2017

Southern Ocean Eddy Heat Flux and Eddy-Mean Flow Interactions in Drake Passage

Annie Foppert
University of Rhode Island, annie_foppert@uri.edu

SOUTHERN OCEAN EDDY HEAT FLUX AND EDDY-MEAN FLOW INTERACTIONS IN DRAKE PASSAGE

BY

ANNIE FOPPERT

A DISSERTATION SUBMITTED IN PARTIAL FULFILLMENT OF THE REQUIREMENTS FOR THE DEGREE OF

DOCTOR OF PHILOSOPHY

IN

OCEANOGRAPHY

UNIVERSITY OF RHODE ISLAND

2017

DOCTOR OF PHILOSOPHY DISSERTATION

OF

ANNIE FOPPERT

APPROVED:

Dissertation Committee:

Major Professor Kathleen A. Donohue

D. Randolph Watts

Jason M. Dahl

Nasser H. Zawia

DEAN OF THE GRADUATE SCHOOL

UNIVERSITY OF RHODE ISLAND

2017

ABSTRACT

The Antarctic Circumpolar Current (ACC) is a complex current system composed of multiple jets that is both unique to the world's oceans and relatively under observed compared with other current systems. Observations taken by current- and pressure-recording inverted echo sounders (CPIES) over four years, from November 2007 to November 2011, quantify the mean structure of one of the main jets of the ACC - the Polar Front - in a composite-mean sense. While the array of CPIES deployed in Drake Passage included a 3 x 7 local dynamics array, analysis of the Polar Front makes use of the line of CPIES that spanned the width of Drake Passage (C-Line). The Polar Front tends to prefer one of two locations, separated along the C-Line by 1° of latitude, with the core of the jet centered on corresponding geopotential height contours (with a 17 cm difference between the northern and southern jets). Potential vorticity fields suggest that the Polar Front is susceptible to baroclinic instability, regardless of whether it is found upstream (farther south along the C-Line) or downstream (farther north along the C-Line) of the Shackleton Fracture Zone (SFZ), yet the core of the jet remains a barrier to smaller-scale mixing, as inferred from estimated mixing lengths.

Within the local dynamics array of CPIES, the observed offset between eddy heat flux (EHF) and eddy kinetic energy (EKE) and the alignment of EHF with sea surface height (SSH) standard deviation motivates a proxy for depth-integrated EHF that can be estimated from available satellite SSH data. An eddy-resolving numerical model develops the statistics of a logarithmic fit between SSH standard deviation and cross-frontal EHF that is applied to the ACC in a circumglobal sense. We find 1.06 PW enters the ACC from the north and 0.02 PW exits towards Antarctica. The magnitude of the estimated EHF, along with contemporaneous estimates of the mean heat flux, suggests that the air-sea heat flux south of the PF

is an overestimate. Long-term trends in EHF are calculated from January 1992 to December 2014 and reveal varying trends at the eight ACC EHF hot spots, with only three having statistically significant temporal trends of strengthening cross-frontal EHF.

The dynamics of an oceanic storm track are investigated using CPIES observations in the local dynamics array to better understand the processes responsible for the spatial offset between EHF and EKE. Wave activity flux ($\boldsymbol{W}$), calculated from the total geostrophic stream-function, is used to diagnose eddy-mean flow interactions in the eddy-rich region immediately downstream of the SFZ. In the full four-year mean and in a composite of eddy events, elevated values of eddy potential energy (EPE) are aligned with the vertical component of $\boldsymbol{W}$. This is indicative of a conversion of mean available potential energy to EPE through EHF associated with baroclinic instability. Emanating from this region, horizontal $\boldsymbol{W}$ vectors point towards the adjacent region of elevated EKE. A case study of an eddy event, lasting from 15 to 23 July 2010, is presented and highlights the capability of $\boldsymbol{W}$ to illustrate the evolution of the storm track in a snap-shot sense. The alignment of elevated values of EKE with the convergence of the horizontal $\boldsymbol{W}$ vectors indicates the importance of barotropic processes in transporting EKE away from the ACC's interaction with the SFZ.

ACKNOWLEDGMENTS

I want to, first of all, thank the GSO community for providing an wonderful work environment. In particular, I'd like to thank all the friendly faces in the PO department. I will sincerely miss drinking coffee and eating bagels and donuts with you all every Friday. I also want to acknowledge NSF, because without their financial support this work would not have happened.

A million thanks to Brandon, whose patience knows no bounds.

To my Jamestown family who provided me with good food and a good laugh when I needed it most. And to the rest of my family and friends, it's been a long road, and I couldn't have done it without all your support.

To Patrick, who didn't mind when I lost my mind and who never underestimated the healing power of adorable dogs. Your kindness keeps me going and I thank you for it.

To Karen, thank you for the immeasurable amount of guidance you provided to me. I don't know where I'd be without your help.

To Jaime, thank you for making my last semester here as a TA so much fun and so worth it. Thank you for your genuine interest in my work. And to Jason and Stephen, thank you for being on my committee.

To Randy, thank you for always double-checking my units, for believing in my work, and for getting me back out of the tennis court.

And finally, to Kathy, I have been blessed to work for you. As a scientist and as a person, you inspire me. Thank you for everything, but especially thank you for trusting me with Nykki when you are away.

DEDICATION

For the giants upon whose shoulders I stand,

and for those who wish to stand upon mine.

PREFACE

This dissertation is a combination of three individual manuscripts in different stages of publication in scientific journals. The first chapter was published in the Journal of Geophyiscal Research: Oceans in 2016; the second is in revision as of June 2017 at the same journal; and the third is in preparation. The dissertation is presented in manuscript format.

TABLE OF CONTENTS

Page

LIST OF FIGURES

LIST OF TABLES

Table **Page**

MANUSCRIPT 1

The Polar Front in Drake Passage: A composite-mean stream-coordinate view

by

Annie Foppert[1], Kathleen A. Donohue[1], and D. Randolph Watts[1]

[1] *Graduate School of Oceanography, University of Rhode Island, Narragansett, RI*

Published in Journal of Geophysical Research: Oceans 2016

1.1 Abstract

The Polar Front (PF) in Drake Passage is studied using 4 years of data collected by a line of current and pressure recording inverted echo sounders complemented with satellite altimetry. Two preferred locations of the PF are found. A northern and southern PF are separated geographically by a seafloor ridge - the Shackleton Fracture Zone - and hydrographically by 17 cm of geopotential height. Expressed in stream coordinates, vertical structures of buoyancy were determined with a gravest empirical mode analysis. Baroclinic velocity referenced to zero at 3500 dbar, width, and full transport (about 70 Sv) of the jets are statistically indistinguishable; the two jets alternately carry the full transport rather than coexisting. The influence of local bathymetry and deep cyclogenesis manifests as differences in deep reference velocity structures. Downstream reference velocities of the PF-N and PF-S reach maximum speeds of 0.09 and 0.06 m s^{-1}, respectively. Buoyancy fields are indicative of upwelling and poleward residual circulation at the PF. Based on potential vorticity fields and mixing length estimates, the northern and southern PF both act as a barrier to cross-frontal exchange.

1.2 Introduction

The Antarctic Circumpolar Current (ACC) is a unique feature of the world's oceans, unrestricted by continental boundaries in the latitude band of Drake Passage. To first order, the ACC is a wind-driven, generally eastward flowing current, strongly steered by large bathymetric features found throughout the Southern Ocean. In terms of global circulation and climate, the ACC's secondary circulation plays a key role. Vertical and meridional flow along isoneutral (constant buoyancy) surfaces in the ACC forms the southern limb of the global meridional overturning circulation. The buoyancy structure of the ACC, therefore, plays a crucial role in global circulation and stratification.

Global schematics and idealized theories often represent the ACC as one swift current, yet it has a complex structure with multiple fronts/jets. As these jets navigate the bathymetry of the Southern Ocean, each follows its own preferred path(s) over steep ridges, around shallow plateaus, or through narrow gaps, as a few examples. Enhanced eddy kinetic energy and increased particle crossings are noted in the lee of abrupt bathymetry and are thought to be indicative of enhanced cross-frontal eddy fluxes (*Thompson and Sallée*, 2012).

The number of ACC fronts varies with space and time. Historical hydrography pointed to 3 fronts in Drake Passage: Subantarctic Front (SAF), Polar Front (PF), and Southern ACC Front (SACCF) (*Baker et al.*, 1977). Around the Southern Ocean, the hydrographic markers used to tag these fronts are commonly associated with a strong current, leading to the "classic" circumpolar view of the ACC (*Orsi et al.*, 1995). Given the nearly equivalent-barotropic and surface-intensified nature of the ACC's mean velocity, SSH contours well represent flow streamlines and satellite altimetry is a particularly useful tool to track fronts. Recently, *Sokolov and Rintoul* (2009a) showed in a circumpolar analysis that multiple distinct SSH

contours are often associated with the "classic" fronts. For example, they find the PF aligns, circumpolarly, with 3 SSH values, and that about 20 cm of height separates the northernmost and southernmost fronts.

Satellite altimetry and numerical models reveal a highly complex frontal structure, especially in snapshots. That is, a particular frontal contour (of SSH, for example) does not maintain a consistently strong gradient along its circumpolar path. Moreover, these frontal contours converge together in some locations and separate in other locations or at other times. *Thompson and Sallée* (2012) used a numerical model to simulate a reorganization of fronts in the lee of simple representations of a ridge. Recently, *Thompson and Naveira-Garabato* (2014) find along-stream alterations in potential vorticity structure, especially deeper than 2000 m, at select standing meanders associated with large bathymetric features around the Southern Ocean. Frontal interactions are especially enhanced in Drake Passage, where the ACC is constricted vertically by a complex submarine ridge system and horizontally by continental boundaries.

Our focus is on the PF in Drake Passage, particularly as it navigates the Shackleton Fracture Zone (SFZ). The SFZ is the main ridge spanning the entire passage, rising to depths as shallow as 2000 m in the region near the PF (Figure 1.1). Within Drake Passage, the SAF is generally banked up against the northern slope, the PF is more centrally located, and the SACCF is found within 200 km of the southern boundary (*Lenn et al.*, 2008). *Firing et al.* (2011), using repeat ADCP measurements, cite average surface velocities of 0.3 m s^{-1} in the region of the PF, and extrapolate to the bottom with an exponential velocity fit to estimate a full-depth PF transport of 63 Sv.

It is crucial to know the mean velocity and potential vorticity structure of the jet for an interpretation in the framework of linear instability theory. Studying

departures from the basic state requires a priori knowledge of the basic state. Many studies average geographically (e.g., *Firing et al.* (2011)), so the strength of a meandering jet appears weakened. Transformation of data into a stream-coordinate system centered on the front is ideal for investigating the jet's dynamics and stability properties. Within a mixing-length framework, *Naveira-Garabato et al.* (2011) show the PF is a barrier to mixing at all but one of the repeat WOCE transects in the Southern Ocean. Their study included transects SR1 and SR1b that are located just upstream and downstream of our study area (Figure 1.1).

We combine 4 years of moored current and pressure-recording inverted echo sounder (CPIES) data collected during the cDrake project with satellite altimetry to study the cross-frontal structure of the PF (Section 2). A stream coordinate system is developed and we find the jet takes two preferred locations about the SFZ (Section 3). The velocity and vorticity fields of the northern and southern PF are presented in Section 4. Section 5 discusses our choice of PF definition, and puts this work in the context of transport, mixing, and residual circulation; we conclude in Section 6.

1.3 Data

1.3.1 cDrake CPIES

The cDrake project includes a line of 20 (combined within an array of 45) CPIES that spanned Drake Passage from November 2007 to November 2011 (www.cdrake.org). We refer to the line of CPIES as the C-Line. Each CPIES measures seafloor to surface round-trip acoustic travel time (τ) every 10 minutes along with bottom pressure and temperature twice an hour. Each is equipped with a current meter to measure horizontal velocities outside the bottom boundary layer (50 m above the seafloor) every hour. These bottom velocities (u_b, v_b) are used to reference the baroclinic velocity shear. All time series are 3-day low-passed

through a 4th-order Butterworth filter and subsequently resampled twice a day. For more details on data processing see the cDrake CPIES data report (*Tracey et al.*, 2013).

The travel-time records have been processed further such that their variability reflects fluctuations in the baroclinic structure. That is, the time series are adjusted for changes in path length, inverted barometer effect by atmospheric pressure, changes in gravity due to latitude, and a seasonal cycle (following *Baker-Yeboah et al.* (2009) and *Donohue et al.* (2010)). The measurements are mapped - optimally interpolated to 10-km horizontal spacing - within the entire array of CPIES.

We chose to convert acoustic travel time to surface geopotential anomaly referenced to 3500 dbar, Φ_{0-3500} (subscript neglected hereafter). A gravest empirical mode (GEM) technique relates travel-time values measured by the CPIES to temperature and salinity at chosen depth levels using historical hydrographic casts in the region (*Meinen and Watts*, 2000). The data are then interpolated to a 10-dbar vertical grid to give $T(\tau, p)$ and $S(\tau, p)$. These T-GEM and S-GEM fields are vertically filtered along the pressure coordinate with a smoothing length ranging from the equivalent of 35 dbar in the thermocline to 500 dbar at depth. The intention is to preserve the thermocline structure while smoothing over noise at depth (due to sparsity of deep-reaching profiles). Φ at the surface can be calculated from T and S, effectively creating 2-dimensional GEM fields of $T(\Phi, p)$ and $S(\Phi, p)$.

When analyzing a jet's structure, a buoyancy GEM (b-GEM) is a natural next step from the T- and S-GEM. First, T and S are used to calculate neutral density, γ^n, following *Jackett and McDougall* (1997). Then, buoyancy is $b = \frac{g}{\rho_0}(\gamma^n - \gamma_0)$, where $g = 9.8$ m s^{-2} is local gravitational acceleration, $\rho_0 = 1035$ kg m^{-3} is a standard ocean density, and $\gamma_0 = 28.5$ kg m^{-3} is a deep neutral density. Finally,

the b-GEM is vertically smoothed consistently with the T- and S-GEMs. The scatter in the b-GEM, the standard deviation of buoyancy calculated from the CTD casts about the GEM value, is on the order of 2 - 6×10^{-4} m s^{-2}. Below 100 dbar, the spline fits of the b-GEM explain 95% or more of the variance in the CTD casts (not shown).

1.3.2 Altimetry

Our analysis uses satellite altimetry, which provides a 2-dimensional view of the sea surface. Addition of a weekly-mean sea level anomaly product to mean dynamic topography creates maps of SSH. Sea level anomaly is provided by AVISO with support from CNES (Archiving, Validation and Interpretation of Satellite Oceanographic data; Centre National d'Etudes Spatiales; 1/4° resolution) and is combined with the mean dynamic topography product of CNES-CLS09 (CNES-Collecte Localisation Satellites 2009; 1/3° resolution). The resulting SSH maps have 1/3° horizontal resolution.

The SSH maps expand our perspective of the region and provide a first approximation for location of the PF. The angle from perpendicular, θ, at which the ACC crossed the C-Line is crucial for projection into our stream-coordinate system (Figure 1.2). It is the angle clockwise-positive from the C-Line to the cross-frontal axis, $Y_{PF} = \tan^{-1}(\eta_x/\eta_y)$, where η is the weekly SSH data and the $[x, y]$ subscripts are standard horizontal derivatives. Finally, θ is interpolated to the twice-daily resolution of the CPIES data.

1.4 Stream-coordinate system

Stream coordinates are especially useful for investigating features that shift laterally in time - in this case the meandering PF. A simple geographic average will smear the properties of a meandering front, widening its structure. With a

line of measurements, the jet will appear weakened if it does not cross the line directly perpendicularly, as the cross-frontal gradient will be artificially reduced. These issues are avoided by converting the data into stream coordinates that move and rotate with, in this case, the PF. A schematic of our stream-coordinate system is shown in Figure 1.2.

We use the SSH data to find its maximum 2-D gradient magnitude, $|\nabla SSH|$, over the 4 years of cDrake, along the C-Line, away from the northern and southern boundaries. The highest mean geostrophic velocity, maximum $|\nabla SSH|$, is associated with the -46.6 cm SSH contour, shown by the thick grey line in Figure 1.1. On average, it occurs at 58.25°S. Tracking the path of this contour, we only consider times when the altimeter shows it to be quasi-perpendicular to the C-line, i.e. $|\theta| < 20°$, for at least 2 consecutive weeks. This angle threshold ensures the along-line gradient of a measured value requires only minimal correction, because it is at least 94% of the actual 2-D gradient magnitude. Additionally, it can be noted that the choice to demand the PF to be slowly varying does not significantly impact the distribution of maximum $\nabla\Phi$. Figure 1.3, top left panel, shows the latitudinal distribution of the maximum $\nabla\Phi$ for all quasi-perpendicular times in white and the subset of times that are also slowly-varying in red and blue, for comparison.

We use the CPIES twice-daily travel-time records (converted to geopotential anomaly, Φ) to refine the location of the PF's core by finding the maximum $\nabla\Phi$ within the $\pm 1/2°$ interval of latitude around the -46.6 cm SSH contour. Figure 1.3 shows a bimodal distribution of maximum $\nabla\Phi$ in latitude (and in Φ, compared in Section 5.1). The strongest gradient is preferentially located either north or south of 58.5 - 58.6°S, with a clear minimum atop the SFZ. Only 48 of the 1853 quasi-perpendicular half-days fall in the 58.5 - 58.6°S latitude range (Figure 1.3,

top left panel). We see this as an opportunity to study the structure of the PF and investigate the influence of local bathymetry. We, therefore, choose to examine two composite-mean jets: a northern and a southern PF, flowing upstream and downstream of the SFZ, respectively.

Figure 1.2 shows our stream-coordinate system with the angle, θ, from altimetry and location of the maximum $\nabla\Phi$ from CPIES as the PF core. Geopotential anomaly values at the core, Φ_{PF}, are allowed to change in time, always associated with the strongest along-line gradient. Earlier, we experimented with defining the core location by two fixed values of Φ, one for the PF-N and one for the PF-S, and found the structure of the jet doesn't significantly change in terms of width and strength, but its velocity peak was offset laterally by up to 20 km from the chosen Φ (not shown).

We exclude instances with rings and/or S-shapes (i.e. when Φ_{PF} appears along the C-Line more than once) and when the altimeter shows the local angle at the core of the PF is oblique (i.e. $|\theta| > 20°$). As a result, 1100 half-days of mapped fields are used for subsequent analyses, with a nearly 60-40 split between times considered PF-N and PF-S. Grey bars in the top right panel of Figure 1.3 show the $\nabla\Phi$ distribution of the half-days that contribute to the final composite means.

1.5 Polar Front structure

1.5.1 Geopotential anomaly and buoyancy

On average, the core of the northern PF is $\Phi_N = 17.5 \pm 0.4$ m^{2}s^{-2}, while that of the southern PF is $\Phi_S = 15.9 \pm 0.2$ m^{2}s^{-2}. The difference between these two cores is significant and equivalent to 17 cm of geopotential height. The cited errors represent standard errors of the mean. Degrees of freedom for the PF-N and PF-S are 23 and 17, respectively, based on the 15-day integral time scale of

the travel-time records (*Bendat and Piersol*, 2000). In a time-mean sense, the core of PF-N crosses the line at 58°S, but it shifts as far north as 56.8°S (Figure 1.3, left column). The core of PF-S, on average, crosses at 59°S, and only shifts as far south as 59.3°S. Following the PF as defined above, we project the mapped Φ data onto the frontal axis such that $Y_{PF} = Y_C = 0$ km at the PF's core and $Y_{PF} = Y_C \cdot cos\theta$ (Figure 1.2). We then convert from $\Phi(Y_{PF}, t)$ to $b(Y_{PF}, p, t)$ with the GEM technique described in Section 2.1.

Figure 1.4 shows the resulting average buoyancy fields of the PF-N and PF-S. Isoneutral surfaces (surfaces of equal buoyancy) of the PF shoal towards the pole, i.e. with decreasing Y_{PF}. The northern PF is warmer and more buoyant, with mean core temperatures about 0.3°C higher and isopycnals shifted about 200 dbar deeper, than its southern counterpart. The stratification, $N^2 = b_z$, of the front is strongest on the poleward side ($Y_{PF} < 0$) around 80 dbar, in the tongue of winter water coming up from the south.

1.5.2 Baroclinic velocity

Cross-stream buoyancy gradient is related to the vertical shear of along-stream baroclinic velocity, as expressed by the thermal wind relationship:

$$\frac{\partial U_{bcb}}{\partial z} = -\frac{1}{f}\frac{\partial b}{\partial Y}. \tag{1.1}$$

$U_{bcb} = U_{bcb}(Y, p, t)$ is downstream baroclinic velocity referenced to zero at 3500 dbar and $Y = Y_{PF}$ is the cross-stream direction with positive northward (subscript dropped hereafter).

The PF-N and PF-S are surface-intensified baroclinic jets. At their cores, the surface down-stream baroclinic speed, referenced to 3500 dbar, reaches 0.59 m s^{-1} (with standard errors of $\pm$0.05 m s^{-1} and $\pm$0.04 m s^{-1} for the PF-N and PF-S, respectively). The shear is strong - weakening the jets to half their surface value

by 1000 dbar and halving again by 2000 dbar (to $\bar{U}_{bcb} = 0.15$ m s^{-1}). Deeper than 1000 dbar, at the core of the jets, the shape of the baroclinic shear can be represented by the exponential function $A[exp(-(p-D)/D)-1]$ where $D = 3500$ dbar is the bottom pressure and $A = 0.26$ m s^{-1} is a best-fit constant coefficient.

The width of the jet is defined as the distance between surface baroclinic speed's first minimum or zero-crossing on either side of the core. Both extend 90 km north of the core (to $Y = 90$ km) where there is a zero-crossing for PF-N and local minimum for PF-S (Figure 1.5). On the poleward side, the PF-N has a local minimum at Y = -70 km and the PF-S has a zero-crossing at Y = -80 km. Hence, we choose to define the southern extent of the PF as the average of these two distances, $Y = -75$ km. So, the width of the PF is 165 km, independent of latitude. This leads to a baroclinic transport relative to 3500 dbar of 49 Sv for both jets; more details on transport are found in Section 4.4.

1.5.3 Reference velocity

Neglecting any shear below 3500 dbar, we take the measured bottom velocity at each CPIES site to be the velocity at 3500 dbar, except at C10 where the nominal bottom pressure is 2540 dbar. At this shallow site, we adjust the measured velocity down to 3500 dbar using the mean shear profile at C10's distance from the PF's core, such that the reference velocity at C10 is the offset between the measured velocity and the baroclinic velocity at 2540 dbar. That is, $(u_b, v_b)_{3500} = (u_b, v_b)_{measured} - \bar{U}_{bcb}(Y_{C10}, 2540)$, where the overbar denotes a composite-mean value.

All reference velocities are converted into our stream-coordinate system with the standard vector rotation:

$$U_{ref} = u_b cos(\alpha) - v_b sin(\alpha), \tag{1.2}$$

$$V_{ref} = u_b sin(\alpha) + v_b cos(\alpha). \tag{1.3}$$

Here, (u_b, v_b) are the measured eastward and northward reference velocities, and α is the angle clockwise-positive from north to Y_{PF} (Figure 1.2). Reference velocity measurements are then organized by distance from the jet's core and averaged in 20-km bins (Figure 1.6). The spacing of CPIES is such that a measurement does not fall in each bin every half-day and there are fewer data in each 20-km bin than in the mapped fields (Figure 1.6, bottom right). Mean reference velocities $(\bar{U}_{ref}, \bar{V}_{ref})$ are smoothed horizontally using a 4th-order Butterworth filter with 100-km cut-off distance and interpolated to the 10-km grid of Y_{PF}.

The PF-N and PF-S have downstream components of reference velocity that are at least a factor of 6 and 10 weaker, respectively, than their surface $\bar{U}_{bcb}$ speeds (Figure 1.5, top panel). The strongest downstream velocity of the northern PF is found 20 km north of its core, where $\bar{U}_{ref} = 0.09$ m s^{-1}. The sign of $\bar{U}_{ref}$ changes, i.e. flow is upstream, at $Y = 80$ km and farther north from the PF-N's core. $\bar{U}_{ref}$ of the southern PF is downstream everywhere and reaches a maximum (of 0.06 m s^{-1}) 80 km north of its core (Figure 1.5). Standard errors of the mean for the PF-N are 0.009-0.015 m s^{-1}, with smaller values south of its core. For the PF-S, errors are comparable to those of the PF-N on the northern flank of the jet (about 0.012 m s^{-1}), but increase by a factor of 2 near its core before decreasing poleward. Degrees of freedom are not constant across the fronts, ranging from 12 to 64, with the PF-N consistently having more than the PF-S.

$\bar{V}_{ref}$ is the cross-stream component of the reference velocity field. The baroclinic portion is defined to be aligned with the flow of the PF, making $V_{bcb} = 0$ m s^{-1}. For both the northern and southern expressions of the PF, $\bar{V}_{ref}$ is negative everywhere (Figure 1.6). This represents an advection of warm water poleward across the core of both jets. The maximum cross-stream speed is

0.08 m s^{-1}, found north of the jet's core (at $Y = 50$ km for the PF-N and on the very northern edge of the PF-S). Speeds decrease poleward across the core of the PF, by about a factor of 2 for the PF-N and to values not significantly different from zero for the PF-S.

1.5.4 Transport

The PF's total transport is the addition of the baroclinic transport and the reference transport. The baroclinic transport, T_{bcb}, of the PF-N is 49.2 ± 4.8 Sv and that of the PF-S is 49.1 ± 3.8 Sv. This was calculated using the mean potential energy anomaly (PEA) relative to 3500 dbar, i.e. Fofonoff Potential denoted by χ, along the frontal axis (*Fofonoff*, 1962). Fofonoff Potential is equivalent to a baroclinic mass transport function. This is appropriate because the composite-means are defined to be on either side of the SFZ, such that neither jet is interrupted at depth by topography. The volume transport and its standard error are given by

$$T_{bcb} = -\frac{1}{\rho_0 f}[\chi_{(90)} - \chi_{(-75)}], \tag{1.4}$$

$$SE_{bcb} = -\frac{1}{\rho_0 f}\sqrt{SE^2_{\chi_{(90)}} + SE^2_{\chi_{(-75)}}}. \tag{1.5}$$

Again, f is the local Coriolis parameter and $\rho_o = 1035$ kg m^{-3} is a standard ocean density. The subscripts of χ represent location along the frontal axis, such that $\chi_{90} = \chi(Y = 90 \text{ km})$. For a more complete description of calculating baroclinic transport from PEA, we refer the reader to Section 2 in *Rodrigues et al.* (2010).

The reference transport, T_{ref}, is calculated as the sum of transport in each 20-km bin within the width of the PF. For the PF-N, $T_{ref} = 19.2 \pm 2.7$ Sv; for the PF-S, $T_{ref} = 20.3 \pm 4.2$ Sv. This accounts for 28% (29 %) of the total transport of the northern (southern) PF. The error of the reference transport is calculated as the root of the sum of the squared standard error of transport in each bin within

the width of the PF. For simplicity, we estimate the PF's extent to be from Y = -80 to 80 km in reference transport and error calculations.

The total (along-stream) transport of the PF-N is 68.4 ± 5.5 Sv and that of the PF-S is 69.4 ± 5.7 Sv. These values do not differ statistically. The total error is made up of error due to the baroclinic field, error due to the reference field, and error due to the choice of the jet's width. Errors from the baroclinic and reference fields are explained and cited above. For the baroclinic field, the error due to 5 km of uncertainty in defining the width of the jet (Section 4.2) is less than 1 Sv. The error due to width of the reference field is negligible.

1.5.5 Relative vorticity

The baroclinic relative vorticity, ζ_{bcb}, is shown as a fraction of f in Figure 1.5. It should be noted now that curvature in our analysis is negligible with averages on the order of 10^{-6} and 10^{-7} m^{-1} for the PF-N and PF-S ($\kappa = [(\eta_x^2\eta_{yy} + \eta_y^2\eta_{xx} - \eta_x\eta_y(\eta_{xy} + \eta_{yx}))/(\eta_x^2 + \eta_y^2)^{3/2}]$, where η is SSH and $[x, y]$ subscripts represent horizontal derivatives, as before). Their respective standard deviations are an order of magnitude larger. The average curvature vorticity, κU_{bcb}, of the PF-N and PF-S is 1% and 0.2% of f (and standard deviation is 5% and 2% of f, respectively). Therefore, baroclinic relative vorticity is well approximated by the cross-stream velocity shear, $\zeta_{bcb} = -dU_{bcb}/dY$.

Figure 1.5 shows that average relative vorticity, $|\bar{\zeta}_{bcb}|$, is stronger on the southern flank of each PF, reaching nearly 10% of f. This is consistent with a decrease in Rossby radius as (full-depth) stratification decreases poleward in the Southern Ocean. On the northern flank of the jet, $|\bar{\zeta}_{bcb}|$ of the northern PF reaches 7% of f, whereas that of the southern PF reaches 6% of f. This justifies our assumption of a low Rossby number to examine velocities and dynamics in a quasi-geostrophic framework.

The mean reference relative vorticity, $\bar{\zeta}_{ref} = -d\bar{U}_{ref}/dY$, is weaker than that of the baroclinic field (Figure 1.5). Specifically, $|\bar{\zeta}_{ref}|$ in the southern PF doesn't exceed 0.5% of f. On the cyclonic side (northern flank) of the PF-N, $|\bar{\zeta}_{ref}|$ gets nearly as large as 2% of f. Note that these values are on the same order as the baroclinic curvature, κU_{bcb}, and small compared to their baroclinic counterparts.

1.5.6 Potential vorticity

Potential vorticity, Q, is calculated directly from velocity and buoyancy fields, expressed as

$$Q = g^{-1}(fb_z - U_Y b_z + U_z b_Y). \tag{1.6}$$

Here, we use the full velocity field, $U = \bar{U}_{bcb} + \bar{U}_{ref}$, the addition of the reference velocity to the mean baroclinic velocity. Potential vorticity is smoothed horizontally with a cut-off distance of 100 km, consistent with reference velocity calculations.

The terms on the right-hand-side of equation 1.6, from left to right, represent thickness-, relative-, and twisting-Q. The bottom panel of Figure 1.7 shows the thickness-Q and relative-Q in the upper 200 dbar, where relative-Q is greatest due to increased horizontal velocity shear and stratification. Relative-Q is an order of magnitude less than thickness-Q, but intensifies the cross-stream ∇Q at the core. The magnitude of relative-Q decreases with depth to 5% of thickness-Q by 700 dbar.

Figure 1.7 shows the total Q of the PF, dominated by thickness-Q. From pycnocline to near bottom, Q changes by two orders of magnitude. Across the core of the jet, in the upper 200 dbar, in both cases, the magnitude of Q changes sharply from larger to smaller values by about a factor of 2 (Figure 1.7, bottom panel). This corresponds to a change from thinner to thicker layers of buoyancy southward across the jet's core, as seen in Figure 1.4. The strong cross-stream ∇Q

acts as a barrier to mixing across the PF.

At the core of the PF-N and PF-S, the cross-stream ∇Q changes sign horizontally with distance and vertically with pressure. Recall that these are necessary, but not sufficient, conditions for barotropic and baroclinic instability, respectively. The horizontal change in sign is noticeable in the upper 200 dbar (Figure 1.7, bottom panel). The vertical change in sign occurs between 400 and 600 dbar, below the pycnocline and deeper than the subsurface temperature inversion (not shown).

Figure 1.8 presents Q in buoyancy space. Again, there is a strong gradient at the core of the jet. In fact, ∇Q here is sharper than that found in pressure space, particularly towards the surface. For example, on the $b = 10 \times 10^{-3}$ m s^{-2} isoneutral, Q changes by a factor of 3 for the PF-N and a factor of 4.5 for the PF-S, compared to the factor of 2 in the upper 200 dbar. A reversal in sign of ∇Q occurs only in the deep buoyancy layers of the PF (Figure 1.9). That is, within buoyancy layers, the reversal in sign of ∇Q occurs only in the bottommost layer where that deep sloped layer encounters a less sloped seafloor.

1.6 Discussion

1.6.1 Comments on PF definition

We find, for times when the PF crosses the C-Line nearly perpendicularly, a northern and southern PF; it is rarely found directly over the SFZ (Figure 1.3). Interestingly, the baroclinic velocity structure and transport of the PF-N and PF-S are statistically indistinguishable, yet the fronts are separated geographically by the SFZ and hydrographically by 17 cm of geopotential height. The PF-N centers on a Φ associated with a warmer and more buoyant profile than the PF-S. In the classic view of the ACC, the PF is found at the northern extent of the 2°C isotherm along the temperature minimum at depths deeper than 200 m (*Orsi et al.*, 1995). In our T-GEM, the Φ associated with this circumpolar definition coincides with

Φ_N.

We look for the PF by searching for the maximum $\nabla\Phi$ at any time, while *Thompson and Sallée* (2012) used probability density functions (PDFs) to find fronts. Those authors take advantage of the low probability of finding a frontal contour where the horizontal gradients are large, and therefore fronts appear as local minima in PDFs. The areas of relative quiescence between the ACC's fronts makes this method so effective, as these inter-frontal zones manifest as local maxima in PDFs. In a histogram of Φ data along the C-Line, we find a broad minimum about the value of the southern PF, $\Phi_S = 15.9$ m^2 s^{-2}, spanning Φ values from $15 - 17$ m^2 s^{-2} (not shown).

Note that this does not mean the northern PF doesn't exist (nor that it is an artifact of our method), but rather implies that the PF-N is not bracketed by two zones of relative quiescence, as the southern PF often is. The enhanced SSH variance (Figure 1.1, right panel) in the region north of the PF, south of the SAF, could mask the manifestation of Φ_N as a local minimum. If a jet is embedded within a region of high variability, the PDF method has trouble identifying it from the background variability. In fact, *Chapman* (2014) shows that the PDF method breaks down in regions of low "signal-to-noise" ratio (e.g. mean ∇SSH relative to SSH variance). Since the PF-N is located in a more energetic and variable place than the PF-S (Figure 1.1), the maximum $\nabla\Phi$ is a more appropriate search criterion than the minimum probability of Φ.

Motivation to study physical differences of the jet on either side of steep bathymetry and the clear minimum in latitudinal distribution at the SFZ (Figure 1.3) led to composite-mean jets based on latitude. The bottom row of Figure 1.3 shows another approach of partitioning by Φ: the occurrences of maximum $\nabla\Phi$ favor Φ values either higher or lower than 17.25 m^2 s^{-2}, with a distinct mini-

mum there. We very well could have chosen to create composite means of the PF based on Φ value: a warmer and a colder PF. Figure 1.3 shows that neither split is perfect, yet we recognize that at some point a choice needs to be made and the desire to investigate bathymetric influence on the PF urged a latitudinal division.

There has been quite a bit of discussion in recent literature about the number of fronts in the ACC (e.g. *Sokolov and Rintoul*, 2007, 2009a,b). Though it is not our intention to address this question directly, we can offer a few remarks. The horizontal and vertical constriction of Drake Passage make it an unique sector of the Southern Ocean, and analyses done outside this region may not be applicable within it. *Sokolov and Rintoul* (2009b) tag the PF globally with three frontal contours, and the difference between the northernmost and southernmost is either 18 or 25 cm of SSH, depending on reference level (their Table 1). In this sense, our result of a 17-cm difference between the PF-N and PF-S aligns quite well with their circumpolar height range for the PF. However, we do not find a preferred Φ for a central PF in Drake Passage, as the local minimum at 19 m^2 s^{-2} is not as pronounced as that at 17.25 m^2 s^{-2} or 58.5°S (Figure 1.3).

The width of the PF (165 km) is comparable to other studies of baroclinic jets in stream coordinates. *Meinen et al.* (2003) use data from south of New Zealand to study the SAF, and estimate its width as 220 km. *Sokolov and Rintoul* (2007) estimate the width of the PF from satellite data as 40 - 90 km (converted here from degrees latitude, their Figure 3), less than the width we find by a factor of 2 - 4. Perhaps the definition of jet width plays a subtle role in determining the number of fronts needed to accurately characterize the ∇SSH field of the ACC. Additionally, confluence in Drake Passage may force the branches of the PF to merge into fewer, and perhaps broader, jets than other locations around the Southern Ocean.

1.6.2 Inferences from transport

The mean baroclinic transport of the PF-N and PF-S (49 Sv) constitutes a significant fraction of the total baroclinic transport of the ACC. *Chidichimo et al.* (2014) find the SAF and PF together carry an average baroclinic transport referenced to the bottom of 105 Sv through Drake Passage. Therefore, if these two versions of the PF flowed simultaneously, the SAF would be left carrying a mere 7 Sv of baroclinic transport. So, we deduce that the PF transport alternates between the PF-N and PF-S in Drake Passage.

Figure 1.10 shows the 4-year mean Fofonoff Potential (PEA) along the C-Line, equivalent to a baroclinic mass transport function. In the entire region encompassing the PF (from about 60°S to 57.5°S) the PEA changes by about 65×10^5 J m^{-2}. Note that the angle at which the jet crosses the line is irrelevant to PEA, so converting to stream coordinates is not necessary. Also note that since PEA is equivalent to baroclinic mass transport, it is directly convertible to volume transport (Sv, see Section 4.4).

Subsets of times included in our composite averages are shown in Figure 1.10. Each example shows that the change in PEA made by either the PF-N or PF-S individually accounts for most, if not all, of the change in PEA spanning the PF region. That is, either the northern or southern jet carries the region's baroclinic transport rather than sharing it. This is further evidence that the PF-N and PF-S do not coexist in Drake Passage. Moreover, cumulative transport along repeat transect SR1b also shows the PF has a bimodal distribution in latitude (*Meredith et al.*, 2011). Their Figure 10 shows that of the 15 hydrography cruises along the transect, 5 were classified as 'southern' years, 9 as 'northern' years, and only 1 as an 'intermediate' year.

Clearly, a transition between these two states occurs, where water transfers

from one core Φ_{PF} to the other. The PF-N and PF-S, in this case, would act as end members in a larger PF system. The transition between these two core states of the PF is a topic of interest, and one where a process model may prove particularly useful.

1.6.3 Inferences from deep circulation

While the baroclinic structure (width and velocity) and along-stream transport of the PF-N and PF-S are identical, the reference fields are not. The PF-N has some upstream flow on its very northern flank ($\bar{U}_{ref} < 0$ m s^{-1}; Figure 1.6, top left). Recall that the PF-N is in a region of high eddy activity as seen by increased SSH variance, especially compared to the PF-S (Figure 1.1, right panel). This upstream flow is likely evidence of interaction with the deep eddy field just downstream of the SFZ (*Chereskin et al.*, 2009).

To remove the deep geographic mean circulation from the reference fields, we subtract CPIES site-mean bottom velocities prior to rotating and averaging. This residual (anomaly) is arguably the signature of the meandering PF. Figure 1.6 (top right panel) shows the reference velocity anomaly, $\vec{U}'_{ref}$, for the PF-N is a cyclone. The result for the PF-S is not statistically different from zero across the front (not shown), probably undetectable because of the wider spacing of the southern CPIES.

For the northern PF, the anomaly of the cross-stream component is slightly poleward, but the along-stream component has a distinct change in sign at the core of the jet (Figure 1.6, top right). Upstream and downstream speeds of U'_{ref} are comparable at about 0.04 - 0.05 m s^{-1}. The magnitude of relative vorticity anomaly, $|\zeta'_{ref}|$, is highest at the core of the PF-N and reaches nearly 1.5% of f, small compared to surface values of $|\zeta_{bcb}|$. This cyclonic circulation can be understood through a simple conservation of (barotropic) potential vorticity argument

($[f+\zeta'_{ref}]/H = \text{constant}$), where ζ'_{ref} acts to balance any changes in either latitude or depth.

Consider the following scenarios. First, the PF-N meanders northward from its upstream longitude while approaching the C-Line transect. The development of negative relative vorticity (a cyclone in the southern hemisphere) balances the decreasing magnitude of f. Second, the PF-N flows down the slope of the SFZ and the magnitude of ζ'_{ref} increases (becomes more cyclonic) to balance the increasing depth. In both scenarios, the dynamics act to increase the cyclonic vorticity, or spin up a deep cyclone at the northern PF.

While the reference velocity of PF-N is strongly influenced by both local bathymetry and deep eddies, the PF-S is in a region of lower eddy activity and weaker cyclogenesis. Figure 1.6 show the reference velocity of PF-S as predominantly downstream with a slight poleward cross-stream component. This velocity structure is consistent with the deep mean circulation in the region. The fact that U'_{ref} of the PF-S is not significantly different from zero is further evidence that regional mean circulation sets its deep flow more so than baroclinic instability (deep eddies).

1.6.4 Implications for residual circulation

The cross-stream component of both PF-N and PF-S is in the poleward direction ($\bar{V}_{ref} < 0$). This is indicative of warm water advection across the jet, associated with upwelling along isopycnals and veering of the PF (*Lindstrom et al.*, 1997; *Holton*, 2004). The buoyancy fields presented in Figure 1.4 also imply upwelling and poleward residual circulation at the PF. That is, the buoyancy layers thin from north to south across the PF (see also Figure 1.9), indicative of a poleward residual transport in those layers (*Karsten and Marshall*, 2002).

We do not see any return of residual circulation here, i.e. we do not see any

buoyancy layers thickening poleward across the PF except in the deepest layer that intersects with the ocean bottom (Figure 1.4). This could be because the downwelling and equatorward flow (a) doesn't occur within Drake Passage, or (b) doesn't occur at the PF (but could at the Southern ACC Front or the SAF, for example), or (c) doesn't occur at these particular times when the PF flows nearly straight through Drake Passage, or (d) occurs in the ageostrophic surface Ekman flow.

1.6.5 Implications for mixing and stability

The strong ∇Q present at the core is indicative of a barrier to isopycnal mixing at the northern and southern PF (Figures 1.7 and 1.8). To further investigate lateral exchange properties, we examine the PF-N and PF-S in the framework of mixing lengths. Figure 1.11 shows the components of the calculation, estimated as $L_{mix} = T_{rms}/|\nabla_b \bar{T}|$, following *Naveira-Garabato et al.* (2011). T_{rms} is the variability of the CTD casts defined as the standard deviation of $(T - \bar{T}_i)$, where T are all CTD casts within $\pm$ 40 km from Y_i and $\bar{T}_i$ is the mean temperature of the PF at $Y = Y_i$. The cross-stream temperature gradient along isoneutral surfaces is $\nabla_b \bar{T}$.

Mixing lengths, L_{mix}, are strongly suppressed at the core of the front in both cases, further indicating the jets are barriers to mixing. Specifically, we find that $L_{mix} < 50$ km at the core of the PF, and slightly more so on the southern flank of the jets (Figure 1.11, bottom row). These results are the same whether temperature or salinity is used to calculate L_{mix}. *Naveira-Garabato et al.* (2011) find the PF to be a barrier to mixing at most repeat hydrography lines around the Southern Ocean, including SR1 and SR1b that bracket our C-Line (black lines in Figure 1.1). We find the PF is a barrier to mixing in Drake Passage as well.

While the PF acts as a barrier to isopycnal mixing, it still satisfies the necessary condition for baroclinic instability. Specifically, when averaged within buoy-

ancy layers, there is a change in sign of cross-frontal ∇Q between the shallow and deep layers (Figure 1.9). It should be noted that the change in sign doesn't occur until the densest layer. Bathymetry, therefore, plays a key role in setting the stability properties of the jet.

Additionally, the sign of ∇Q changes with distance from the core of the jet, satisfying the necessary condition for barotropic instability. This sign reversal occurs in both pressure space in the upper 200 dbar (Figure 1.7, bottom panel) and in the surface layers when Q is averaged in buoyancy layers (Figure 1.9). The change in sign occurs on the southern flank of the PF, poleward of Y = -50 km, and is particularly noticeable at the PF-S. A less-pronounced reversal in sign of ∇Q occurs on the northern flank of the PF-N. The relative-Q, though much smaller in magnitude, is enough to change the sign of ∇Q with distance from the PF's core.

1.7 Conclusions

Along the C-Line in Drake Passage, the PF alternates between 2 distinct cores - separated hydrographically by 17 cm of geopotential height and geographically by the SFZ. While the northern expression of the jet is slightly warmer and more buoyant, the baroclinic velocity structure of the PF-N and PF-S are comparable: maximum $\bar{U}_{bcb}$ near 0.6 m s^{-1}, width of 165 km, and strong vertical shear. Total transports (about 70 Sv) of the northern and southern PF are statistically indistinguishable, with just over 70% carried by their baroclinic fields. Baroclinic relative vorticity is greatest in magnitude along the southern flank of the PF (at Y = -30 km), but $|\bar{\zeta}_{bcb}|$ remains less than 10% of local f across the front.

The potential vorticity fields and mixing length estimates imply both jets act as a barrier to mixing by smaller scale processes, thus tending to preserve the frontal structure. Yet, the Q fields satisfy the necessary conditions for baroclinic and barotropic instability, so meander or mesoscale eddy processes can drive cross-

frontal exchange at the PF-N and PF-S.

Differences between the PF-N and PF-S are found in the structure of the deep reference velocities that are locally influenced. It appears the the PF-N is more affected by deep cyclogenesis, while the PF-S is in a location of less variability so the mean deep circulation sets the shape of the deep flow. In both cases, the cross-stream velocity advects warm water poleward across the core the jet, associated with the upwelling and veering at the PF. Buoyancy fields also imply an upwelling and poleward residual circulation.

Acknowledgements We graciously acknowledge the National Science Foundation for its financial support (ANT-0635437/0636594). The cDrake data are available at the National Centers for Environmental Information, and can be found at http://www.nodc.noaa.gov. Many thanks to Karen Tracey for her time, patience, and insight; to Tom Rossby, Georgi Sutyrin, Mark Wimbush, and Jonas Nycander for thoughtful comments and feedback; and to Andrew Thompson and Kurt Polzin for guidance concerning potential vorticity. We'd also like to thank the reviewers for their consideration.

Bibliography

Baker, D. J., Jr., W. D. Nowlin, Jr., R. D. Pillsbury, and H. L. Bryden (1977), Antartic Circumpolar Current: Space and time fluctuations in the Drake Passage, *Nature*, *268*, 696–699, doi:10.1038/268696a0.

Baker-Yeboah, S., D. R. Watts, and D. A. Byrne (2009), Measurements of sea surface height variability in the eastern South Atlantic from pressure sensor-equipped inverted echo sounders: Baroclinic and barotropic components, *Journal of Atmospheric and Oceanic Technology*, *26*, 2593–2609, doi:http://dx.doi.org/10.1175/2009JTECHO659.1.

Bendat, J. S., and A. G. Piersol (2000), *Ramdom Data: Analysis and Measurement Procedures*, 3 ed., Wiley, New York.

Chapman, C. C. (2014), Southern Ocean jets and how to find them: Improving and comparing common jet detection methods, *Journal of Geophysical Research*, *119*, 4318–4339, doi:10.1002/2014JC009810.

Chereskin, T. K., K. A. Donohue, D. R. Watts, K. L. Tracey, Y. L. Firing, and A. L. Cutting (2009), Strong bottom current and cyclogenesis in Drake Passage, *Geophysical Research Letters*, *36*(23), doi:10.1029/2009GL040940.

Chidichimo, M. P., K. A. Donohue, D. R. Watts, and K. L. Tracey (2014), Baroclinic transport time series of the Antarctic Circumpolar Current measured in Drake Passage, *Journal of Physical Oceanography*, *44*, 1829–1853, doi:10.1175/JPO-D-13-071.1.

Donohue, K. A., D. R. Watts, K. L. Tracey, A. D. Greene, and M. Kennelly (2010), Mapping circulation in the Kuroshio Extension with an array of current and

pressure recording inverted echo sounders, *Journal of Atmospheric and Oceanic Technology*, *27*, 507–527, doi:10.1175/2009JTECHO686.1.

Firing, Y. L., T. K. Chereskin, and M. R. Mazloff (2011), Vertical structure and transport of the Antarctic Circumpolar Current in Drake Passage from direct velocity observations, *Journal of Geophysical Research*, *116*, doi: 10.1029/2011JC006999.

Fofonoff, N. P. (1962), Physical properties of sea water in the sea, volume 1, New York: Wiley-Interscience.

Holton, J. R. (2004), *An Introduction to Dynamic Meteorology*, 4 ed., Academic Press.

Jackett, D. R., and T. J. McDougall (1997), A neutral density variable for the world's oceans, *Journal of Physical Oceanography*, *27*, 237–263, doi:10.1175/1520-0485(1997)0272.0.CO;2.

Karsten, R. H., and J. Marshall (2002), Constructing the residual circulation of the ACC from observations, *Journal of Physical Oceanography*, *32*(12), 3315–3327, doi:10.1175/1520-0485(2002)0322.0.CO;2.

Lenn, Y.-D., T. K. Chereskin, and J. Sprintall (2008), Improving estimates of the Antarctic Circumpolar Current streamlines in Drake Passage, *Journal of Physical Oceanography*, *38*, doi:10.1175/2007JPO3834.1.

Lindstrom, S. S., X. Qian, and D. R. Watts (1997), Vertical motion in the Gulf Stream and its relation to meanders, *Journal of Geophysical Research*, *102*, 8485–8503, doi:10.1029/96JC0349.

Meinen, C. S., and D. R. Watts (2000), Vertical structure and transport on a transect across the North Atlantic Current near 42N: Time series and mean, *Journal of Geophysical Research*, *105*(C9), 21,869–21,891, doi:10.1029/2000JC900097.

Meinen, C. S., D. S. Luther, D. R. Watts, A. D. Chave, and K. L. Tracey (2003), Mean stream coordinates structure of the Subantarctic Front: Temperature, salinity, and absolute velocity, *Journal of Geophysical Research*, *108*(C8), doi: 10.1029/2002JC001545.

Meredith, M. P., P. L. Woodworth, T. K. Chereskin, D. P. Marshall, L. C. Allison, G. R. Bigg, K. A. Donohue, K. J. Heywood, C. W. Hughes, A. HIbbert, A. M. Hogg, H. L. Johnson, L. Jullion, B. A. King, H. Leach, Y.-D. Lenn, M. A. M. Maqueda, D. R. Munday, A. C. Naveira-Garabato, C. Provost, J.-B. Sallée, and J. Sprintall (2011), Sustained monitoring of the Southern Ocean at Drake Passage: Past achievements and future priorities, *Reviews of Geophysics*, *49*(4), doi:10.1029/2010RG000348.

Naveira-Garabato, A. C., R. Ferrari, and K. L. Polzin (2011), Eddy stirring in the Southern Ocean, *Journal of Geophysical Research*, *116*, doi:10.1029/2010JC006818.

Orsi, A. H., T. W. III, and W. D. N. Jr. (1995), On the meridional extent and fronts of the Antarctic Circumpolar Current, *Deep-Sea Research I*, *42*, 641–673, doi:10.1016/0967-0637(95)00021-W.

Rodrigues, R. R., M. Wimbush, D. R. Watts, L. M. Rothstein, and M. Ollitrault (2010), South Atlantic mass transports obtained from subsurface float and hydrographic data, *Journal of Marine Research*, *68*(6), 819–850, doi: 10.1357/002224010796673858.

Smith, W. H., and D. T. Sandwell (1997), Global sea floor topography from satellite altimetry and ship depth soundings, *Science*, *277*(5334), 1956–1962, doi: 10.1126/science.277.5334.1956.

Sokolov, S., and S. R. Rintoul (2007), Multiple jets of the Antarctic Circumpolar Current South of Australia, *Journal of Physical Oceanography*, *37*, doi:10.1175/JPO3111.1.

Sokolov, S., and S. R. Rintoul (2009a), Cirumpolar structure and distribution of the Antarctic Circumpolar Current fronts: 1. Mean circumpolar paths, *Journal of Geophysical Research*, *114*, doi:10.1029/2008JC005108.

Sokolov, S., and S. R. Rintoul (2009b), Cirumpolar structure and distribution of the Antarctic Circumpolar Current fronts: 2. Variability and relationship to sea surface height, *Journal of Geophysical Research*, *114*, doi: 10.1029/2008JC005248.

Thompson, A. F., and A. C. Naveira-Garabato (2014), Equilibration of the Antarctic Circumpolar Current by standing meanders, *Journal of Physical Oceanography*, *44*, doi:10.1175/JPO-D-13-0163.1.

Thompson, A. F., and J.-B. Sallée (2012), Jets and topography: Jet transitions and the impact on transport in the Antarctic Circumpolar Current, *Journal of Physical Oceanography*, *42*, doi:10.1175/JPO-D-11-0135.1.

Tracey, K. L., K. A. Donohue, D. R. Watts, and T. K. Chereskin (2013), cDrake CPIES Data Report, *GSO Technical Report 2013-01*, University of Rhode Island, Graduate School of Oceanography, Narragansett, RI.

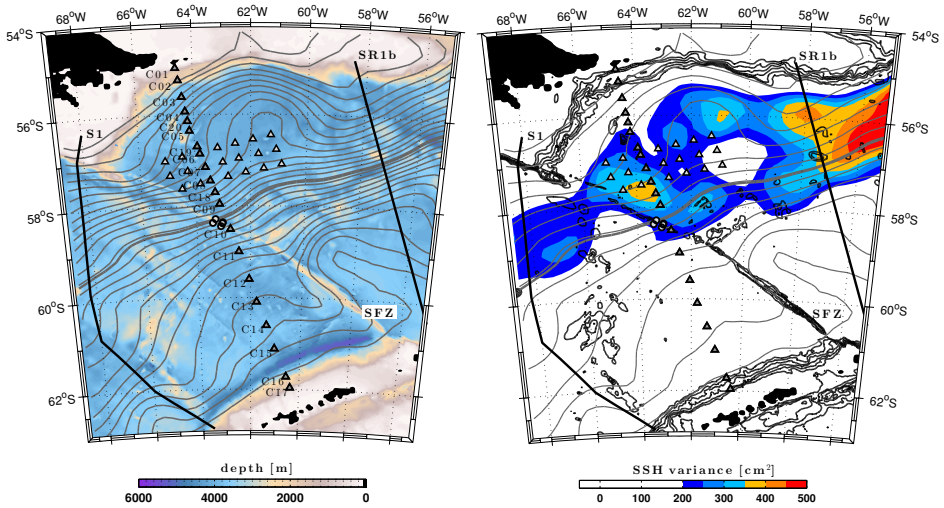

Figure 1.1. Map of Drake Passage. Left: Bathymetry [m] from *Smith and Sandwell* (1997) merged with multi-beam data is shown in color. Right: SSH variance [cm^2] during the 4 years of cDrake shown in color. 4-year mean SSH field is shown in grey (contour interval = 5 cm, left panel; 10 cm, right panel) with the -46.6 cm SSH contour in bold. CPIES sites are shown as triangles, with the C-Line darkened. The 4 CPIES in the H-Array, deployed the last year of cDrake, slightly northwest of C10, are denoted by circles. Location of WOCE lines S1 and SR1b are shown upstream and downstream of Drake Passage, respectively. The Shackleton Fracture Zone (SFZ), while labelled in southern Drake Passage, spans the entire Drake Passage.

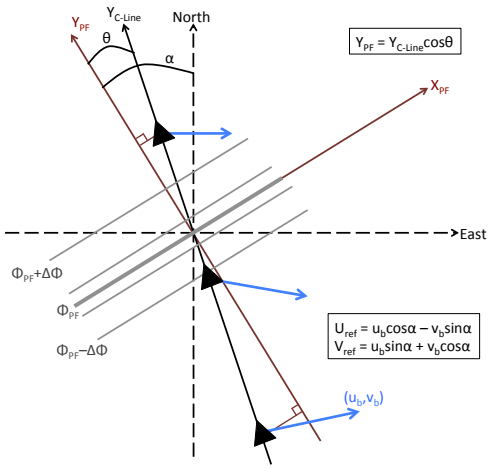

Figure 1.2. Schematic of projection of CPIES data onto the PF-axis. Triangles represent CPIES sites and grey lines represent the mapped Φ field along the C-Line. The along-stream and cross-stream axes (X_{PF}, Y_{PF}) are shown in red. Measured bottom velocities, $\vec{u}_b = (u_b, v_b)$, are presented as blue arrows. The bottom velocities, $\vec{u}_b$, are rotated into the stream-coordinate axis for each instantaneous orientation of the PF with angle α. The cross-front coordinate is $Y_{PF} = Y_{C-Line} \cdot \cos\theta$. Both angles are defined to be clockwise-positive.

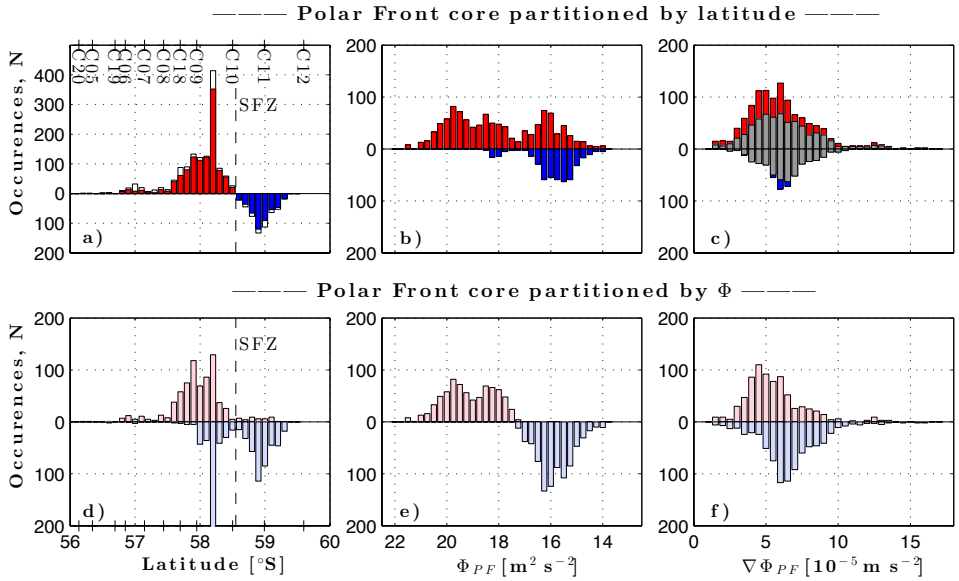

Figure 1.3. Distribution of the maximum $\nabla\Phi$ near the -46.6 cm SSH contour. The top row has been partitioned as a function of latitude, the bottom row as a function of Φ. Left column is the latitude associated with the maximum $\nabla\Phi$, center column is the Φ at maximum $\nabla\Phi$, and right column the corresponding $\nabla\Phi$. White bars with black outlines in the top left show the superset of times where the criterion of a slowly-varying angle has been relaxed (such that they represent anytime the SSH contour is quasi-perpendicular to the C-Line). Grey bars in the top right panel represent the subset of the times (excluding rings, S-shapes, and local obliquity) used in the composite means of the PF. Location of CPIES sites are shown in the left column; the SFZ crosses the C-Line at C10 (58.5°S).

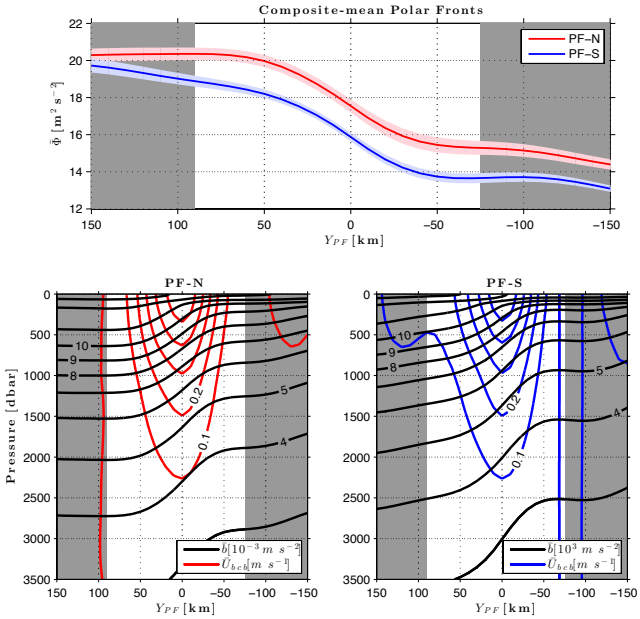

Figure 1.4. Top: Mean geopotential anomaly, Φ_{0-3500} [m^2 s^{-2}], of the northern and southern PF in stream coordinates shown in red and blue. Pale colored shading represents the respective standard errors of the mean. Degrees of freedom used to calculate standard error are shown in bottom left corner of the top panel. Middle and bottom: Mean buoyancy [10^{-3} m s^{-2}] and $\bar{U}_{bcb}$ [m s^{-1}] of the PF-N (middle) and PF-S (bottom). Contour interval for buoyancy is 1×10^{-3} m s^{-2}, while that for baroclinic velocity is 0.1 m s^{-1}. Grey shading denotes the extent of the PF's width.

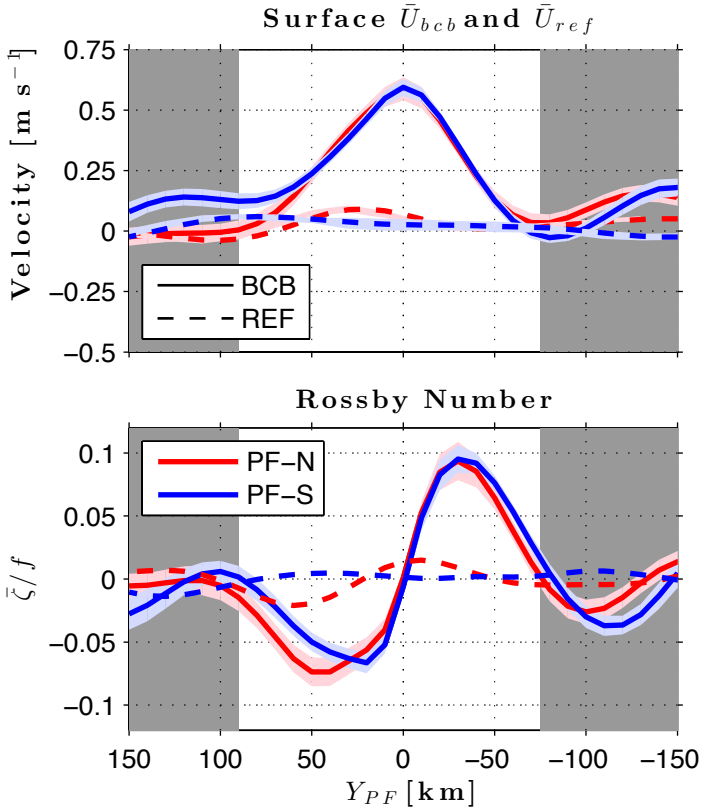

Figure 1.5. Top: Mean downstream velocity of PF-N and PF-S in stream coordinates (red and blue). Solid lines are U_{bcb} referenced to 3500 dbar of PF-N and PF-S; dashed lines are U_{ref}. Pale colored shading represents the respective standard errors of the mean for each calculation. Bottom: Shear vorticity as a fraction of local Coriolis parameter, $\bar{\zeta}/f$, for the surface $\bar{U}_{bcb}$ and $\bar{U}_{ref}$ fields. Grey shading denotes the extent of the PF's width.

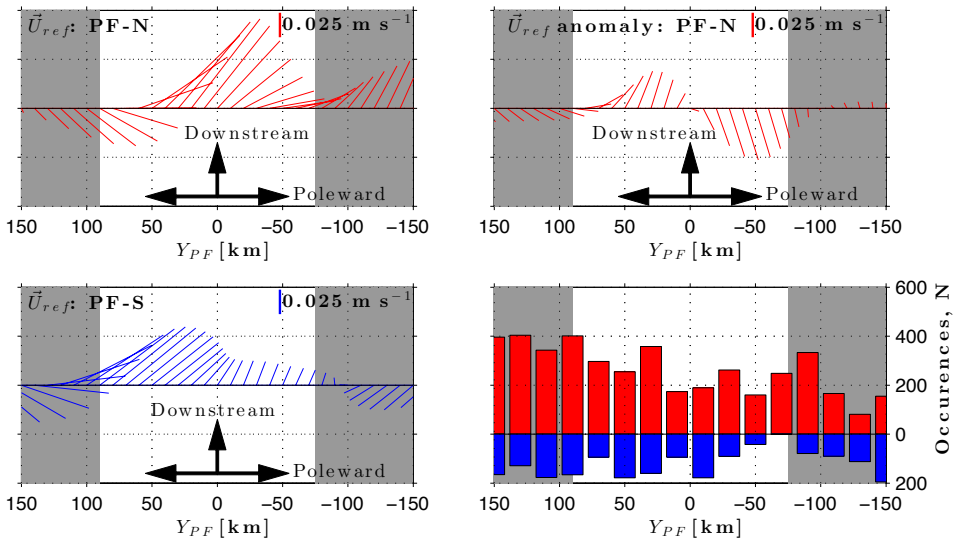

Figure 1.6. Left column: Mean reference velocities of the PF-N and PF-S in stream coordinates (top and bottom, respectively). Right column: (top) Reference velocity anomaly of PF-N, as explained in Section 5.3; (bottom) histogram of CPIES measurements occurring in each 20-km bin. Grey shading denotes the extent of the PF's width.

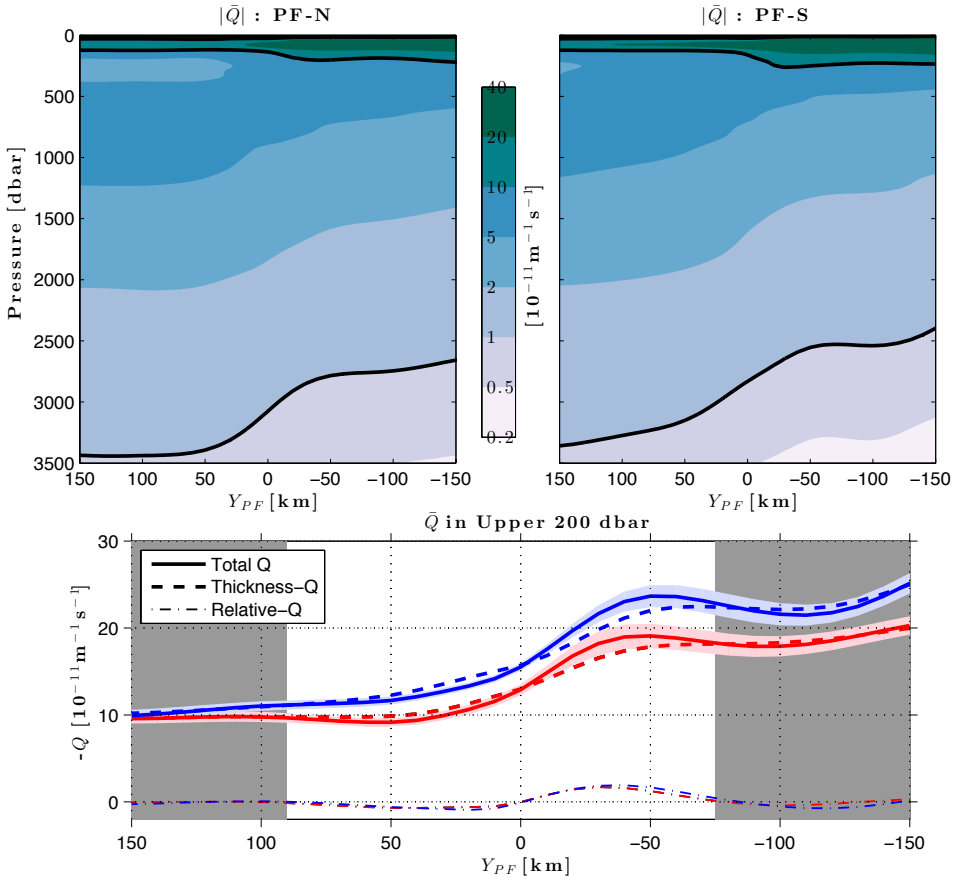

Figure 1.7. Top: Potential vorticity, $|Q|$ $[\mathrm{m}^{-1}\mathrm{s}^{-1}]$, contoured on a variable scale as a function of pressure and distance along the PF axis of PF-N and PF-S (left and right, respectively; consecutive contour intervals differ by roughly a factor of 2). Thick black lines represent $Q = 10^{-10}$ and 10^{-11} $\mathrm{m}^{-1}\mathrm{s}^{-1}$ contours. Bottom: Q and its two main components averaged in the upper 200 dbar (presented as $-Q$ such that total Q is positive). Total Q is shown as solid lines, thickness-Q is dashed, and relative-Q is dash-dotted. Grey shading denotes the extent of the PF's width.

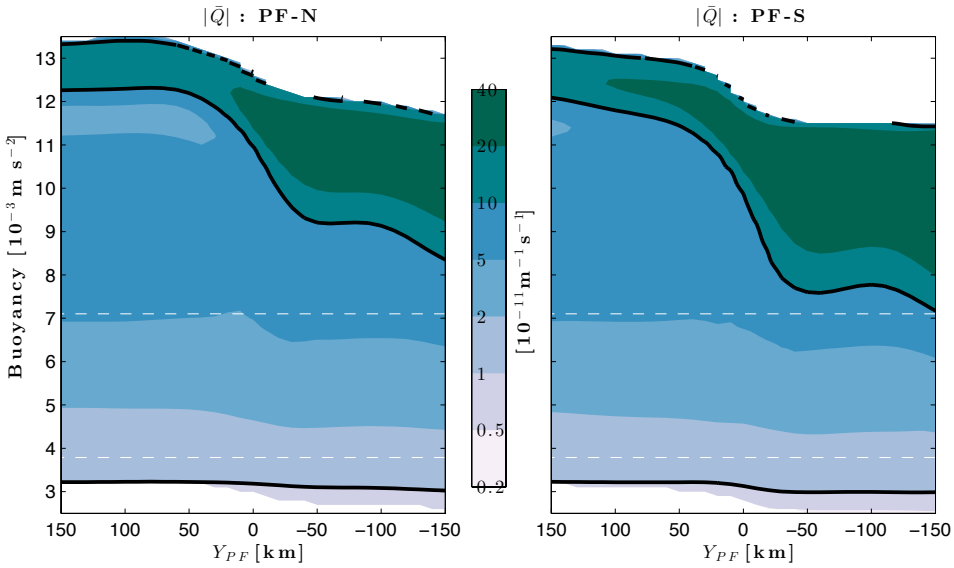

Figure 1.8. Potential vorticity, $|Q|$ [$\mathrm{m^{-1}s^{-1}}$], contoured on a variable scale as a function of buoyancy and distance along the PF axis of PF-N and PF-S (left and right, respectively; consecutive contour intervals differ by roughly a factor of 2). Thick black lines represent $Q = 10^{-10}$ and 10^{-11} $\mathrm{m^{-1}s^{-1}}$ contours.

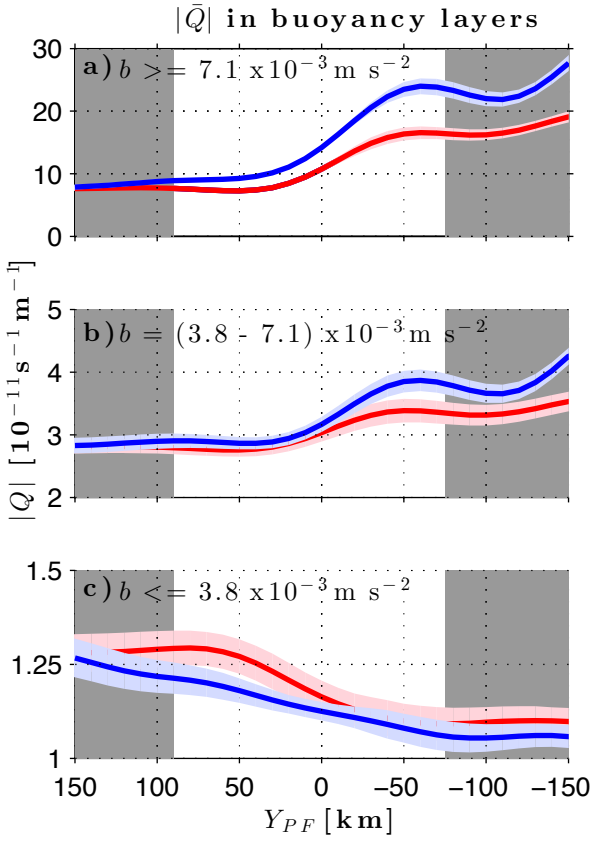

Figure 1.9. Potential vorticity, $|Q|$ [$\mathrm{m}^{-1}\mathrm{s}^{-1}$], averaged within buoyancy layers for the PF-N and PF-S (red and blue, respectively). Note the different limits on the y-axes. Also note that Q reverses its horizontal tendency in the densest layer, due to the deep buoyancy surfaces sloping into the ocean bottom in Figure 1.4. Grey shading denotes the extent of the PF's width.

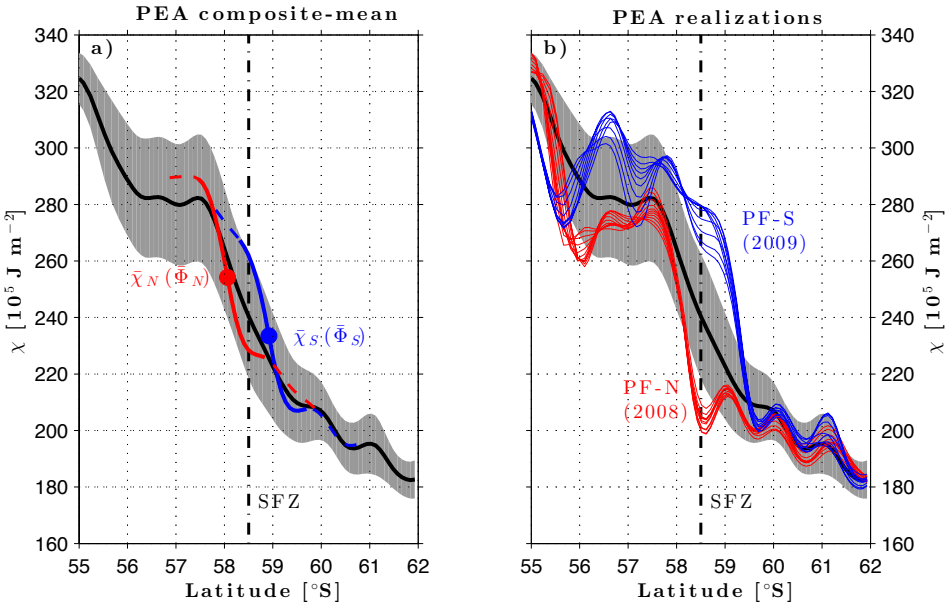

Figure 1.10. Potential energy anomaly (PEA or Fofonoff Potential, χ) along the C-Line. Time mean from the full 4 years of cDrake is shown in black, and its standard deviation shaded in grey. Colors represent examples of times included in the composite mean for the PF-N (28 March - 2 April 2008; red) and PF-S (28 March - 1 April 2009; blue), illustrating that they individually carry the full baroclinic transport rather than share it.

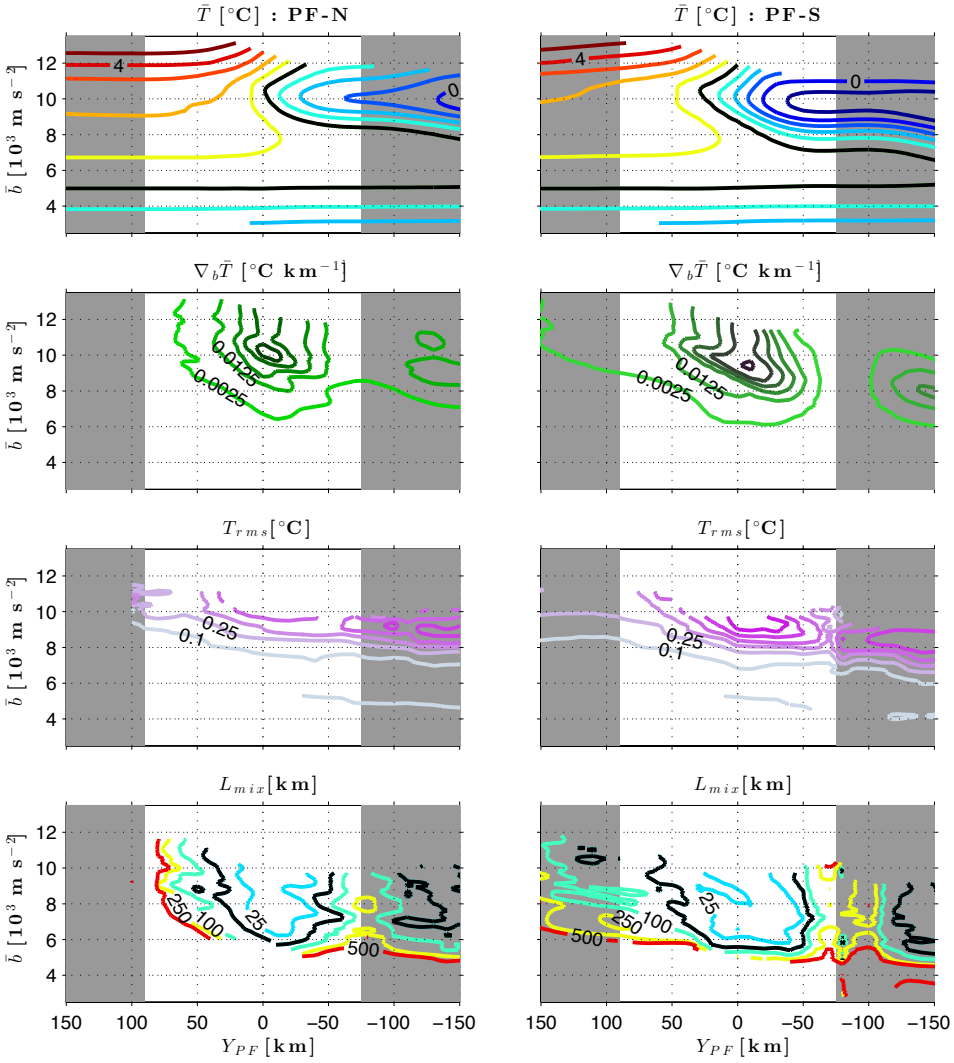

Figure 1.11. Mixing length calculations; PF-N left column, PF-S right. Top row: Temperature [°C] along the PF-axis in buoyancy space from the T-GEM (contour interval = 0.5°C). The 2°C isotherm is shown in black. Second row: Cross-stream ∇T [°C km^{-1}] on buoyancy surfaces (contour interval = 0.01°C km^{-1}). Third row: Temperature root-mean-square [°C] defined as the standard deviation of $[T(Y_i \pm \Delta Y, b) - \bar{T}(Y_i, b)]$, where ΔY = 40 km and $\bar{T}$ is the mean temperature (contour interval = 0.15°C). Bottom row: Mixing length [km] defined as $L_{mix} = T_{rms}/|\nabla T|$. The 50 km contour is shown in black (contours = 25, 50, 100, 250, and 500 km). Grey shading denotes the extent of the PF's width.

MANUSCRIPT 2

Eddy heat flux across the Antarctic Circumpolar Current estimated from sea surface height standard deviation

by

Annie Foppert[1], **Kathleen A. Donohue**[1], **D. Randolph Watts**[1], **and Karen L. Tracey**[1]

[1] *Graduate School of Oceanography, University of Rhode Island, Narragansett, RI*

In Revision at Journal of Geophysical Research: Oceans

2.1 Abstract

Eddy heat flux (EHF) is a predominant mechanism for heat transport across the zonally unbounded mean flow of the Antarctic Circumpolar Current (ACC). Observations of dynamically relevant, divergent, four-year mean EHF in Drake Passage from the cDrake project, as well as previous studies of atmospheric and oceanic storm tracks, motivates the use of sea surface height (SSH) standard deviation, H^*, as a proxy for depth-integrated, downgradient, time-mean EHF ($[\overline{EHF}]$) in the ACC. Statistics from the Southern Ocean State Estimate corroborate this choice and validate throughout the ACC the spatial agreement between H^* and $[\overline{EHF}]$ seen locally in Drake Passage. Eight regions of elevated $[\overline{EHF}]$ are identified from nearly 23.5 years of satellite altimetry data. Elevated cross-front exchange usually does not span the full latitudinal width of the ACC in each region, implying a hand-off of heat between ACC fronts and frontal zones as they encounter the different $[\overline{EHF}]$ hot spots along their circumpolar path. Integrated along circumpolar streamlines, defined by mean SSH contours, there is a convergence of $\oint[\overline{EHF}]$ in the ACC: 1.06 PW enters from the north and 0.02 PW exits to the south. Temporal trends in low-frequency [EHF] are calculated in a running-mean sense using H^* from overlapping 4-year subsets of SSH. Significant increases in downgradient [EHF] magnitude have occurred since 1993 at Kerguelen Plateau, Southeast Indian Ridge, and the Brazil-Malvinas Confluence, whereas the other five $[\overline{EHF}]$ hot spots have insignificant trends of varying sign.

2.2 Introduction

Oceanic and atmospheric circulations transport heat poleward to balance the excess radiative heat experienced at the equator. In the southern hemisphere, the nearly zonal geostrophic flow of the Antarctic Circumpolar Current (ACC) acts as a barrier to direct poleward heat transport by the mean flow towards Antarctica and the southern seas. *de Szoeke and Levine* (1981) propose eddy heat flux (EHF) across the ACC as the main mechanism for balancing the northward ageostrophic Ekman flux and air-sea flux of heat out of the Southern Ocean, thus balancing the heat budget. Satellite altimetry and model studies reveal the eddy field of the ACC to be patchy, with hot spots of eddy activity found in the lee of major bathymetric features (e.g. *Thompson and Sallée*, 2012). Understanding and quantifying EHF across the ACC, its relative contribution to the total heat flux across the ACC, and how it might be changing over time are essential for modeling and predicting how the Southern Ocean may modulate our future global climate.

Observations of the ACC are challenging to acquire and the lack thereof limits our ability to accurately quantify the relative contributions of eddy and mean heat flux to the total across the ACC. A mean heat flux due to the non-equivalent barotropic component of the mean velocity is small at any given point in the ACC, but an accumulation of these immeasurably small fluxes over a large area can lead to a significant, non-negligible heat flux across mean streamlines in a numerical model simulation (*Peña-Molino et al.*, 2014). Quantifying the mean heat flux with observations is particularly difficult due to the large area and the high resolution and accuracy of velocity and temperature measurements required for a meaningful estimate of the flux. The variability of EHF in the ACC in both time and space, with episodic pulses of EHF occurring on timescales of several days (*Watts et al.*, 2016) and with localized regions of eddy activity (*Thompson*

and Sallée, 2012), makes quantifying the total circumpolar integral of EHF through observations also a daunting task. Direct measurements of EHF in the ACC are limited to a handful of studies (*Watts et al.*, 2016; *Ferrari et al.*, 2014; *Sekma et al.*, 2013; *Phillips and Rintoul*, 2000), and the non-uniformity of the ACC eddy field complicates extrapolation from point measurements. Until the ACC and its eddy field are properly resolved with observations and the air-sea flux of heat is better constrained, closing the Southern Ocean heat budget will remain a matter of proxy measurements and bulk formula estimates. In this study, we use a high resolution numerical model and existing satellite altimetry to quantify EHF throughout the ACC.

Watts et al. (2016) demonstrate with direct observations in Drake Passage that baroclinic instability is the driving mechanism for large EHF events. These events release mean available potential energy (APE) from the system, reduce the slope of isopycnal surfaces by transporting heat down the mean temperature gradient, and produce eddy potential energy (EPE) (*Pedlosky*, 1987). The simplest theory of baroclinic instability has meanders growing into eddies over time, yet spatial growth of eddies is also possible. In the ACC, meanders are forced by the local bathymetric configuration and mean flow, supporting the link between large bathymetric features and localized hot spots of eddy activity, that are sometimes referred to as oceanic storm tracks.

Sea surface height (SSH) data are readily available throughout the ACC from satellite altimetry, and we use the temporal standard deviation of SSH, H^*, as a proxy for time-mean EHF. *Holloway* (1986) uses SSH height variability, scaled by gravity and a local Coriolis parameter, as a proxy for eddy diffusivity and estimates EHF via the mean temperature gradient. *Kushner and Held* (1998) apply that method analogously to two pressure levels in the atmosphere to reproduce maps

of the divergent component of the EHF with some success. Furthermore, as the dynamics in the zonally unbounded ACC are similar to those in the atmosphere, albeit with different scales, those authors suggest a straightforward extension to oceanic storm tracks. This method of estimating eddy diffusivity has been applied to SSH variability in the Southern Ocean (e.g. *Keffer and Holloway*, 1988; *Karsten and Marshall*, 2002). *Marshall et al.* (2006) and *Ferrari and Nikurashin* (2010) use other techniques for estimating eddy diffusivity from altimetric data, but again rely on a diffusive closure scheme to draw conclusions about eddy mixing. In this study, instead of seeking an eddy diffusivity or mixing coefficient to predict a downgradient flux, we use H^* directly as a proxy for the depth-integrated, divergent EHF in the ACC.

The eddy field of the ACC is likely to respond to the observed increase in circumpolar wind stress over the Southern Ocean (*Marshall*, 2003). While direct observations are ideal for studying the ACC's response to the increasing winds, a large scale monitoring system is not yet in place and would be costly to implement. A proxy estimate of low-frequency, running-mean EHF via satellite H^* allows for investigation of trends in the circumpolar eddy field from January 1993 through December 2014. *Hogg et al.* (2014) diagnose the eddy kinetic energy (EKE) field in several sectors of the ACC and find variable trends over the 20 years of satellite data. However, recent model simulations by *Treguier et al.* (2010) have shown that trends in EKE do not necessarily reflect trends in EHF, and therefore EKE may not be the best metric for studying changes in the EHF field. Moreover, *Ferrari and Nikurashin* (2010) find, through estimating eddy diffusivity, suppressed mixing in the core of the ACC where there is enhanced EKE, again suggesting that EKE is not the best metric for EHF.

The following section presents motivating observations from the cDrake

project (*Chereskin et al.*, 2012) in Drake Passage: elevated EHF and H^* are concentrated immediately downstream of the major bathymetric ridge, while the peak in mean surface EKE is offset further downstream (Section 2.1). This local relationship is confirmed throughout the circumpolar band of the ACC and a statistical relationship between EHF and H^* is developed using data from an eddy-permitting numerical model (Section 2.2). A power-law fit is applied to about 23.5 years of satellite data (Section 2.3). Circumpolar path-integrated values of EHF, its spatial pattern throughout the ACC, and long-term temporal trends in EHF at several "hot spots" are presented in Section 3. Section 4 provides a discussion of H^* as a proxy for EHF in the context of oceanic storm tracks, a comparison with the few other observations of EHF in the ACC, plus a discussion of the along- and cross-ACC structure of EHF and long-term trends. Section 5 summarizes the study.

2.3 Relating EHF to SSH variability

2.3.1 Observations in Drake Passage

An array of bottom-moored current- and pressure-recording inverted echo sounders (CPIES) was deployed in Drake Passage from November 2007 to November 2011 as part of the cDrake project (Figure 2.1a). Time series of hourly acoustic travel-time records measured by the IES and hourly near-bottom velocities measured by the current meter 50 m above the seafloor are three-day low-pass filtered and resampled every 12 hours, resulting in four-year records of τ and $\boldsymbol{u}_{ref}$, respectively, at each CPIES site. (The bold text indicates a horizontal vector quantity.) *Tracey et al.* (2013) describes the data collection and processing procedures in detail. A gravest empirical mode analysis based on regional hydrography provides a profile of temperature for every value of τ (*Chidichimo et al.*, 2014). The near-bottom $\boldsymbol{u}_{ref}$ is assumed to be geostrophic and depth-independent, such that the

total geostrophic velocity is the sum of the bottom-referenced baroclinic velocity profile and the reference velocity: $\boldsymbol{u}_{tot}(x,y,z,t) = \boldsymbol{u}_{bcb}(x,y,z,t) + \boldsymbol{u}_{ref}(x,y,t)$. A local dynamics array of CPIES was placed in the interfrontal zone between the mean position of the Subantarctic Front (SAF) and Polar Front (PF) in Drake Passage in a region of elevated eddy activity downstream of the Shackleton Fracture Zone (SFZ; Figure 2.1). The design of the local dynamics array, with 40 km spacing between sites, allows for three-dimensional optimal-interpolation mapping of twice-daily total geostrophic velocity and temperature fields (*Firing et al.*, 2014).

The dynamic importance lies in the divergent component of EHF, whereas the rotational component of EHF that circulates around contours of mean temperature variance is irrelevant dynamically (*Marshall and Shutts*, 1981). That is, only the divergent EHF influences the dynamics of eddy-mean flow interactions. Measurements by CPIES naturally separate the large purely rotational EHF ($\boldsymbol{u}'_{bcb}T'$) from the $\boldsymbol{u}'_{ref}T'$, such that the latter contains all the divergent EHF, albeit with the possibility of a small residual rotational component (*Bishop et al.*, 2013; *Watts et al.*, 2016). The prime denotes any deviation from the time mean, e.g. $T'(x,y,z,t) = T(x,y,z,t) - \bar{T}(x,y,z)$, where the overbar denotes the time-mean value. Time-mean, depth-integrated EHF is calculated, as in *Watts et al.* (2016), as:

$$[\overline{\boldsymbol{EHF}}] = \rho c_p \int_z \overline{\boldsymbol{u}'_{ref} \cdot T'} dz, \tag{2.1}$$

where square brackets denote a depth-integrated value and again the bold text indicates a horizontal vector quantity. Multiplication by a nominal density ($\rho =$ 1035 kg m^{-3}) and specific heat of seawater ($c_p = 4000$ J kg^{-1} °C^{-1}) expresses the units as a proper heat flux.

Figure 2.1b shows $[\overline{\boldsymbol{EHF}}]_{cDrake}$, where the subscript denotes the dataset. Here, the vertical integration is from the surface to a common depth of 3500 m.

We limit our analysis to the time-mean, depth-integrated $[\overline{\boldsymbol{EHF}}]_{cDrake}$ and present the results in units of MW m^{-1}. More details on EHF calculated from the cDrake CPIES, including the vertical structure and time series, can be found in *Watts et al.* (2016).

Figure 2.2 reinforces the claim made above, i.e. that $\boldsymbol{u}'_{bcb}T'$ is purely rotational and that $\boldsymbol{u}'_{ref}T'$ contains all of the divergence with a small rotational component remaining. The curl and the divergence of the total EHF ($\rho c_p \overline{\boldsymbol{u}'_{tot}T'}$) is compared with that of the baroclinic EHF ($\rho c_p \overline{\boldsymbol{u}'_{bcb}T'}$) and reference EHF ($\rho c_p \overline{\boldsymbol{u}'_{ref}T'}$). Here, for simplicity, the fluxes have been calculated at 400 m depth rather than depth-integrated, but the result is consistent. Figure 2.2 shows that, within the scatter due to mapping error, the divergence of the total $\overline{\boldsymbol{EHF}}$ is completely contained in the reference $\overline{\boldsymbol{EHF}}$. Likewise, the curl of the total $\overline{\boldsymbol{EHF}}$ is dominated by the curl of the baroclinic $\overline{\boldsymbol{EHF}}$. We also note that *Firing et al.* (2014) found good agreement between the mooring-based and CPIES-based velocities (R^2 between 0.67 and 0.85 in the upper 1000 m), temperatures (R^2 between 0.85 and 0.9), and *Watts et al.* (2016) found good agreement for the same comparison of velocity-temperature covariances (R^2 between 0.72 and 0.89). We are thus confident that the method for calculating the $[\overline{EHF}]$ using the near-bottom reference velocities in Equation 2.1 greatly reduces the amount of rotational flux while retaining the divergent flux.

CPIES measurements also allow for calculation of total SSH, SSH_{cDrake}, as the sum of a reference SSH from directly-measured bottom pressure and bottom-referenced baroclinic SSH, as described by *Donohue et al.* (2016). Figure 2.1c shows the standard deviation of the twice-daily SSH_{cDrake}, H^*_{cDrake} calculated with the CPIES data as:

$$H^* = \sqrt{\frac{1}{N-1}\sum_{i=1}^{N}(SSH_i - \overline{SSH})^2}, \tag{2.2}$$

where the subscript i represents the time index, and the overbar again denotes the time-mean value. We find that H^*_{cDrake} has a similar spatial pattern to $[\overline{\boldsymbol{EHF}}]_{cDrake}$: elevated values occur along the western edge of the local dynamics array immediately downstream of the SFZ (Figure 2.1b,c). While the spatial pattern of $[\overline{\boldsymbol{EHF}}]_{cDrake}$ has some interannual variability, depending on time period of averaging, the maximum $[\overline{\boldsymbol{EHF}}]_{cDrake}$ for any multiyear subset of the data is consistently on the western side of the CPIES array (see Figure 6 in *Watts et al.* (2016)). Moreover, the general agreement with the pattern of H^*_{cDrake} is also consistent for any multiyear subset of four-year record (not shown).

Figure 2.1d shows the mean surface EKE calculated from the cDrake CPIES data, $\overline{EKE}_{cDrake}$, as:

$$\overline{EKE} = \frac{1}{2}(\overline{u'^2 + v'^2}), \tag{2.3}$$

where $(u, v) = (u_{tot}, v_{tot})$ are the zonal and meridional geostrophic velocities at the sea surface. There are two peaks in $\overline{EKE}_{cDrake}$, with the highest value in the central longitudes of the local dynamics array, farther east than the peaks in $[\overline{\boldsymbol{EHF}}]_{cDrake}$ and H^*_{cDrake} (Figure 2.1b,c,d). Again, interannual variability in the spatial pattern of $\overline{EKE}_{cDrake}$ exists, but does not change its misalignment with $[\overline{\boldsymbol{EHF}}]_{cDrake}$ averaged over the same multiyear subset (not shown).

In Drake Passage, $[\overline{\boldsymbol{EHF}}]_{cDrake}$ and H^*_{cDrake} are concentrated in a relatively broad region immediately downstream of the SFZ, whereas $\overline{EKE}_{cDrake}$ exhibits smaller spatial scales. The peaks are separated by 1–2° of longitude. These observed spatial patterns from the cDrake project motivate our use of H^* as a proxy for $[\overline{\boldsymbol{EHF}}]$ throughout the entire ACC.

2.3.2 Circumpolar validation around the ACC

The Southern Ocean State Estimate (SOSE) validates that the spatial relationship between H^*_{cDrake} and $[\overline{\boldsymbol{EHF}}]_{cDrake}$ observed in Drake Pasage holds for the

entire ACC (Figure 2.3). SOSE is an eddy-permitting general circulation model based on the MITgcm for all longitudes and latitudes south of 25°S (*Mazloff et al.*, 2010). At 1/6° horizontal resolution and with 42 vertical levels, SOSE uses an iterative adjoint method to match the model's ocean state estimate to a suite of observational data sources — Argo floats, CPIES, satellite altimetry, etc — without introducing non-physical nudging terms into the equations of motion. Partial cells, rather than step functions, represent sloping bathymetry and give SOSE a better chance at capturing realistic near-bottom dynamics, making it well suited for this study. Several studies have shown that SOSE is an apt model for the investigation of ACC dynamics: *Peña-Molino et al.* (2014) examined the along- and across-stream components of the total geostrophic velocity and their respective mean heat fluxes, *Masich et al.* (2015) investigated topographic form stress, and *Abernathey et al.* (2016) considered water-mass transformation in the upper branch of the overturning circulation. We employ the most up-to-date output, Iteration 100, that contains six years of data from January 1, 2005 to December 31, 2010. Daily sea surface height, $SSH_{SOSE}(x, y, t)$, is available online (http://sose.uscd.edu) and its standard deviation, H^*_{SOSE}, given by Equation 2.2, is shown in Figure 2.3a.

The EHF calculation using SOSE output is analogous to the CPIES methodology to retain all of the dynamically-relevant divergent component of the flux (albeit with the possibility of a small residual rotational flux). Daily hydrostatic pressure potential anomaly and temperature throughout the water column were obtained directly from M. Mazloff (personal communication, March 2016). Geostrophic velocity is calculated at every point in SOSE from the surrounding pressure potential anomalies, avoiding partial cells. Reference velocities, $\boldsymbol{u}_{SOSE}(x, y, t)$, are the deepest of these geostrophic velocities at every location in the SOSE grid and are considered independent of depth, i.e. constant throughout the water column.

The mean (median) height above the bottom of $\boldsymbol{u}_{SOSE}$ is 550 m (375 m) and the largest differences are found along steep sloping topography (not shown); the deepest layers of the model are 250 m thick.

Time-mean, depth-integrated $[\overline{\boldsymbol{EHF}}]_{SOSE}$ is then calculated with Equation 2.1, using SOSE reference velocity and temperature anomalies and the same nominal seawater density and specific heat as before (Figure 2.3b). An integration depth of 2046 m was chosen to capture the majority of the signal and for consistent calculations throughout the ACC. Only locations within the circumpolar band of mean streamlines ($\overline{SSH}_{SOSE} = -0.8$ to 0.2 m) and where the reference depth is as deep as or deeper than the integration depth are considered in the subsequent analysis. Finally, the horizontal flux vectors are projected across $\overline{SSH}_{SOSE}$ contours within the ACC band to give cross-frontal $[\overline{EHF}]_{SOSE}$ as a scalar quantity, such that the negative values in Figure 2.3b indicate downgradient fluxes (i.e. towards the southern seas and Antarctica).

In linear instability theory (*Pedlosky*, 1987), baroclinic instability acts to transport heat down the mean temperature gradient (or $\nabla\overline{SSH}$), yet about 20% of the $[\overline{EHF}]_{SOSE}$ values are up the mean gradient of $\overline{SSH}_{SOSE}$ (Figure 2.4a). In general, these upgradient values have smaller magnitudes and are associated with lower values of H^*_{SOSE} than the downgradient $[\overline{EHF}]_{SOSE}$ values. Figure 2.4b shows that, when averaged within 2.5×10^{-3} m wide H^*_{SOSE} bins and excluding bins with less than 30 points, the magnitudes of positive values of $[\overline{EHF}]_{SOSE}$ are significantly smaller than those that are negative, especially as H^*_{SOSE} increases. The sum of all downgradient $[\overline{EHF}]_{SOSE}$ points is an order of magnitude greater than the sum of upgradient points. For the rest of this study, we only consider downgradient fluxes.

There is a spatial alignment between downgradient $[\overline{EHF}]_{SOSE}$ and H^*_{SOSE}

in the ACC: regions of elevated H^*_{SOSE} align with regions of elevated $[\overline{EHF}]_{SOSE}$ (Figure 2.3). A statistically significant power law exists between downgradient $[\overline{EHF}]_{SOSE}$ and H^*_{SOSE}, i.e. the variables are linearly related in log-log space (Figure 2.4b,c). The distribution is skewed such that there are many more points with low values of H^*_{SOSE} and $[\overline{EHF}]_{SOSE}$ (Figure 2.4a), as expected from the handful of regions with elevated values of $[\overline{EHF}]_{SOSE}$ and H^*_{SOSE} in Figure 2.3. For example, within 2.5×10^{-3} m wide H^*_{SOSE} bins, there are 60 times more points of downgradient $[\overline{EHF}]_{SOSE}$ with H^*_{SOSE} between 0.1 m and 0.15 m than there are with H^*_{SOSE} between 0.2 m and 0.25 m (Figure 2.4a). To avoid biasing the fit with lower values of H^*_{SOSE}, $[\overline{EHF}]_{SOSE}$ values are averaged within H^*_{SOSE} bins prior to calculating the power-law fit (Figure 2.4b,c). Outliers, shown as light gray points in Figure 2.4c, are excluded by only using $[\overline{EHF}]_{SOSE}$ values found between the 5th and 95th percentile in each bin and by excluding H^*_{SOSE} bins that have fewer than 30 points. The bin-averaged power law is

$$[\overline{EHF}] = A \cdot {H^*}^B, \tag{2.4}$$

where $[\overline{EHF}] = [\overline{EHF}]_{SOSE-fit}$ is the scalar quantity of downgradient, depth-integrated flux in units of MW m^{-1} and $H^* = H^*_{SOSE}$ is in meters. The best-fit coefficients, $A = -(1.85 \pm 0.17) \times 10^4$ and $B = 3.95 \pm 0.12$, give a bin-averaged R^2 value of 0.93. The negative value of A guarantees downgradient values everywhere. In log-log space, B is the slope of the line and $|A| = 10^\alpha$, where α is the y-intercept.

The observed $[\overline{EHF}]_{cDrake}$ values (described in Section 2.1) fall within the scatter of the circumpolar SOSE values (Figure 2.4c, red squares). Here, we present $[\overline{EHF}]_{cDrake}$ values that have been projected across the mean satellite SSH field (described in Section 2.3) averaged over the four years of the cDrake experiment. The data are from all CPIES sites with downgradient values of $[\overline{EHF}]_{cDrake}$, including those along the full-passage transect shown in Figure 2.1a. Additionally,

the vertical integration is from the surface to 2000 m, rather than to 3500 m as in Figure 2.1b, for an appropriate comparison with $[\overline{EHF}]_{SOSE}$. On average, surface-to-3500 m integral values of $[\overline{EHF}]_{cDrake}$ are 1.3 times greater than surface-to-2000 m integral values.

A noticeable feature of Figure 2.4c is the apparent truncation of H^*_{SOSE} near 0.09 m, whereas H^*_{cDrake} and other observations extend to lower values. The lowest value observed at the southern CPIES sites ($H^*_{cDrake} = 0.0697$ m) is about 80% of the lowest value of H^*_{SOSE} (= 0.0875 m). This elevated floor of H^*_{SOSE} is mainly due to high frequency, rapidly propagating waves within the model, but not in the cDrake observations (not shown). Arguably, the dynamics in SOSE capture the baroclinic instability process driving the $[\overline{EHF}]_{SOSE}$ signal with or without the presence of these high frequency waves. Moreover, low-pass filtering the SSH_{SOSE} data does not improve the power-law fit in terms of mean square error or R^2 value, so H^*_{SOSE} is calculated from the unfiltered daily SSH_{SOSE} fields. Additionally, the higher values of H^*_{SOSE} have similar magnitudes as H^*_{cDrake}, and it is in these regions of greatest SSH variability where the strongest $[\overline{EHF}]$ occurs.

Comparison of $[\overline{EHF}]$ calculated directly in SOSE with that estimated from H^*_{SOSE} using Equation 2.4 provides further confidence in the H^* proxy. Integrated along circumpolar contours of $\overline{SSH}_{SOSE}$, the estimated $\oint[\overline{EHF}]_{SOSE-fit}$ values agree well with the directly calculated $\oint[\overline{EHF}]_{SOSE}$ values, where $\oint(\cdot)$ denotes a circumpolar path-integrated value (Figure 2.5a). For orientation within the ACC mean flow field, the mean geostrophic speed in the uppermost vertical layer (5 m depth) along each $\overline{SSH}_{SOSE}$ contour is shown in Figure 2.5b. A nominal streamline for the SAF is $\overline{SSH}_{SOSE} = 0.0$ m contour, with along-stream speeds of about 0.2 m s^{-1}. The estimated $\oint[\overline{EHF}]_{SOSE-fit}$ is slightly weaker than its directly calculated counterpart across some streamlines and slightly stronger across oth-

ers, with a root-mean-square difference of 0.02 PW (Figure 2.5a). The largest differences between path-integrated values are near the SAF, where the magnitude of $\oint[\overline{EHF}]_{SOSE-fit}$ is 0.06 PW stronger than that of $\oint[\overline{EHF}]_{SOSE}$ and remains less than 10% of the mean absolute value of -0.7 PW. Both $\oint[\overline{EHF}]_{SOSE}$ and $\oint[\overline{EHF}]_{SOSE-fit}$ are weakest along the southern edge of the ACC where the path-integrated heat flux is about -0.2 PW. The magnitudes of $\oint[\overline{EHF}]_{SOSE-fit}$ and $\oint[\overline{EHF}]_{SOSE}$ increase by more than a factor of 3 as $\overline{SSH}_{SOSE}$ increases across the southern and central streamlines, and decrease slightly on the northern flank of the ACC (north of the SAF). This pattern of $\oint[\overline{EHF}]$ is indicative of a convergence of heat in streamlines south of the SAF and a divergence north of the SAF.

2.3.3 Application to satellite data

The power-law fit given by Equation 2.4 is now applied to satellite SSH data to estimate time-mean, depth-integrated EHF, $[\overline{EHF}]_{sat}$, in the ACC. Again, the direction of the flux is treated as downgradient (as ensured by the negative coefficient in Equation 2.4). Here, $SSH_{sat}(x, y, t)$ is the addition of the CNES-CLS13 mean dynamic topography to the Ssalto/Duacs gridded daily mean sea level anomaly (with a consistent reference period from 1993-2012). The mean dynamic topography was produced by CLS Space Oceanography Division and the sea level anomalies are produced and distributed by the Copernicus Marine and Environment Monitoring Service (as of May 2015); both are available online through AVISO at http://www.aviso.altimetry.fr. For this study, we use the two-satellite 'ref' product of mean sea level anomaly to additionally investigate long-term temporal trends in the record. The resulting SSH_{sat} record is almost 23.5 years of data from January 1993 to May 2016 at 1/4° horizontal resolution.

This analysis uses the SSH_{sat} field to calculate several variables: H^*_{sat}, $[\overline{EHF}]_{sat}$, $\oint[\overline{EHF}]_{sat}$, $[EHF_{sat}]$, and surface $\overline{EKE}_{sat}$. Standard deviation, H^*_{sat},

is calculated by applying Equation 2.2 to the full-length SSH_{sat} record. For consistency with analysis in SOSE, the power law is only applied to points within the circumpolar ACC band, defined as $\overline{SSH}_{sat} = -1.0$ to 0.3 m. The circumpolar band is chosen such that the $\overline{SSH}_{sat}$ contours are continuous throughout the Southern Ocean and pass through Drake Passage. Downgradient $[\overline{EHF}]_{sat}$ is estimated throughout the ACC from the H^*_{sat} field using the power law (Equation 2.4). $[\overline{EHF}]_{sat}$ and its path-integrated counterpart, $\oint[\overline{EHF}]_{sat}$, represent the nearly 23.5-year mean divergent eddy flux of heat, depth-integrated to 2000 m, and directed across mean $\overline{SSH}_{sat}$ contours towards Antarctica and the southern seas. Additionally, time series of low-frequency, running-mean $[EHF]_{sat}$ is estimated with the same equation, using a time series of H^*_{sat} calculated from 4-year subsets of SSH_{sat} overlapped by 2 years from 1993 through 2014. Finally, $\overline{EKE}_{sat}$ is calculated with Equation 2.3 using SSH_{sat}-derived geostrophic velocities, and is discussed in a few regions of elevated eddy activity in the context of oceanic storm tracks (Section 4.1).

2.4 Cross-ACC eddy heat flux

2.4.1 Circumpolar path-integrated $\oint[\overline{EHF}]_{sat}$

Integrated along circumpolar contours of $\overline{SSH}_{sat}$, the maximum magnitude of downgradient $\oint[\overline{EHF}]_{sat}$ of 1.06 PW occurs on the northern edge of the ACC (Figure 2.6a). Figure 2.6b shows the mean surface geostrophic speed, calculated from the $\overline{SSH}_{sat}$ fields, as well as labels for nominal ACC fronts determined from the mean along-stream surface geostrophic speed ($\overline{SSH}_{sat}$ of SAF=-0.1 m; PF=-0.4 m; SACCF =-0.7 m). The overall pattern of decreasing $\oint[\overline{EHF}]_{sat}$ magnitude with decreasing $\overline{SSH}_{sat}$ indicates a lateral convergence of heat due to eddies into the ACC (Figure 2.6a). The steeper slope on the northern side of the SAF, compared to the nearly constant slope south of the SAF, represents a stronger convergence

of $\oint[\overline{EHF}]_{sat}$ in the northern flank of the ACC.

An uncertainty in $\oint[\overline{EHF}]_{sat}$ of 0.02 PW is taken as the root-mean-square difference between $\oint[\overline{EHF}]_{SOSE}$ and $\oint[\overline{EHF}]_{SOSE-fit}$ (Figure 2.5a). For simplicity, this uncertainty is assumed to be independent of the circumpolar path of integration, i.e. independent of $\overline{SSH}_{sat}$ contour. Therefore, the $\oint[\overline{EHF}]_{sat}$ values on the southern edge of the ACC are statistically indistinguishable from zero (Figure 2.6a). Point-wise uncertainties in the $[\overline{EHF}]_{sat}$ estimates are not discussed, as most interest lies in the qualitative spatial distribution and quantitative circumpolar integrations. However, it can be noted that the rms difference between the bin-mean values of $[\overline{EHF}]_{SOSE}$ and the power-law fit is 10.5 MW m^{-1} (Figure 2.4b).

2.4.2 Spatial distribution of $[\overline{EHF}]_{sat}$

There are eight regions of relatively large values, i.e. hot spots, of $[\overline{EHF}]_{sat}$ around the ACC, shown by the red colored dots in Figure 2.7a. We define these hot spots as broad regions where $[\overline{EHF}]_{sat} \leq -10$ MW m^{-1} (approximately equivalent to $H^*_{sat} \geq 0.15$ m), more than double the ACC average of -5.1 MW m^{-1}. Six of these regions are associated with interactions between the ACC and major bathymetric features and two regions are associated with interactions with western boundary currents of subtropical gyres. Eastward from 0°E, the hot spots associated with major bathymetric features occur at the Southwest Indian Ridge (SWIR; 20–40°E), Kerguelen Plateau (KP; 81–96°E), Southeast Indian Ridge (SEIR; 115–160°E), Maquarie Ridge (MR; 160–180°E), Pacific Antarctic Rise (PAR; 205–230°E), and Drake Passage (DP; 285–315°E, south of 52°S); the hot spots associated with western boundary currents are the Agulhas Return Current (ARC; 10–83.5°E, northern flank of ACC) and the Brazil-Malvinas Confluence (BMC; 300–335°E, north of DP where they overlap longitudes). The longitudinal limits

of the $[\overline{EHF}]_{sat}$ hot spots are denoted by horizontal bars in Figure 2.7b; latitudinal limits only exist for regions that overlap in longitude. It can be noted that there is little interaction between the ACC and the Eastern Australian Current, the western boundary current of the subtropical South Pacific gyre, as the circumpolar band of $\overline{SSH}_{sat}$ excludes almost all of it from this study. Here, DP spans the Phoenix Antarctic Ridge, the Shackleton Fracture Zone, and the Scotia Arc (including Shag Rocks); the BMC region includes the entire Zappiola Anticyclone; MR region also includes the area south of Campbell Plateau; and the PAR includes both the Udintsev and Eltanin Fracture Zones.

Along circumpolar streamlines, the relative contribution of each hot spot to the total $\oint[\overline{EHF}]_{sat}$ varies (Table 2.1; Figure 2.7). Few regions of elevated $[\overline{EHF}]_{sat}$ influence all ACC streamlines. The main pulses of $[\overline{EHF}]_{sat}$ along the northern edge of the ACC are strongly tied to its interactions with the subtropical western boundary currents. That is, 89% of the total $\oint[\overline{EHF}]_{sat}$ crosses the $\overline{SSH}_{sat} = 0.3$ m contour at the ARC and BMC. It is not surprising that the ARC and BMC become increasingly less influential for more southern ACC streamlines. Across the SAF ($\overline{SSH}_{sat} = -0.1$ m), the two western boundary currents account for less than half (41%) of the total $\oint[\overline{EHF}]_{sat}$, and more occurs at the SAF's interaction with the SEIR (16%) than the ARC. $\oint[\overline{EHF}]_{sat}$ across a nominal PF ($\overline{SSH}_{sat} = -0.4$ m) accumulates from its interaction with all eight hot spots, with DP accounting for nearly a quarter of the total (23%). The SWIR and KP play a more prominent role in the $\oint[\overline{EHF}]_{sat}$ across the more southern streamlines of the ACC, with each accounting for between 21 and 26% of the total crossing the SACCF ($\overline{SSH}_{sat} = -0.8$ m) and exiting the southern edge of the ACC ($\overline{SSH}_{sat} = -1.0$ m). That different streamlines have different hot spots of $[\overline{EHF}]_{sat}$ suggests there is a hand-off of heat from one front or frontal zone to

another along the circumpolar path of the ACC.

The DP and BMC regions require a more detailed view, as the northern streamlines of the ACC turn sharply northward upon exiting the east side of DP before meeting the southward flowing Brazil Current and turning eastward again. Figure 2.7c shows an expanded view of the cumulative $[\overline{EHF}]_{sat}$ as a percent of the total $\oint[\overline{EHF}]_{sat}$ along mean ACC streamlines in the DP and BMC regions as a function of along-stream distance (rather than as a function of longitude, as in Figure 2.7b). The contours are drawn from 360°E back to 275°E, i.e. ending at the black dots in Figure 2.7a, such that 0 km is equivalent to 360°E. The DP region is designated by a thin gray and white dashed line and the BMC region by the thin black line within the colored lines; 52°S divides the two regions where their longitudinal ranges overlap. As noted previously, interactions with subtropical western boundary currents, i.e. BMC, are predominant sources of $[\overline{EHF}]_{sat}$ along the northern streamlines of the ACC and become less influential for more southern streamlines. The PF and the SACCF have a greater percentage of their respective total $\oint[\overline{EHF}]_{sat}$ occurring in DP than compared to the BMC (see also Table 2.1). The total $\oint[\overline{EHF}]_{sat}$ exiting the southern edge of the ACC has a 11% contribution from the BMC region, at the southeastern edge of the Zappiola Anticyclone, but recall the total path-integrated value on this contour is not significantly different from zero.

A small fraction of the total $\oint[\overline{EHF}]_{sat}$ along each $\overline{SSH}_{sat}$ contour is produced within regions outside of the hot spots. At the northern edge, 95% of the total $\oint[\overline{EHF}]_{sat}$ occurs within the hot spots; thus a mere 5% occurs outside these eight regions (Table 2.1. In contrast, at the southern edge, 16% of the total $\oint[\overline{EHF}]_{sat}$ is produced in regions outside the $[\overline{EHF}]_{sat}$ hot spots.

2.4.3 Low-frequency $[EHF_{sat}]$ time series

There is much interest in how the ACC eddy field responds to changes in zonal wind stress associated with the increasing wind stress noted by *Marshall* (2003). To investigate long-term trends in $[EHF]_{sat}$, each of the eight regions of enhanced fluxes is considered individually (boxes in Figure 2.8a). A time series of running-mean $[EHF]_{sat}$ and its linear trend are calculated at every point with enhanced $[\overline{EHF}]_{sat}$ ($\geq$ 10 MW m^{-1}; orange and red colors in Figure 2.8a). The time series and temporal trends are then averaged within each $[\overline{EHF}]_{sat}$ hot spot, resulting in eight regional-mean time series of low-frequency $[EHF]_{sat}$ and a respective trend (Figure 2.8b). Note that the trends are calculated using complete 4-year subsets of time and therefore only include data through the end of 2014. The trends are listed in the legend as a percentage of the regional-mean $[\overline{EHF}]_{sat}$ per year.

Figure 2.8b shows the low-frequency $[EHF]_{sat}$ anomaly time series for each hot spot. We include the most recent four years of data in the time series as an unfilled symbol connected by a dashed line to indicate that it was not used in the trend calculation, as it overlaps the preceding 4 year interval by more than 2 years (as labelled). The inter-annual variability in the time series makes the trends particularly dependent on the choice of endpoints for the linear regression, and only three of the $[\overline{EHF}]_{sat}$ hot spots have statistically significant trends: KP, SEIR, and BMC. Of these trends, KP has the highest R^2 value of 0.76, while SIER and BMC have R^2 values of 0.46 and 0.39, respectively. Additionally, there is a suggestion of a low-frequency signal with a period of 6–12 years in most of the records, especially that of the ARC (Figure 2.8b).

Regions without large trends are grouped in the upper panel and regions with large trends are grouped in the lower panel. (Here, large means the magnitude of the trend is greater than 0.25 MW m^{-1} yr^{-1} or greater than 1.0% of the regional

mean per year.) Large negative trends in running-mean $[EHF]_{sat}$, i.e. increasing $[EHF]_{sat}$ magnitudes over time, are seen at KP, SEIR, and MR. These bathymetric features are found between 60°E and 180°E in the Indian sector and entering the Pacific sector of the ACC.

The SWIR experiences a large, but insignificant, decrease in $[EHF]_{sat}$ magnitude of -1.2% of the regional mean per year over the 22 years of SSH_{sat} data (Figure 2.8b). It can be noted that including the last 4 years of SSH_{sat} data, from May 2012 to May 2016, with an adjusted period of overlap, results in a decrease in magnitude of the trend at the SWIR but does not change its sign. That is, even with the most recent data, the magnitude of $[EHF]_{sat}$ at the SWIR is decreasing (i.e. there is a positive trend in Figure 2.8b). DP and ARC also exhibit decreases in $[EHF]_{sat}$ magnitude, albeit smaller than that at the SWIR.

2.5 Discussion

2.5.1 H^* as a proxy for $[\overline{EHF}]$

The spatial distribution of time-mean, depth-integrated, downgradient, divergent EHF in the ACC is patchy, with enhanced fluxes in the lee of major bathymetric features and in regions where the ACC interacts with western boundary currents of subtropical gyres. That there are eddy activity hot spots is not new (e.g *Thompson and Sallée*, 2012; *Thompson and Naveira-Garabato*, 2014)), but here the fluxes have been quantified by using satellite altimetry, specifically H^*_{sat}, as a proxy for $[\overline{EHF}]_{sat}$ using the power law in Equation 2.4.

Previous studies have used SSH variability, scaled by g/f, as a proxy for eddy diffusivity and have estimated EHF via the mean temperature gradient (e.g *Holloway*, 1986; *Keffer and Holloway*, 1988). *Kushner and Held* (1998) successfully reproduce maps of the divergent component of the EHF by applying that method analogously to the atmosphere. Applied to the Southern Ocean, this method es-

timates about 0.5 PW of poleward EHF at 60°S (*Keffer and Holloway*, 1988). *Karsten and Marshall* (2002) estimate surface diffusivities in the Southern Ocean directly from the scaled SSH variability, and a constant of proportionality. We find that scaling H^*_{SOSE} by g/f did not improve the statistics of the bin-averaged power law and choose to quantify depth-integrated, time-mean, divergent $[\overline{EHF}]_{sat}$ directly from H^*_{sat} (Equation 2.4). Moreover, we estimate $[\overline{EHF}]_{sat}$ directly from an empirical relationship with H^*_{sat} rather than through a diffusive closure argument, thus bypassing the need to estimate an eddy diffusivity.

Abernathey and Cessi (2014) show that cross-stream eddy diffusivity is directly related to the downgradient $[\overline{EHF}]$ and cross-stream $[\nabla\bar{T}]$. Even with the advent of Argo floats, maps of subsurface temperature gradient at high resolution are not readily available for this calculation. Moreover, the use of depth-integrated quantities erases any vertical structure in the diffusivity. It has been shown in SOSE that there is a subsurface eddy diffusivity maximum associated with 'steering levels' where the mean flow matches the eddy propagation speed (*Abernathey et al.*, 2010). Therefore, we focus on $[\overline{EHF}]$ and simply note that, with some care taken in estimating $[\nabla\bar{T}]$, the spatial pattern of depth-integrated eddy diffusivity could later be quantified. Here, we can look at the qualitative pattern of path-integrated eddy diffusivity by assuming that $[\nabla\bar{T}]$ is proportional to the mean surface speed along each $\overline{SSH}_{sat}$ contour in Figure 2.6b. The patterns in Figure 2.6 imply larger eddy diffusivities north of the SAF and weaker diffusivities in the rest of the ACC. This qualitative result is in accordance with recent work showing eddy mixing suppression at the core of the ACC and enhanced mixing on the equatorward flank (e.g. *Marshall et al.*, 2006; *Ferrari and Nikurashin*, 2010).

Idealized model studies find that baroclinic conversion, and thus $\overline{EHF}$, occurs in the region of highest baroclinicity, and that there is a spatial offset between this

region and the region of highest eddy activity and $\overline{EKE}$ (e.g. *Chang and Orlanski*, 1993; *Chapman et al.*, 2015). Baroclinic instability converts mean APE to EPE through a flux of heat across the mean temperature (or $\overline{SSH}$) gradient (*Pedlosky*, 1987). SSH_{cDrake} variance, i.e. H^{*2}_{cDrake}, is dominated by the bottom-referenced baroclinic (or buoyancy) term rather than the bottom pressure term (comparison of Figure 3d and 3e in *Donohue et al.* (2016)). Consequently, H^{*2}_{cDrake} corresponds mainly to the surface expression of $\overline{EPE}$ ($=\overline{b'b'}/\bar{b}_z$, where b is buoyancy). Therefore, enhanced H^{*}_{cDrake} immediately downstream of SFZ seen in Figure 2.1c is interpreted as the production of EPE through conversion from mean APE due to baroclinic instability. This suggests why H^* is observed to be a good indicator of $[\overline{EHF}]$, because of growth by baroclinic instability in the most unstable regions.

Contours of $[\overline{EHF}]_{cDrake}$ and H^{*}_{cDrake} generally trend north-south (roughly parallel to the bathymetry of the SFZ) and are enhanced immediately downstream of the SFZ, while peak values of $\overline{EKE}_{cDrake}$ are found farther downstream, i.e. farther east in the CPIES array (Figure 2.1). This is in accordance with work on oceanic storm tracks by *Chapman et al.* (2015). Those authors show, using wave activity flux vectors calculated in a primitive equation model, that $\overline{EHF}$ (diagnosed as the vertical component of the wave activity vector) is highest directly downstream of an idealized ridge. In this region of enhanced baroclinic instability, meanders actively grow into eddies, EHF converts mean APE into EPE, and EKE is increasing in the along-stream direction. We posit that the growth and persistence of baroclinic eddies, in both time and space, results in a spatial offset between peaks of $[\overline{EHF}]$ (as well as $\overline{EPE}$ and H^*) and $\overline{EKE}$.

While baroclinic instability, $[\overline{EHF}]$, and $\overline{EPE}$ characteristically concentrate leading into the produced meander, the location of highest $\overline{EKE}$ is more variable. That is, the location where $\overline{EKE}$ is highest depends on additional factors

(bathymetric configuration, eddy-mean flow interactions, etc.) that can advance or retard eddy growth downstream. Figure 2.9 provides observational evidence at additional locations of the spatial offset between H^*_{sat} (and thus $[\overline{EHF}]_{sat}$) and $\overline{EKE}_{sat}$ in oceanic storm tracks from a zoomed-in subsection of three $[\overline{EHF}]_{sat}$ hot spots: SWIR, SEIR, and MR. We present H^{*2}_{sat} (top row), rather than H^*_{sat}, as it is analogous to EPE and therefore a parallel quantity to $\overline{EKE}_{sat}$ (bottom row).

Figure 2.9 shows the offset between peaks of H^{*2}_{sat} and $\overline{EKE}_{sat}$ at the SWIR and MR to be less than one degree of longitude, or about 50–100 km. This is about the same as, or slightly shorter than, the offset observed in DP from the cDrake CPIES data (Figure 2.1). The SEIR region is a bit more complicated, with the suggestion of both a northern and southern storm track. Figure 2.9e shows peaks of $\overline{EKE}_{sat}$ (plotted here as $2 \cdot \overline{EKE}_{sat}$ to use consistent limits for the colorbar) along both the $\overline{SSH}_{sat} = 0.2$ m and $\overline{SSH}_{sat} = -0.2$ m contours. Along the northern contour, there is a small peak in $\overline{EKE}_{sat}$ near 125°E and another elongated peak near 128°E that extends to 131°E. The offset between H^{*2}_{sat} and the first $\overline{EKE}_{sat}$ peak along this northern contour is similar to that seen in the other regions. The offset between H^{*2}_{sat} and the second $\overline{EKE}_{sat}$ peak along this contour is about 4° of longitude, closer to the suggested offset of about 350 km in the modeling work of *Chapman et al.* (2015). The pattern of heightened H^{*2}_{sat} followed by heightened $\overline{EKE}_{sat}$ is not clear in all eight hot spots, but we note that the ACC is much more complicated than an idealized model and that we do not expect to see the characteristic pattern of storm tracks everywhere, especially in regions of complicated bathymetry. Nevertheless, in the three regions of enhanced $[\overline{EHF}]_{sat}$ in Figure 2.9, as well as in DP observations, the peaks in H^{*2} (or H^* and thus $[\overline{EHF}]$) generally occur where $\overline{EKE}$ is increasing in the along-stream direction.

2.5.2 Comparison with observations

Observations of EHF in the Southern Ocean are sparse, and contamination by the dynamically irrelevant rotational EHF can confound interpretation. A large rotational component can be removed from the full EHF in CPIES measurements by using the depth-independent, near-bottom, reference velocities (the technique used by *Watts et al.* (2016) and described in Section 2.1) or from current-meter data by projecting the data into a low-passed shear-coordinate system (used by *Sekma et al.* (2013), *Phillips and Rintoul* (2000), and *Ferrari et al.* (2014)). When significant depth-mean values are converted to surface-to-2000 m depth-integrated values, the latter two studies find downgradient $[\overline{EHF}]$ from south of Tasmania and Drake Passage (respectively) ranging from 17 to 26 MW m^{-1}. *Sekma et al.* (2013) find insignificant depth-mean downgradient values of EHF in the narrow constraints of Fawn Trough (with a depth-integrated equivalent of 1 MW m^{-1} or less, depending on the reference frame). The significant values are plotted in Figure 2.4c (gray and blue triangles) on a log-log scale as a function of H^*_{sat}, where the standard deviation is taken over the sampling period corresponding to the respective studies. These values, as well as those from cDrake (red squares), fall within the upper limits of the scatter of all ACC locations in SOSE (Figure 2.4c).

If the rotational component is accurately known at every grid point and well enough resolved, its contribution to the circumpolar path-integrated EHF is exactly zero, by definition. The spatial distribution of EHF along contours may still be contaminated by the rotational component, but the total path-integrated value is purely divergent. However, if the measurements are noisy or not well resolved around the circumpolar path, the path-integrated rotational EHF may produce a large false contribution. Our results of circumpolar path-integrated $[\overline{EHF}]_{sat}$ magnitude decreasing from about 1.06 PW to 0.02 PW in the upper 2000 m of

the ACC agree well with the results of *Gille* (2003) from ALACE floats (0.9 PW decreasing to 0.3 PW across the ACC) and *Zhiwei et al.* (2014) from ARGO floats (0.38 PW in the ACC band of streamlines). It can be noted that the alternating poleward-equatorward EHF found in ARGO float data by *Zhiwei et al.* (2014) may be due to contamination of the signal locally by a large rotational component, and may not be dynamically relevant.

2.5.3 Across-stream structure of $\oint[\overline{EHF}]_{sat}$ Implications for Southern Ocean heat budget

In a balanced world, the amount of heat crossing a streamline's vertical-circumpolar surface is equal to the total air-sea heat flux out of the sea surface encompassed south that closed streamline. In this case, the circumpolar and vertical integral of total heat flux across streamlines of $\overline{SSH}_{sat}$ must balance the air-sea flux of heat out of the ocean to its south (neglecting a nominal mean geothermal heating from the seafloor of less than 50 mW m^{-2} (*Adcroft et al.*, 2001)). Estimates of air-sea flux come with uncertainties of up to 70% (*Large and Nurser*, 2001), yet the general consensus between models (e.g. *Volkov et al.*, 2010; *Meijers et al.*, 2007) and bulk formulae estimates (*Large and Nurser*, 2001) is on the order of tenths of petawatts out of the Southern Ocean. Several recent studies have used 0.4 PW as a typical value (e.g. *Watts et al.*, 2016; *Sekma et al.*, 2013). Historically, 60°S has been chosen as the latitude of integration because the ocean is unblocked by land at all longitudes there. However, around the globe the ACC spans a wide range of latitudes and it makes more sense conceptually to integrate along a circumpolar streamline instead.

The total heat flux across mean ACC streamlines is a combination of eddy and mean heat fluxes. While *de Szoeke and Levine* (1981) show that the mean heat flux is dominated by the ageostrophic Ekman heat flux ($\overline{EkHF}$), *Peña-Molino*

et al. (2014) show that there is also a non-negligible contribution from the non-equivalent barotropic veering of the mean baroclinic velocity field ($\overline{nonEBHF}$). *Levitus* (1987) use monthly climatological wind and sea surface temperature to estimate global Ekman heat flux. Integrating along latitudes, those authors find $\overline{EkHF} = 0.38$ PW at 50.5°S (i.e. northward heat flux) that decreases to 0.00 PW at 61.5°S. More recently, *Abernathey and Cessi* (2014) calculate a northward $\overline{EkHF}$ to be 0.3 PW at the PF in SOSE, agreeing with the climatology-based estimate of *Levitus* (1987). Additionally, *Peña-Molino et al.* (2014) show that the non-equivalent barotropic component of the mean geostrophic velocity contributes -0.2 PW entering the northern edge of the ACC and 0.0 PW exiting the southern edge, i.e. downgradient $\overline{nonEBHF}$. Thus, we consider the mean heat flux across the PF to be a combination of 0.3 PW of $\overline{EkHF}$ and -0.1 PW of $\overline{nonEBHF}$, to give a total of 0.2 PW in the northward/upgradient direction.

Our estimates of $\oint[\overline{EHF}]_{sat}$ find -0.24 ± 0.02 PW crossing the PF (Figure 2.6a; Table 2.1). When $\oint[\overline{EHF}]_{sat}$ is scaled up to "full-depth" ACC using the factor of 1.3 from the mean ratio of $[\overline{EHF}]_{cDrake}$ integrated from the surface to 3500 m to that integrated to 2000 m depth (see Section 2.2), we find -0.31 PW crosses PF (Figure 2.6a). Total heat flux across the PF, the combination of 0.2 PW (northward/upgradient) mean heat flux and -0.3 PW due to eddies, is -0.1 PW. Thus, ocean processes transport 0.1 PW across the PF towards Antarctica and the southern seas. The air-sea flux required to balance the total heat flux across the PF estimated here, i.e. an ocean loss of 0.1 PW to the atmosphere south of the PF, is well below the 0.4 PW cited above. We note that it falls just outside of the 70% uncertainty associated with the current estimate of air-sea flux. While the estimates given here have uncertainties of their own, as the sum of small terms where the sign seems well established, the uncertainties are less than the 0.3 PW

difference from 0.4 PW of air-sea heat flux. We suggest that 0.4 PW is an overestimate of the air-sea heat flux south of the PF. Direct observations of the air-sea heat flux over the Southern Ocean are needed to better constrain the Southern Hemisphere heat budget, as its magnitude is estimated here as a residual.

Inferences from lateral heat convergence

The shape of $\oint[\overline{EHF}]_{sat}$ as a function of $\overline{SSH}_{sat}$ in Figure 2.6a implies a convergence of heat by eddies across all the streamlines of the ACC. On the southern edge of the ACC, $\oint[\overline{EHF}]_{sat}$ approaches zero. This is in agreement with the modeling work of *Volkov et al.* (2010) where path-integrated $\overline{EHF}$ is negligible south of 65°S. Interestingly, the shape of the $\oint[\overline{EHF}]$ curve north of the SAF where the flux is dominated by interactions with the subtropical western boundary currents differs greatly between SOSE and satellite data. Comparison of Figure 2.5a and 2.6a reveals an enhanced convergence of $\oint[\overline{EHF}]_{sat}$ north of the SAF that is not apparent in $\oint[\overline{EHF}]_{SOSE}$ or $\oint[\overline{EHF}]_{SOSE-fit}$. *Volkov et al.* (2010) also show enhanced latitudinally integrated $\overline{E}HF$ convergence around 60°S. SOSE, on the other hand, has a divergence of $\oint[\overline{EHF}]_{SOSE}$ and $\oint[\overline{EHF}]_{SOSE-fit}$ north of the SAF. Close inspection of H^*_{SOSE} and H^*_{sat} (via $[\overline{EHF}]_{sat}$) reveals a different pattern and magnitude of the SSH variability, especially at the BMC (Figure 2.3a and 2.7a). The complex bathymetry of the Argentine Basin, the Zappiola Anticyclone, and the exact location of the fronts have a large impact on the $[\overline{EHF}]$ in the region. Further observations and higher resolution modeling studies are needed to determine processes controlling the pattern and strength of $[\overline{EHF}]$, especially in this particular region.

The convergence of $\oint[\overline{EHF}]_{sat}$ throughout the ACC implies an along-stream temperature change at the $[\overline{EHF}]_{sat}$ hot spots. Assuming there are no sources or sinks of heat at mid-depth in the ACC and a steady-state long-term mean in

stream-wise temperature, the temperature equation reduces to a balance between along-stream temperature advection and cross-stream (or downgradient) $\overline{EHF}$ convergence, i.e. $U(\partial T/\partial s) = -(\partial/\partial n)\overline{V'T'}$. Here, U and V are the down- and cross-stream components of the velocity at, say, 500 m depth. Note that in simplifying this equation, we assume divergence of along-stream $\overline{U'T'}$ is small and there is no mean cross-stream velocity. This can be rearranged to estimate the scale of downstream temperature changes, $\Delta T = -(\overline{EHF}/U)(L_s/L_n)$, where L_s and L_n are down- and cross-stream length scales. We use scales based on the observed mean structure of the PF and EHF in Drake Passage. The mean width of the PF is on the order of 100 km and has a mean downstream bottom-referenced U_{bcb} of 0.4 m s^{-1} at 500 m depth (taken from Figure 4 of *Foppert et al.* (2016)). A typical value of $\overline{V'T'}$ near the PF is about 0.01 m s^{-1} °C at 500 m depth (taken from Figure 10 of *Watts et al.* (2016)). This implies an increase in temperature on the order of 0.1°C along a 400 km path downstream of a major bathymetric ridge. This magnitude of temperature change may be observable with available hydrographic data (e.g. with Argo floats). Interestingly, *Foppert et al.* (2016) found, for relatively stable time periods, a depth-mean temperature difference of 0.3°C between a composite-mean PF upstream and downstream of the SFZ, some of which may be due to a convergence of $\overline{EHF}$ in the downstream jet.

The above posited increases in temperature at each of the $[\overline{EHF}]_{sat}$ hot spots are analogous to the deep changes in buoyancy found in the OFES model by *Thompson and Naveira-Garabato* (2014). This increased temperature (or buoyancy) associated with lateral $[\overline{EHF}]_{sat}$ convergence is not able to interact with the atmosphere directly through air-sea flux, as it occurs throughout the water column. It must, therefore, be incorporated into the mean circulation of the ACC and leave the ACC laterally through mean heat flux associated with the overturning

circulation (sometimes referred to as the Deacon cell). This is a topic of immediate interest, to both confirm the estimate of along-stream ΔT done here and to gain understanding of the relative importance of each hot spot of $[\overline{EHF}]_{sat}$.

2.5.4 Along-stream structure of $[\overline{EHF}]_{sat}$

In a broad sense, the locations of elevated $[\overline{EHF}]_{sat}$ correspond with where the $\overline{SSH}_{sat}$ contours pinch together (Figure 2.7a). This is especially apparent at the PAR where the latitudinal width between the SAF and the southern edge of the ACC reduces to less than half its upstream width before expanding again downstream, i.e. from more than 10° wide at 192°E to 4° wide at 215°E back to 10° wide by 232°E. *Thompson and Naveira-Garabato* (2014) find a similar pinching together and widening of mean streamlines associated with standing meanders set by steep bathymetry in the OFES model. The nearly flat sections of lines in Figure 2.7b, like that found in the Bellingshausen Basin (220−290°E), have a nearly inconsequential effect on the total $\oint[\overline{EHF}]_{sat}$. These are regions where *Thompson and Naveira-Garabato* (2014) showed a gradual steepening of buoyancy surfaces along the path of the ACC. These stretches of minimal $[\overline{EHF}]_{sat}$ accumulation can occur across the entire ACC, e.g. in the Bellingshausen Basin, or across a subset of $\overline{SSH}_{sat}$ contours. While $\oint[\overline{EHF}]_{sat}$ has nearly constant convergence south of the SAF (implied by the nearly constant slope in Figure 2.6a), when neighboring $\overline{SSH}_{sat}$ contours have different strengths of $[\overline{EHF}]_{sat}$, the convergence of heat between the streamlines is locally enhanced or reduced.

The relative contribution of heat to the total $\oint[\overline{EHF}]_{sat}$ at each hot spot depends on the $\overline{SSH}_{sat}$ contour, or path, chosen for integration. Western boundary current interactions are the prominent mechanism of $[\overline{EHF}]_{sat}$ across the northern streamlines of the ACC, whereas interactions with bathymetric features become increasingly important for the central and the southern streamlines. Figure 2.7b

and Table 2.1 show the percentage of total $\oint[\overline{EHF}]_{sat}$ at each hot spot. The different relative contributions of each hot spot to the total $\oint[\overline{EHF}]_{sat}$ confounds extrapolation from local observations. Prior knowledge of the number of hot spots around the ACC band alone is not enough; it is also necessary to know the relative contribution of each. Additionally, some of the more influential hot spots have been relatively under studied or under observed. In particular, much focus has been on fluxes across the ACC in DP (e.g. *Watts et al.*, 2016; *Ferrari et al.*, 2014; *Bryden*, 1979), when, in fact, the BMC contributes a greater percentage of the total $\oint[\overline{EHF}]_{sat}$ across the northern flank of the ACC and the SAF, and contributes a greater absolute value of $[\overline{EHF}]_{sat}$ to the Southern Ocean heat budget than DP (Figure 2.7; Table 2.1).

That the percent of total $\oint[\overline{EHF}]_{sat}$ at each $[\overline{EHF}]_{sat}$ hot spot depends on the chosen $\overline{SSH}_{sat}$ implies a hand-off of heat between mean streamlines of the ACC (Figure 2.7b and Table 2.1). In other words, heat that enters the ACC through $[\overline{EHF}]_{sat}$ in the BMC or ARC is able to cross the next front when it encounters a subsequent $[\overline{EHF}]_{sat}$ hot spot downstream. Eventually, it can exit the ACC southward at, most likely, either the SWIR or KP. To the extent that $[\overline{EHF}]_{sat}$ is driven by baroclinic instability events that act to transport heat across strong upper water column fronts, the heat may cross the more quiescent regions of the ACC through another process, e.g. the mean heat flux due to the non-equivalent barotropic component of the velocity described by *Peña-Molino et al.* (2014).

Each region of elevated $[\overline{EHF}]_{sat}$ found in this study has its own unique properties of background mean flow and bathymetry that together set the amplitude of the standing meander. For example, the strongest $[\overline{EHF}]_{cDrake}$ found in *Watts et al.* (2016) is in the Polar Frontal Zone, an inter-frontal zone between the SAF and PF, where there are warm-core rings pinching off the SAF and cold-core rings

pinching off the PF. *Chapman et al.* (2015) show that the amount of $\overline{EKE}$ produced and the amount of $\overline{EHF}$ (characterized by vertical wave activity flux) decrease with a decreasing amplitude of the standing meander. That is, the amount of $\overline{EHF}$ and $\overline{EKE}$ depends on the amplitude of the standing meander, forced by the unique configuration of bathymetry and mean flow, that triggers the baroclinic instability process. The extension to biological productivity is unclear, yet there have been observations that warm and cold core rings have different implications for chlorophyll distributions and primary production at the SWIR(*Ansorge et al.*, 2010). Thus, it is crucial to have a good understanding of the background mean flow in order to quantify, and perhaps predict, the amount of $[\overline{EHF}]$ crossing the ACC locally at each hot spot and the implications thereof.

2.5.5 Temporal trends of $[EHF]_{sat}$

There has been discussion in recent literature about the ACC eddy field's response to increasing and poleward-shifting winds in the Southern Ocean (e.g. *Meredith and Hogg*, 2006; *Hogg et al.*, 2014; *Meredith*, 2016). In this study, the long-term trend in low-frequency $[EHF]_{sat}$ in each hot spot is diagnosed in a running-mean sense using 4-year subsets of H^*_{sat} overlapped by 2 years (Figure 2.8). This reduces any variability occurring on time scales shorter than a few years, while retaining enough data to appropriately calculate trends. We find that the long-term trends from 1993 through 2014 vary in both sign and magnitude depending on location in the ACC, with only three of the eight $[\overline{EHF}]_{sat}$ hot spots showing significant trends of increasing poleward heat fluxes.

Hogg et al. (2014) find positive long-term linear trends in EKE from 1993 through 2012 in the Indian and Pacific sectors of the Southern Ocean, and no trend in the Atlantic, associated with intensifying circumpolar winds. Those authors define an Indian sector that includes the KP and part of SEIR, two regions where

we find significant increases in $[\overline{EHF}]_{sat}$ magnitude (Figure 2.8b). The BMC, the other hot spot with a significant trend of increasing $[\overline{EHF}]_{sat}$ magnitude, is not included in the Atlantic sector defined by *Hogg et al.* (2014). It is important to note that the trends in EKE represent trends in oceanic storm track intensity, and do not necessarily represent trends in EHF (*Treguier et al.*, 2010). In other words, the eddies may persist longer with enhanced EKE, but the amount of baroclinic growth and EHF could remain the same or even decrease. *de Souza et al.* (2013) find an increase in southward heat flux, based on an eddy diffusivity parameterization from sea level anomaly and mean temperature gradient, equivalent to 0.78% yr^{-1} of the total across the circumpolar PF. While that trend was calculated over a 4-year record from 2006 through 2009, the magnitude of the trend as a percentage of the mean falls within the range of values from the $[\overline{EHF}]_{sat}$ hot spots presented in the legend of Figure 2.8b.

Table 2.1 shows that 47% of the total $\oint[\overline{EHF}]_{sat}$ that crosses the southern edge of the ACC occurs in the Indian sector of the Southern Ocean (i.e. at SWIR and KP). Recent findings have pointed out several source locations for Antarctic Bottom Water with up to 40% produced in the Indian Sector (e.g. *Jacobs*, 2004; *Meredith*, 2013). The $[\overline{EHF}]_{sat}$ at SWIR and KP may act as direct sources of heat to the shelf and slope waters by baroclinic eddies. Both regions show large trends of $[EHF]_{sat}$ over the satellite record, respectively, of 0.26 MW m^{-1} and -0.27 MW m^{-1} (Figure 2.8). Note that the signs of these trends are opposite, with increasing $[EHF]_{sat}$ magnitude at KP and decreasing $[EHF]_{sat}$ magnitude at the SWIR. These changes in $[EHF]_{sat}$ could have consequences on amount of Antarctic Bottom Water formed in the Indian sector of the Southern Ocean.

2.6 Conclusion

SSH standard deviation (H^*) and time-mean, depth-integrated, divergent, downgradient eddy heat flux ($[\overline{EHF}]$) are related through a power law that is quantified using SOSE. The pattern of $[\overline{EHF}]_{sat}$ in the Southern Ocean estimated from satellite altimetry is strongly tied to large local bathymetric features and interactions with western boundary currents of the subtropical gyres. Heat enters the northern ACC from the subtropical gyres, mainly through interactions at the BMC and ARC, and appears to take a circuitous path before exiting the southern edge of the ACC. Pulses of $[\overline{EHF}]_{sat}$ occur at different locations along different $\overline{SSH}_{sat}$ contours. Integrated along circumpolar streamlines within the ACC band, $\oint[\overline{EHF}]_{sat}$ has a maximum value of 1.06 PW and a minimum of 0.02 PW, with an estimated uncertainty of 0.02 PW. This implies a convergence of heat due to eddies between circumpolar streamlines of the ACC, particularly for those north of the SAF. The values of $\oint[\overline{EHF}]_{sat}$ found here fall within the values of estimated from circumpolar extrapolation from local observations (e.g. *Watts et al.*, 2016; *Phillips and Rintoul*, 2000), found in model simulations (e.g. *Meijers et al.*, 2007; *Volkov et al.*, 2010), and calculated from float data (e.g. *Gille*, 2003; *Zhiwei et al.*, 2014).

Each region of elevated $[\overline{EHF}]_{sat}$ tied to ACC interactions with bathymetry has its own unique configuration of mean flow and bathymetry that sets the size of the standing meander and the strength of EHF. Significant long-term increases in $[EHF]_{sat}$ magnitude occurring at KP and SEIR may be related to the intensifying westerly winds over the ACC. On the other hand, the significant increases in $[EHF]_{sat}$ magnitude at the BMC and small insignificant trend of the opposite sign at the ARC are likely related to changes in the strength of the subtropical gyres and/or changes in water mass properties more so than to changes in circumpolar

wind stress over the Southern Ocean. It could be suggested that if the major fronts of the ACC shift southward due to changes in the winds, the locations of direct sources of heat out of the ACC towards the Antarctic slope and shelf could change. That is, the shifted jets may have to negotiate different parts of the ridge systems with concomitant changes regarding where $[\overline{EHF}]_{sat}$ hot spots occur in the ACC and how much heat crosses the southern edge of the ACC due to eddies.

Acknowledgements The authors are grateful for support from the National Science Foundation grants OCE1141802 and OCE1358470. The cDrake data are available at the National Centers for Environmental Information, online at http://www.nodc.noaa.gov. We thank M. Mazloff for his helpful comments and for providing us with auxiliary SOSE data; computational resources for the SOSE were provided by NSF XSEDE resource grant OCE130007. MATLAB codes and files for this manuscript can be found online at http://digitalcommons.uri.edu/physical_oceanography_techrpts/6/. We also thank two reviewers whose constructive comments helped to greatly improve this manuscript.

Bibliography

Abernathey, R. P., and P. Cessi (2014), Topographic enhancement of eddy efficiency in baroclinic equilibration, *Journal of Physical Oceanography*, *44*(8), 2107–2126, doi:http://dx.doi.org/10.1175/JPO-D-14-0014.1.

Abernathey, R. P., J. Marshall, M. R. Mazloff, and E. Shuckburgh (2010), Enhancement of mesoscale eddy stirring at steering levels in the Southern Ocean, *Journal of Physical Oceanography*, *40*(1), 170–184, doi:http://dx.doi.org/10.1175/2009JPO4201.1.

Abernathey, R. P., I. Cerovecki, P. R. Holland, E. Newsom, M. R. Mazloff, and L. D. Talley (2016), Water-mass transformation by sea ice in the upper branch of the Southern Ocean overturning, *Nature Geoscience*, doi:10.1038/ngeo2749.

Adcroft, A., J. R. Scott, and J. Marotzke (2001), Impact of geothermal heating on the global ocean circulation, *Geophysical Research Letters*, *28*, 1735–1738, doi:10.1029/2000GL012182.

Ansorge, I. J., E. A. Pakhomov, S. Kaehler, J. R. E. Lutjeharms, and J. V. Durgadoo (2010), Physical and biological coupling in eddies in the lee of the South-West Indian Ridge, *Polar Biology*, *33*, 747–759, doi:10.1007/s00300-009-0752-9.

Bishop, S. P., D. R. Watts, and K. A. Donohue (2013), Divergent eddy heat fluxes in the Kuroshio Extension at 144 - 146E. Part I: Mean structure, *Journal of Physical Oceanography*, *43*(8), 1533–1550, doi:10.1175/JPO-D-12-0221.1.

Bryden, H. L. (1979), Poleward heat flux and conversion of available potential energy in Drake Passage, *Journal of Marine Research*, *37*, 1–22.

Chang, E. K. M., and I. Orlanski (1993), On the dynamics of a storm track, *Journal of the Atmospheric Sciences*, *50*(7), 999–1015.

Chapman, C. C., A. M. Hogg, A. E. Kiss, and S. R. Rintoul (2015), The dynamics of Southern Ocean storm tracks, *Journal of Physical Oceanography*, *45*(3), 884–903, doi:10.1175/JPO-D-14-0075.1.

Chereskin, T. K., K. A. Donohue, and D. R. Watts (2012), cDrake: Dynamics and transport of the Antarctic Circumpolar Current in Drake Pasage, *Oceanography*, *25*(3), 134–135, doi:http://dx.doi.org/10.5670/oceanog.2012.86.

Chidichimo, M. P., K. A. Donohue, D. R. Watts, and K. L. Tracey (2014), Baroclinic transport time series of the Antarctic Circumpolar Current measured in Drake Passage, *Journal of Physical Oceanography*, *44*, 1829–1853, doi:10.1175/JPO-D-13-071.1.

de Souza, J. M. A. C., A. d. M. Paiva, and K. Von Schuckmann (2013), New estimates for the heat flux across the Polar Front: spatial and temporal variability in recent years, *Antarctic Science*, *25*(3), 433–444, doi:10.1017/S0954102012001113.

de Szoeke, R. A., and M. D. Levine (1981), The advective flux of heat by mean geostrophic motions in the Southern Ocean, *Deep Sea Researh I*, *28*, 1057–1085.

Donohue, K. A., M. A. Kennelly, and A. Cutting (2016), Sea surface height variability in Drake Passage, *Journal of Atmospheric and Oceanic Technology*, *33*(4), 669–683, doi:10.1175/JTECH-D-15-0249.1.

Ferrari, R., and M. Nikurashin (2010), Suppression of eddy diffusivity across jets in the Southern Ocean, *Journal of Physical Oceanography*, *40*(7), 1501–1519, doi:http://dx.doi.org/10.1175/2010JPO4278.1.

Ferrari, R., C. Provost, Y.-H. Park, N. Sennéchael, Z. Koenig, H. Sekma, G. Garric, and R. Bourdallé-Badie (2014), Heat fluxes across the Antarctic Circumpolar Current in Drake Passage: Mean flow and eddy contributions, *Journal of Geophysical Research: Oceans*, *119*, 6381–6402, doi:10.1002/2014JC010201.

Firing, Y. L., T. K. Chereskin, D. R. Watts, K. L. Tracey, and C. Provost (2014), Computation of geostrophic streamfunction, its derivatives, and error estimates from an array of CPIES in Drake Passage, *Journal of Atmospheric and Oceanic Technology*, *31*, 656–680, doi:10.1175/JTECH-D-13-00142.1.

Foppert, A., K. A. Donohue, and D. R. Watts (2016), The Polar Front in Drake Passage: A composite-mean stream-coordinate view, *Journal of Geophysical Research: Oceans*, *121*, 1771–17,881, doi:10.1002/2015JC011333.

Gille, S. T. (2003), Float observations of the Southern Ocean. Part II: Eddy fluxes, *Journal of Physical Oceanography*, *33*(6), 1182–1196, doi:10.1175/1520-0485(2003)033⟨1182:FOOTSO⟩2.0.CO;2.

Hogg, A. M., M. P. Meredith, D. P. Chambers, E. P. Abrahamsen, C. W. Hughes, and A. K. Morrison (2014), Recent trends in the Southern Ocean eddy field, *Journal of Geophysical Research: Oceans*, *120*, 257–267, doi:10.1002/2014/JC010470.

Holloway, G. (1986), Estimation of oceanic eddy transports from satellite altimetry, *Nature*, *323*, 243–244, doi:10.1038/323243a0.

Jacobs, S. S. (2004), Bottom water production and its links with the thermohaline circulation, *Antarctic Science*, *16*(4), 427–437, doi:10.1017/S095410200400224X.

Karsten, R. H., and J. Marshall (2002), Constructing the residual circulation of the

ACC from observations, *Journal of Physical Oceanography*, *32*(12), 3315–3327, doi:10.1175/1520-0485(2002)032⟨3315:CTRCOT⟩2.0.CO;2.

Keffer, T., and G. Holloway (1988), Estimating Southern Ocean eddy flux of heat and salt from satellite altimetry, *Nature*, *332*, 624–626, doi:10.1038/332624a0.

Kushner, P. J., and I. M. Held (1998), A test, using atmospheric data, of a method for estimating oceanic eddy diffusivity, *Geophysical Research Letters*, *25*(22), 4213–4216, doi:10.1029/1998GL900142.

Large, W. G., and A. J. Nurser (2001), *Ocean Circulation and Climate: Observing and Modeling the Global Ocean*, Academic Press.

Levitus, S. (1987), Meridional Ekman heat fluxes for the world ocean and individual ocean basins, *Journal of Physical Oceanography*, *17*(9), 1484–1492, doi: http://dx.doi.org/10.1175/1520-0485(1987)017⟨1484:MEHFFT⟩2.0.CO;2.

Marshall, G. J. (2003), Trends in the Southern Annular Mode from observations and reanalyses, *Journal of Climate*, *16*, 4134–4143, doi:10.1175/1520-0442(2003)016⟨4134:TITSAM⟩2.0.CO;2.

Marshall, J., and G. Shutts (1981), A note on rotational and divergent eddy fluxes, *Journal of Physical Oceanography*, *11*, 1677–1680, doi:10.1175/1520-0485(1981)011⟨1677:ANORAD⟩2.0.CO;2.

Marshall, J., E. Shuckburgh, H. Jones, and C. Hill (2006), Estimates and implications of surface eddy diffusivity in the Southern Ocean derived from tracer transport, *Journal of Physical Oceanography*, *36*(9), 1806–1821, doi: http://dx.doi.org/10.1175/JPO2949.1.

Masich, J., T. K. Chereskin, and M. R. Mazloff (2015), Topographic form stress in

the Southern Ocean State Estimate, *Journal of Geophysical Research: Oceans*, *120*, 7919–7933, doi:10.1002/2015JC011143.

Mazloff, M. R., P. Heimbach, and C. Wunsch (2010), An eddy-permitting Southern Ocean State Estimate, *Journal of Physical Oceanography*, *40*(5), 880–899, doi:10.1175/2009JPO4236.1.

Meijers, A. J., N. L. Bindoff, and J. L. Roberts (2007), On the total, mean, and eddy heat and freshwater transports in the Southern Hemisphere of a 1/8 x 1/8 global ocean model, *Journal of Physical Oceanography*, *37*(2), 277–295, doi:10.1175/JPO3012.1.

Meredith, M. P. (2013), Replenishing the abyss, *Nature Geoscience*, *6*, 166–167, doi:10.1038/ngeo1743.

Meredith, M. P. (2016), Understanding the structure of changes in the Southern Ocean eddy field, *Geophysical Research Letters*, *43*, 5829–5832, doi:10.1002/2016GL069677.

Meredith, M. P., and A. M. Hogg (2006), Circumpolar response of Southern Ocean eddy activity to a change in the Southern Annular Mode, *Geophysical Research Letters*, *33*, L16,608, doi:10.1029/2006GL026499.

Pedlosky, J. (1987), *Geophysical Fluid Dynamics*, 2cd ed., Springer-Verlag.

Peña-Molino, B., S. R. Rintoul, and M. R. Mazloff (2014), Barotropic and baroclinic contributions to along-stream and across-stream transport in the Antarctic Circumpolar Current, *Journal of Geophysical Research: Oceans*, *119*, 8011–8028, doi:10.1002/2014JC010020.

Phillips, H. E., and S. R. Rintoul (2000), Eddy variability and energetics from direct current measurements in the Antarctic Circumpolar Current south of

Australia, *Journal of Physical Oceanography*, *30*(12), 3050–3076, doi:10.1175/1520-0485(2000)030⟨3050:EVAEFD⟩2.0.CO;2.

Sekma, H., Y.-H. Park, and F. Vivier (2013), Time-mean flow as the prevailing contributiont to the poleward heat flux across the southern flank of the Antarctic Circumpolar Current: A case study in the Fawn Trough, Kerguelen Plateau, *Journal of Physical Oceanography*, *43*(3), 583–601, doi:10.1175/JPO-D-12-0125.1.

Smith, W. H., and D. T. Sandwell (1997), Global sea floor topography from satellite altimetry and ship depth soundings, *Science*, *277*(5334), 1956–1962, doi:10.1126/science.277.5334.1956.

Thompson, A. F., and A. C. Naveira-Garabato (2014), Equilibration of the Antarctic Circumpolar Current by standing meanders, *Journal of Physical Oceanography*, *44*(7), 1811–1828, doi:10.1175/JPO-D-13-0163.1.

Thompson, A. F., and J.-B. Sallée (2012), Jets and topography: Jet transitions and the impact on transport in the Antarctic Circumpolar Current, *Journal of Physical Oceanography*, *42*(6), 956–972, doi:10.1175/JPO-D-11-0135.1.

Tracey, K. L., K. A. Donohue, D. R. Watts, and T. K. Chereskin (2013), cDrake CPIES data report November 2007 to December 2011, *GSO Technical Report Paper 4*, University of Rhode Island Physical Oceanography.

Treguier, A. M., J. Le Sommer, J. M. Molines, and B. de Cuevas (2010), Response of the Southern Ocean to the Southern Annular Mode: Interannual variability and multidecadal trend, *Journal of Physical Oceanography*, *40*(7), 1659–1668, doi:10.1175/2010JPO4364.1.

Volkov, D. L., L.-L. Fu, and T. Lee (2010), Mechanisms of the meridional heat transport in the Southern Ocean, *Ocean Dynamics*, *60*, 791–801, doi:10.1007/s10236-010-0288-0.

Watts, D. R., K. L. Tracey, K. A. Donohue, and T. K. Chereskin (2016), Estimates of eddy heat flux crossing the Antarctic Circumpolar Current from observations in Drake Passage, *Journal of Physical Oceanography*, *46*(7), 2103–2122, doi:10.1175/JPO-D-16-0029.1.

Zhiwei, Z., Z. Yisen, T. Jiwei, Y. Qingxuan, and Z. Wei (2014), Estimation of eddy heat transport in the global ocean from Argo data, *Acta Oceanologica Sinica*, *33*(1), 42–47, doi:10.1007/s13131-014-0421-x.

Table 2.1. $[\overline{EHF}]_{sat}$ at hot spots of eddy activity along 5 $\overline{SSH}_{sat}$ contours[a]

Label ($\overline{SSH}_{sat}$ [m])	ARC	BMC	SWIR	KP	SEIR	MR	PAR	DP	total [PW]
N-Edge (0.3)	42	47	–	–	5	–	1	–	-1.06
SAF (-0.1)	14	27	1	6	16	14	4	12	-0.33
PF (-0.4)	1	13	15	6	15	12	6	23	-0.24
SACCF (-0.8)	–	7	22	21	15	3	6	15	-0.08
S-Edge (-1.0)	–	11	26	21	7	3	9	7	-0.02

[a]Hot spot values presented as a percent of the total circumpolar path-integrated values (last column). Hot spots with less than 0.5% of the total $\oint[\overline{EHF}]_{sat}$ are left empty. All regions are defined by their longitudinal limits shown in Figure 2.7b. The SWIR, ARC and KP have additional latitudinal limits, as do DP and BMC, so that there is no overlap between regions. See text for abbreviations.

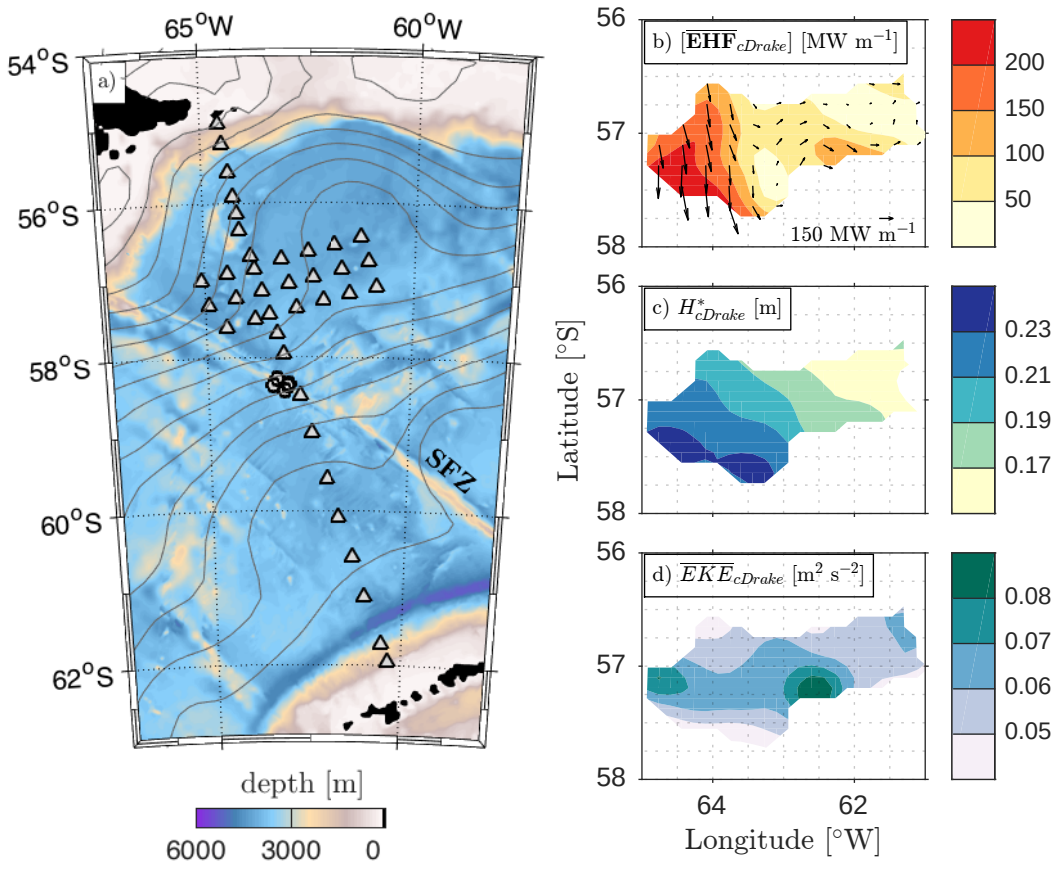

Figure 2.1. cDrake results. (a) Map of bathymetry [m] from *Smith and Sandwell* (1997) merged with multi-beam data (filled color contours) and the cDrake array of CPIES (triangles) in Drake Passage. The submarine ridge spanning Drake Passage, the Shackleton Fracture Zone (SFZ) is labelled in the southern passage. The circles represent the subset of CPIES deployed in the final year of the experiment. The nearly 23.5-year mean SSH field is shown as gray lines with a contour interval of 0.1 m. (b) $[\overline{\boldsymbol{EHF}}]_{cDrake}$ [MW m^{-1}]: 4-year mean depth-integrated (surface to 3500 m) eddy heat flux magnitude from the mapped CPIES variables with a contour interval of 50 MW m^{-1}. The arrows indicate the direction of $[\overline{\boldsymbol{EHF}}]_{cDrake}$ at every other point on the mapped grid. (c) H^*_{cDrake} [m]: SSH_{cDrake} standard deviation over the 4 years, from 2007 through 2011, with a contour interval of 0.02 m. (d) $\overline{EKE}_{cDrake}$ [m^2 s^{-2}]: 4-year mean surface eddy kinetic energy with contour interval of 0.01 m^2 s^{-2}.

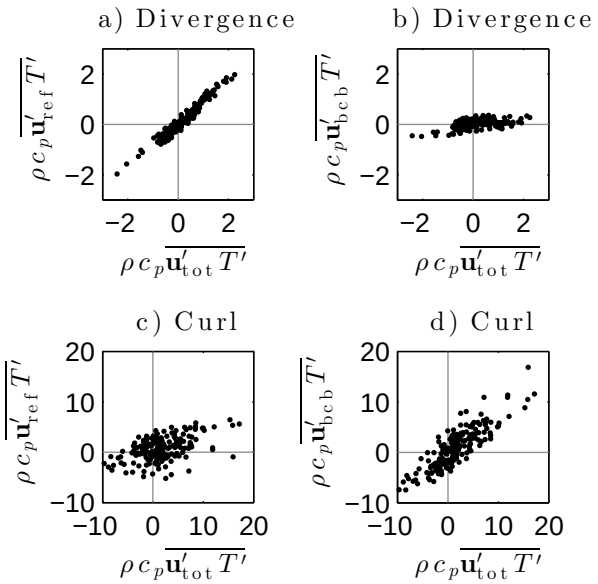

Figure 2.2. Divergence (a,b) and curl (c,d) of total EHF ($\rho c_p \overline{\boldsymbol{u}'_{tot} T'}$) compared to the reference EHF ($\rho c_p \overline{\boldsymbol{u}'_{ref} T'}$) and baroclinic EHF ($\rho c_p \overline{\boldsymbol{u}'_{bcb} T'}$) at 400 m depth within the local dynamics array of CPIES in Drake Passage in units of W m^{-3}. The total EHF on the x-axis is plotted against the reference EHF (a,c) and baroclinic EHF (b,d) on the y-axis.

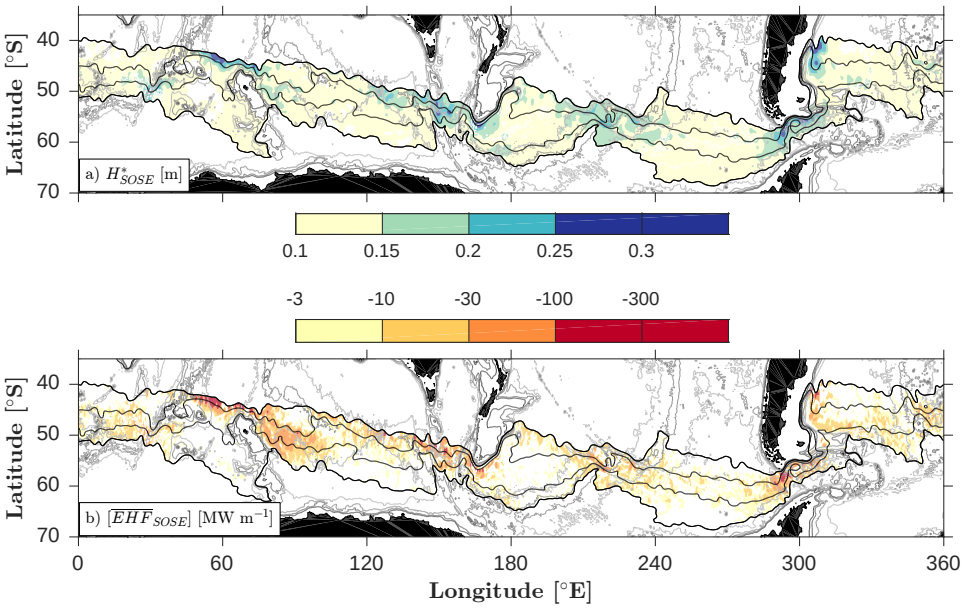

Figure 2.3. SOSE maps of the Southern Ocean with model depth contoured every 1000 m in gray and mean circumpolar streamlines defining outer edges of the ACC band ($\overline{SSH}_{SOSE} = -0.8$ to 0.2 m) and two more central contours ($\overline{SSH}_{SOSE} = -0.5$ and -0.1 m) in black. (a) H^*_{SOSE} [m]: daily SSH_{SOSE} standard deviation over the 6 years of SOSE Iteration 100, from 2005 through 2010. Values less than 0.1 m are left unshaded and those greater than 0.25 m are dark blue. Note that all values greater than 0.3 m are only found in the Agulhas Return Current and Brazil-Malvinas Confluence regions. (b) $[\overline{EHF}]_{SOSE}$ [MW m^{-1}]: time-mean depth-integrated (surface to 2000 m) cross-frontal eddy heat flux calculated in SOSE. Only negative (i.e. down gradient) values are plotted. Values with a magnitude less than 3 MW m^{-1} are left unshaded and those greater than 100 MW m^{-1} are dark red. Note that all values greater than 300 MW m^{-1} are only found in the Agulhas Return Current and Brazil-Malvinas Confluence regions.

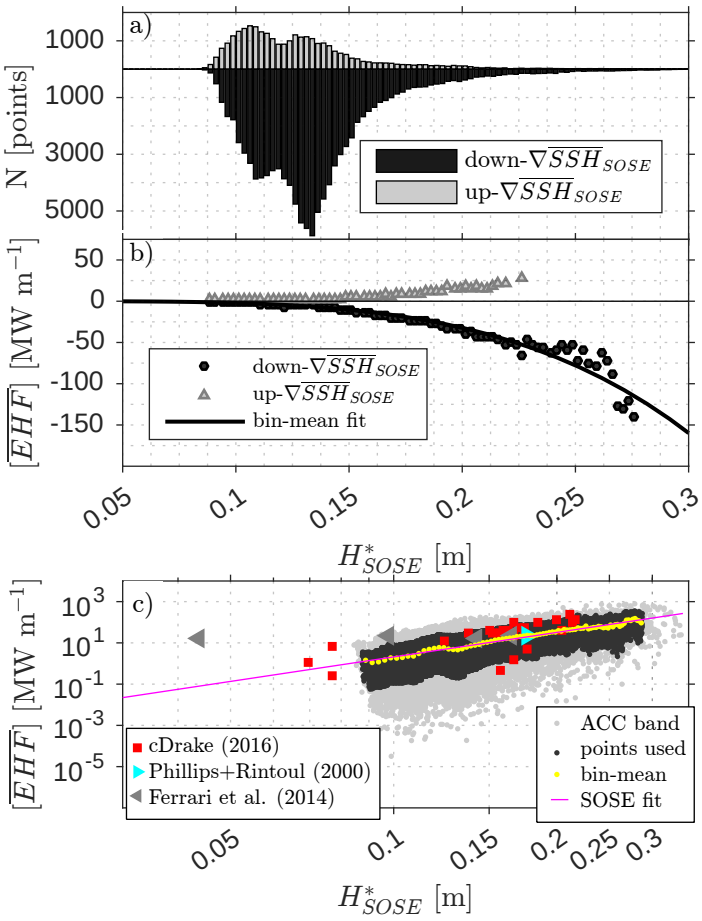

Figure 2.4. (a) Cross-frontal eddy heat flux calculated in SOSE, $[\overline{EHF}]_{SOSE}$, as a function of SSH_{SOSE} standard deviation, H^*_{SOSE} [m], within the ACC band of mean streamlines ($\overline{SSH}_{SOSE} = -0.8$ to 0.2 m). Gray/black bars indicate a heat flux up/down the $\overline{SSH}_{SOSE}$ gradient. (b) $[\overline{EHF}]_{SOSE}$ [MW m^{-1}] averaged within 0.025 m-wide H^*_{SOSE} bins. Upgradient (gray triangles) and downgradient (black circles) $[\overline{EHF}]_{SOSE}$ are averaged independently and only bins containing greater than 30 points are considered. The black line represents the bin-averaged power-law fit used in this study. (c) Downgradient $[\overline{EHF}]$ values as a function of H^* from several sources are plotted on a log-log scale. Points from SOSE within the ACC used for the bin-averaged fit (black dots), points considered outliers (light gray dots), and bin-averaged points (yellow dots) are all shown. The magenta line represents the bin-mean power-law fit (Equation 2.4). cDrake points (red squares) and other significant observations of $[\overline{EHF}]$ in the ACC (triangles) are plotted as a function of H^*_{sat} over their respective time periods.

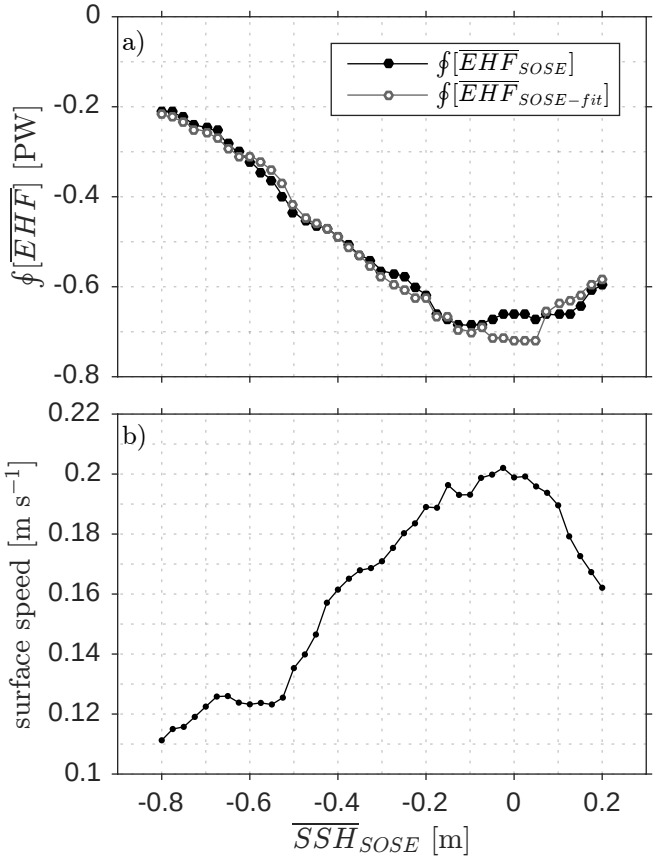

Figure 2.5. (a) Circumpolar path-integrated $\oint[\overline{EHF}]$ [PW= 10^{15} W] calculated directly in SOSE ($\oint[\overline{EHF}]_{SOSE}$; black filled circles) and estimated from the bin-averaged power law fit to H^*_{SOSE} ($\oint[\overline{EHF}]_{SOSE-fit}$; gray open circles). Negative values indicate a flux in the downgradient direction, i.e. towards Antarctica and the southern seas. (b) Mean geostrophic speed [m s^{-1}] at 5 m depth along circumpolar $\overline{SSH}_{SOSE}$ contours.

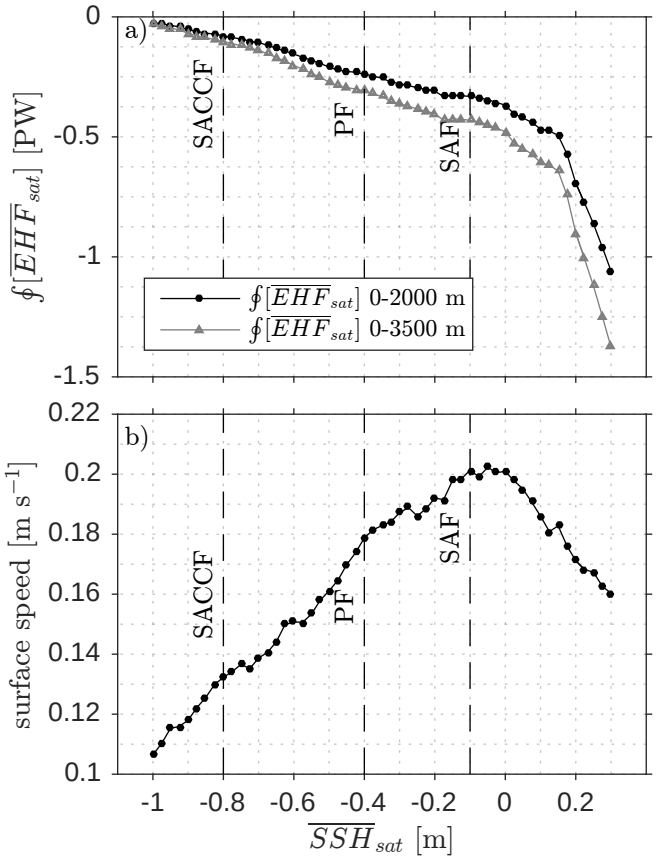

Figure 2.6. (a) $\oint[\overline{EHF}]_{sat}$ [PW] estimated from H^*_{sat} over the full-length (nearly 23.5 years) record of SSH_{sat} using the Southern Ocean power law in Equation 2.4 (black circles). The estimate is scaled up using the average ratio of surface-to-2000 m to surface-to-3500 m $[\overline{EHF}]_{cDrake}$ of 1.3 to a full-depth, i.e. surface to 3500 m, integration (gray triangles). (b) Mean surface geostrophic speed [m s^{-1}] along circumpolar $\overline{SSH}_{sat}$ contours. Nominal positions of the major fronts of the ACC are labelled.

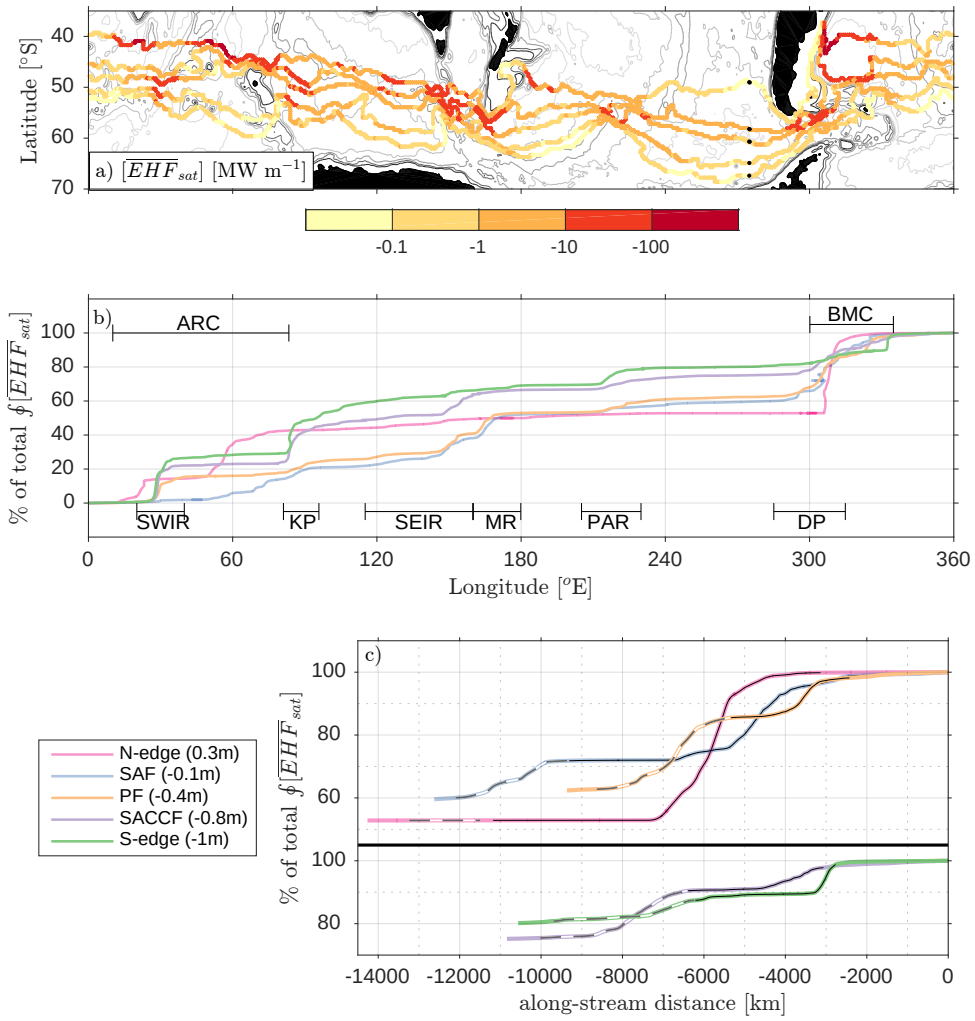

Figure 2.7. (a) $[\overline{EHF}]_{sat}$ [MW m^{-1}] along circumpolar streamlines. (b) Cumulative percent of total $\oint[\overline{EHF}]_{sat}$ along the five $\overline{SSH}_{sat}$ contours in panel (a) as a function of longitude. Longitudinal ranges of the eight $[\overline{EHF}]_{sat}$ hot spots are denoted by the horizontal bars and labelled. (c) An alternative view of the DP and BMC regions: cumulative percent of total $\oint[\overline{EHF}]_{sat}$ along the $\overline{SSH}_{sat}$ contours in panel (a), with the three northern streamlines in upper panel and the two southern streamlines in lower panel, as a function of along-stream distance east of 275°E (black dots in (a)), such that 0 km is 360°E. Within the colored lines, the DP region is designated by the thin white and gray dashed line and the BMC region is designated by the thin solid black line.

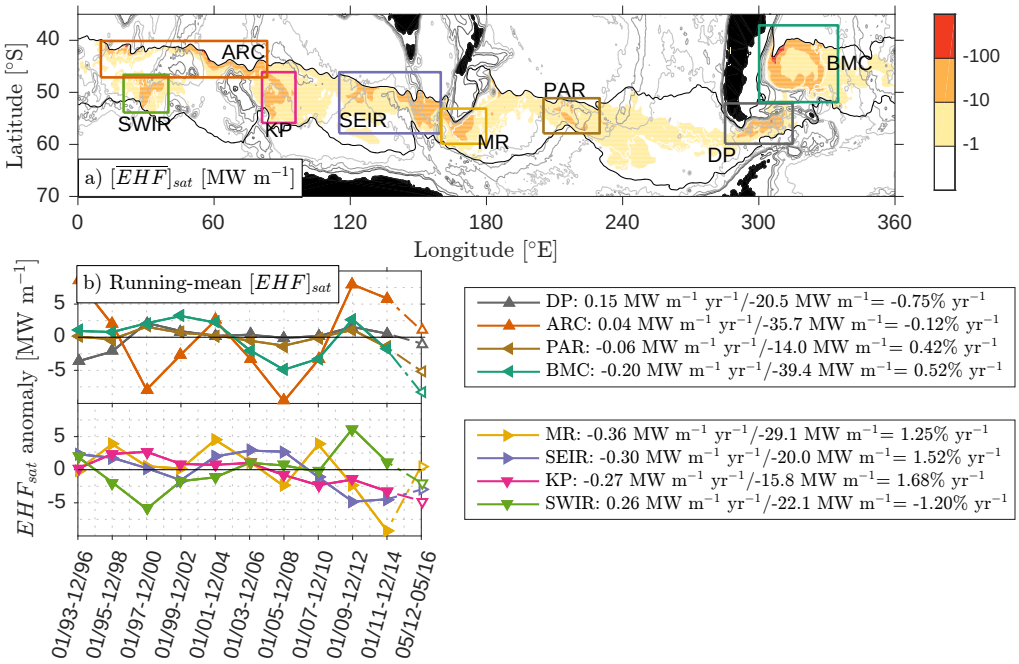

Figure 2.8. (a) Map of $[\overline{EHF}]_{sat}$ [MW m^{-1}]. The eight hot spots of $[\overline{EHF}]_{sat}$ are designated by the colored boxes and labelled. (b) Time series of running-mean $[EHF]_{sat}$ anomaly averaged over points within each box where $[\overline{EHF}]_{sat} \leq -10$ MW m^{-1}. Each colored line represents a particular $[\overline{EHF}]_{sat}$ hot spot and the colors are consistent with the colored boxes identifying the different regions in panel (a). The legends list the slope of the linear regression divided by the regional mean (using points where $[\overline{EHF}]_{sat} \leq -10$ MW m^{-1}) to express each as a percent per year for each hot spot. KP, SEIR, and BMC are the regions with statistically significant trends.

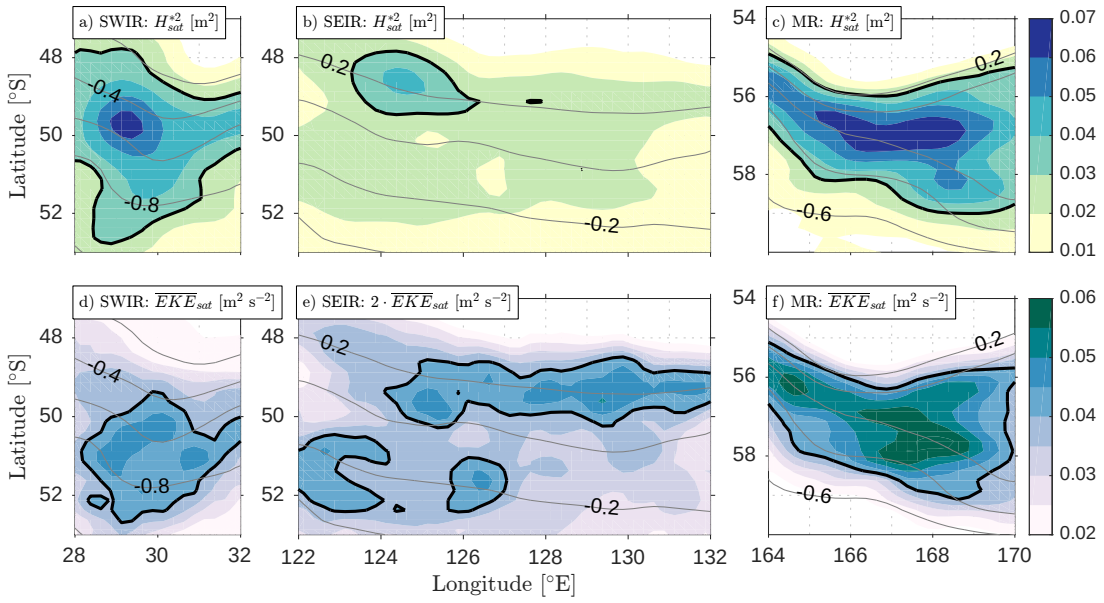

Figure 2.9. Observations of oceanic storm tracks highlighting the spatial offset between H^{*2}_{sat} [m^2] (a–c) and $\overline{EKE}_{sat}$ [m^2 s^{-2}] (d–f) in a subsection of three $[\overline{EHF}]_{sat}$ hotspots: Southwest Indian Ridge, Southeast Indian Ridge, and Macquarie Ridge (SWIR, SEIR, and MR). Note that H^{*2}_{sat} is presented here because it is more similar unit-wise to EPE than H^{*}_{sat}, and thus more analogous to $\overline{EKE}$. The contour interval for H^{*2}_{sat} is 0.01 m^2 and theH^{*2}_{sat} = 0.03 m^2 contour in black. The contour interval for $\overline{EKE}_{sat}$ is 0.005 m^2 s^{-1}, with $\overline{EKE}_{sat}$ = 0.04 m^2 s^{-2} in black. Note also that we present $2 \cdot \overline{EKE}_{sat}$ in the region within the SEIR (panel e), so that we can use consistent colorbar limits. Therefore, the black line represents $\overline{EKE}_{sat}$ = 0.02 m^2 s^{-2} in the SEIR region. The gray contour lines overlaid in each panel represent $\overline{SSH}_{sat}$ with a contour interval of 0.2 m and values are given by the numeric label.

MANUSCRIPT 3

Eddy-mean flow interactions in Drake Passage from a wave activity flux framework

by

Annie Foppert[1]

[1] *Graduate School of Oceanography, University of Rhode Island, Narragansett, RI*

In preparation for publication

3.1 Abstract

The dynamics of an oceanic storm track are investigated using four years of observations to evaluate the processes responsible for the offset between eddy heat flux and eddy kinetic energy (EKE) in Drake Passage. Mapped total geostrophic stream-function derived from current- and pressure-recording inverted echo sounder measurements are used to calculate the local wave activity flux, $\boldsymbol{W}$. This flux is used to diagnose the eddy-mean flow interactions in the eddy rich region of the Polar Frontal Zone, between the mean locations of the Polar Front and Subantarctic Front, immediately downstream of the Shackleton Fracture Zone. In the full four-year mean and in a composite-mean of eddy events, elevated values of the vertical component of $\boldsymbol{W}$ are collocated with elevated values of eddy potential energy (EPE) and are indicative of a conversion of mean available potential energy to EPE through baroclinic instability. Horizontal $\boldsymbol{W}$ vectors emanate from this region and generally point towards the region of elevated EKE found farther downstream. A case study of a single eddy event, from 15 to 23 July 2010, is presented and analyzed, highlighting the ability of $\boldsymbol{W}$ to diagnose the evolution of a storm track in a snap-shot sense. The importance of the horizontal $\boldsymbol{W}$ vectors transporting wave activity from the region of elevated $\boldsymbol{W}^z$ suggests the importance of barotropic processes in supporting strong EKE downstream from the jet's interaction with the Shackleton Fracture Zone where there is local production of EPE.

3.2 Introduction

The Southern Ocean and its dynamics are unique to the world's oceans, dominated by the zonally unbounded Antarctic Circumpolar Current (ACC) system. The deep-reaching stratification of the wind-driven ACC is thought to set the deep ($\geq$500 m) isopycnal structure of the world's oceans (e.g. *Toggweiler and Samuels*, 1995; *Nikurashin and Vallis*, 2012). Quantifying the strongly inhomogenous flow of the ACC, with along- and across-stream variability on many scales, is an observational challenge and numerical models require parameterization of processes crucial for setting the stratification of the ACC, i.e. eddy transports (of buoyancy, heat, momentum, carbon) and eddy-mean flow interactions. Predicting and preparing for future climates rely on properly parameterizing these processes in climate models that require validation with direct observations.

The large-scale dynamics of the ACC are analogous to those of the midlatitude atmosphere, with storm tracks of increased eddy activity downstream of localized forcing (e.g. *Williams et al.*, 2007; *Bischoff and Thompson*, 2014; *Chapman et al.*, 2015). In the ACC, the forcing is orographic, due to the mean flow's encounter with large bathymetric features. The existence of these oceanic storm tracks makes it especially challenging to extrapolate local observations to the rest of the ACC and to interpret the results of studies framed in a zonal-mean sense at any particular location in the ACC. Work on the dynamics of atmospheric storm tracks (e.g. *Danielson et al.*, 2006), that have been studied for much longer than oceanic storm tracks, guides our study of the dynamics of an oceanic storm track in Drake Passage.

The dynamics of a localized storm track, be it atmospheric or oceanic, are rooted in the interaction between the eddying and the mean flow. That is, the storm track is defined as a region of relatively high eddy activity (often diagnosed

through eddy kinetic energy, EKE) where the eddies are growing by gaining energy from the mean flow. In the ACC, episodic baroclinic instability events are the main mechanism for eddy heat flux (*Watts et al.*, 2016). Each baroclinic instability event is associated with a conversion from mean available potential energy (APE) to eddy potential energy (EPE) through a flux of heat/buoyancy across the mean upper baroclinic front by the eddying flow (*Pedlosky*, 1987). This step is followed by a conversion of EPE to EKE through vertical eddy buoyancy flux. EKE can also be produced directly from the mean kinetic energy pool through barotropic instability. A recent idealized model study, with dynamics representative of a standing meander in the ACC associated with a submarine ridge, illustrates the importance of mixed baroclinic-barotropic instability (*Youngs et al.*, 2017).

Elevated EKE values observed in the atmosphere downstream of the local forcing and region of highest baroclinicity have been explained, through use of numerical model simulations, by the idea of 'downstream baroclinic development' (*Orlanski and Sheldon*, 1993). Downstream baroclinic development has been observed in the atmosphere to be associated with large storms, e.g. a major winter blizzard (*Danielson et al.*, 2006). In this process, an individual eddy depends on its neighboring upstream eddy for its energy through geopotential flux convergence (*Orlanski and Katzfey*, 1991; *Orlanski and Sheldon*, 1993). This transfer of energy allows the wave packet to move much faster than the individual eddies propagate. This process of sequential growth and decay of eddies downstream of the local forcing is a purely baroclinic process and there is no contribution from the barotropic component of the flow. The importance of the barotropic flow in the ACC suggests that downstream baroclinic development may not fully explain the dynamics of oceanic storm tracks.

Eddy energy budgets, based on time-mean eddy energy equations, are typ-

ically used to study eddy-mean flow interactions in the ocean and can provide useful information when interpreted appropriately (e.g. *Cronin*, 1996; *Phillips and Rintoul*, 2000; *Bishop et al.*, 2013). However, without knowledge of the physical process responsible for the different conversion terms, the interpretation of these eddy energy budgets is ambiguous (*Plumb*, 1983). These ambiguities can be avoided by diagnosing a 'wave activity flux.' *Eliassen and Palm* (1961) first formulated a wave activity flux for a zonally and temporally averaged mean flow, with eddies defined as any deviation from that mean. The EP flux, as it has come to be known, provides useful insight into the relative importance of eddy heat and momentum fluxes, i.e. of baroclinic and barotropic instabilities. While the EP flux, and the transformed Eulerian mean framework that often accompanies it, is a powerful tool for diagnosing eddy-mean flow interactions, the requisite zonally and temporally averaged background state makes it a difficult diagnostic to observe and makes interpretation a challenge in the ACC.

Plumb (1985) generalized the wave activity flux to three dimensions for a simple time-mean flow, eliminating the need for a zonally averaged background state. *Takaya and Nakamura* (2001) further generalize wave activity flux to include the temporal dimension, i.e. the propagating component of the eddy is also included whereas the flux of *Plumb* (1985) is for a stationary eddy. Therefore, the study of the interaction between propagating waves in three dimensions and the background mean flow is possible under the assumptions of their formulation (explicitly stated in Section 2). An export of wave activity, i.e. a divergence of its flux, is analogous to the mean flow losing energy to the eddying flow. Additionally, the vertical wave activity flux vector can be thought to be associated with baroclinic interactions and the horizontal flux vectors with barotropic interactions (*Takaya and Nakamura*, 2001).

In this study, eddy-mean flow interactions in Drake Passage are diagnosed through wave activity flux along with eddy energy. Specifically, these diagnostics are used to shed light on the physical processes responsible for the spatial offset observed between eddy heat flux and EKE in Drake Passage (*Foppert et al.*, in rev). In the next section, an oceanic wave activity flux based on that of *Takaya and Nakamura* (2001) is presented. Section 3 describes the Drake Passage dataset and the complementary satellite altimetry data used in this study. Section 4 presents our major results: four-year time-mean fields of wave activity flux and its components, and a case study highlighting the temporal evolution of an eddy event that went into making composite-mean fields. Section 5 discusses the results and Section 6 summarizes the study.

3.3 A primer on wave activity and its flux

For small amplitude, quasi-geostrophic disturbances on a background mean geostrophic flow, a linear combination of the eddy energy (EPE and EKE) and eddy enstrophy can be formulated such that

$$\frac{\partial M}{\partial t} + \nabla \cdot \boldsymbol{W} = D, \tag{3.1}$$

where M is the wave activity density, $\boldsymbol{W}$ is the wave activity flux, and D is diabatic or frictional forcing (*Takaya and Nakamura*, 2001). The wave activity $M = \rho(A + E)/2$, where $A = (1/2)q'q'/|\nabla\bar{q}|$ is the psuedomomentum with q being the quasi-geostrophic potential vorticity and an over-bar denoting the time-mean quantity and $E = e/(|\bar{\mathbf{u}}| - c_p)$ is a normalized eddy energy density with c_p being the phase speed of the eddies that must be known a priori. Quasi-geostrophic potential vorticity anomaly, $q' = \nabla^2\psi' + (f_0^2\psi_z/N^2)_z$, has units of s^{-1} and the eddy energy, $e = \psi'_{xx} + \psi'_{yy} + (f_0\psi_z/N)^2$, has units of $\mathrm{m}^2\ \mathrm{s}^{-2}$. Here, ψ is the total geostrophic stream-function with its associated geostrophic velocity, $\boldsymbol{u} = (u, v) = (-\psi_y, \psi_x)$, and buoyancy, $b = f_0\psi_z$, f_0 in the local Coriolis parameter, $N^2 = \bar{b}_z$ is the squared

buoyancy frequency, and subscripts represent partial derivatives.

Written this way, the wave activity and its flux have no phase dependence, i.e. do not depend on their location along the linear wave. The derivation of this wave activity and its flux by *Takaya and Nakamura* (2001) assumes that (1) the steady basic flow is nearly unforced, (2) the wave/eddy is slowly changing in a WKB sense, and (3) the phase speed of the eddies is almost constant in the direction of the background mean flow. These assumptions impose strict restrictions that may not hold true in the ACC, yet the following results and their interpretations are useful in understanding eddy-mean flow interactions in Drake Passage.

Equation 3.1 states that, in the absence of diabatic forcing and friction, a convergence of the wave activity flux, $\boldsymbol{W}$, is directly associated with an increase in local wave activity, M. *Takaya and Nakamura* (2001) show in the atmosphere that $\boldsymbol{W}$ is divergent over a region of surface heat fluxes or thermal forcing and, in another case, convergent into an amplifying blocking high. Furthermore, *Takaya and Nakamura* (2001) show that $\boldsymbol{W}$ illustrates wave propagation and is, in general, perpendicular to height anomaly contours. Moreover, Equation 3.1 implies that $\boldsymbol{W}$ is non-divergent for steady, conservative waves and that the divergence of the time-mean $\boldsymbol{W}$ is directly related to nonconservative or nonlinear effects.

The wave activity flux vector is the sum of a stationary and propagating component, i.e. $\boldsymbol{W} = \boldsymbol{W}_s + M\bar{\boldsymbol{C}}_{\boldsymbol{u}}$, where $\bar{\boldsymbol{C}}_u$ is the mean phase speed of the eddies in the direction of the mean flow. For a completely stationary eddy, the second term is exactly zero. The stationary component of the wave activity flux vector for the ocean in depth coordinates can be written as

$$\boldsymbol{W_s} = \frac{\rho}{2|\bar{\boldsymbol{u}}|}\{ \begin{array}{c} \bar{u}(\psi_x'^2 - \psi'\psi'_{xx}) + \bar{v}(\psi'_x\psi'_y - \psi'\psi'_{xy}) \\ \bar{u}(\psi'_x\psi'_y - \psi'\psi'_{xy}) + \bar{v}(\psi_y'^2 - \psi'\psi'_{yy}) \\ \frac{f_0^2}{N^2}[\bar{u}(\psi'_x\psi'_z - \psi'\psi'_{xz}) + \bar{v}(\psi'_y\psi'_z - \psi'\psi'_{yz})] \end{array} \}, \tag{3.2}$$

where ρ is a nominal ocean density. Note that the vertical flux is scaled by f_0^2/N^2.

Takaya and Nakamura (2001) explain that the terms of $\boldsymbol{W_s}$ represent two complementary dynamical processes. The first terms in Equation 3.2, e.g. the terms with $\bar{u}\psi_x'^2$ and $\bar{v}\psi_y'\psi_x'$ in the zonal component of $\boldsymbol{W}_s$, are associated with 'backward transport' of mean westerly momentum due to horizontal flux of eddy momentum and heat. (Recall that horizontal heat flux is equivalent to a vertical momentum flux in a quasi-geostrophic framework.) The second terms in Equation 3.2, e.g. the terms with $\bar{u}\psi'\psi_{xx}'$ and $\bar{v}\psi'\psi_{xy}'$ in the zonal component of $\boldsymbol{W}_s$, are associated with work done by pressure fluctuations (i.e. ψ'). *Takaya and Nakamura* (2001) show that these second terms can be approximately interpreted as a flux of geopotential anomaly by the ageostrophic (sub- or super-geostrophic) flow. For a linear plane wave, *Takaya and Nakamura* (2001) showed that the first terms dominate between the trough and ridge ($\psi' = 0$) while the second terms dominate at the trough/ridges where the ageostrophic flow is strongest, and the two sets of terms combine into a phase-independent quantity. A detailed description of the relation between terms of $\boldsymbol{W}_s$ and traditional eddy energy equation terms can be found in *Chapman et al.* (2015, Section 3). For a description of the physical interpretation of the wave activity flux terms, the reader is referred to *Takaya and Nakamura* (2001, Section 4) or *Chapman et al.* (2015, Section 3c)

3.4 Data

3.4.1 cDrake dataset

The cDrake project was designed to study the dynamics and transport of the ACC in Drake Passage with observations from November 2007 through November 2011 (www.cdrake.org; *Chereskin et al.*, 2012). A local dynamics array (LDA) and a cross-passage transport line of bottom-moored current- and pressure-recording inverted echo sounders (CPIES) was deployed with 40 km spacing between each instrument (Figure 3.1). The LDA was placed in the inter-frontal zone between the

Polar and Subantarctic Fronts downstream of the Shackleton Fracture Zone (SFZ), in a region of elevated eddy activity (*Firing et al.*, 2014). Each CPIES records hourly round-trip acoustic travel time (τ), bottom pressure and temperature, and near-bottom reference velocity measured outside the bottom boundary layer at 50 m above the seafloor. Four-year time series of each quantity are three-day low-pass filtered and subsequently resampled twice a day. More details on the data collection and processing can be found in *Tracey et al.* (2013).

A gravest empirical mode analysis based on regional hydrography provides a profile of temperature and salinity, and thus geopotential height (ϕ), for every value of τ (*Chidichimo et al.*, 2014). Buoyancy is then calculated from each temperature and salinity profile. That is, $b = \frac{g}{\rho_0}(\gamma - \gamma_0)$, where $g = 9.8$ m s^{-2} is a local gravitational acceleration, $\rho_0 = 1035$ kg m^{-3} is a standard ocean density, $\gamma_0 = 28.5$ kg m^{-3} is a deep neutral density, and γ is calculated with the neutral density package of *Jackett and McDougall* (1997). *Firing et al.* (2014) demonstrate that the LDA allows for optimal-interpolation mapping of the total geostrophic stream-function, ψ, its horizontal derivatives (i.e. total geostrophic velocity), and horizontal velocity shear. A detailed error analysis is also detailed in *Firing et al.* (2014).

The stationary component of the wave activity flux, $\boldsymbol{W}_s$ is calculated from the mapped $\psi(x, yz, t)$ fields, as in Equation 3.2. The propagating component of $\boldsymbol{W}$ is assumed to be small compared with the stationary component, and only consider the stationary component of the wave activity flux. Therefore, the subscript from $\boldsymbol{W}_s$ is dropped and the stationary component of the wave activity flux is referred to as $\boldsymbol{W}$ hereafter. This assumption of the stationary flux dominating the propagating flux is consistent with the work of *Chapman et al.* (2015). Here, 'time-mean' is defined as the 90-day low-pass filtered field and the anomalies are any deviation

from the slowly varying mean.

Eddy energy, EPE and EKE, are calculated directly from the CPIES measurements. EPE is calculated from the buoyancy field as

$$EPE = \frac{1}{2}(\frac{b'^2}{N^2}), \tag{3.3}$$

where $N^2 = \bar{b}_z$ is the low-passed mean buoyancy frequency squared. EKE is calculated from the total geostrophic velocity as

$$EKE = \frac{1}{2}(u'^2 + v'^2). \tag{3.4}$$

Again, as with $\boldsymbol{W}$, the prime denotes any deviation from the slowly varying, 90-day low-passed 'mean' quantity.

3.4.2 Satellite altimetry

The analysis is complemented with satellite altimetry to give a broader picture of the regional sea surface height, SSH, that is the addition of the CNES-CLS13 mean dynamic topography to the Ssalto/Duacs gridded daily mean sea level anomaly with a consistent reference period from 1993 to 2012. The mean dynamic topography was produced by CLS Space Oceanography Division and the sea level anomalies by the Copernicus Marine and Environment Monitoring Service; both are available online through AVISO at http://www.aviso.altimetry.fr. Both products are mapped onto 1/4° horizontal resolution grid. Only SSH data coinciding with the cDrake experiment, from November 2007 to November 2011, is used in this study.

3.5 Results

3.5.1 Four-year mean fields

The four-year mean stationary wave activity flux, $\overline{\boldsymbol{W}}$, averaged from 200 to 700 meters depth is shown in Figure 3.2. The vertical component $\overline{\boldsymbol{W}}^z$ is positive (or very weakly negative) over the entire LDA. The largest values of $\overline{\boldsymbol{W}}^z$ are found

immediately downstream of the SFZ, with peak values of almost 0.4 J m^{-3} near 64.5°W and 57.5°S. This peak in $\overline{\boldsymbol{W}}^z$ is collocated with a mean (SAF) crest, as seen in the mean SSH field (Figure 3.2). There is another local peak in $\overline{\boldsymbol{W}}^z$ in the central LDA (near 63°W) of about half the magnitude of the western peak. The large positive values of $\overline{\boldsymbol{W}}^z$ are indicative of downgradient eddy heat flux, or downward vertical flux of westward momentum, associated with baroclinic growth and instability.

The horizontal component $\overline{\boldsymbol{W}}^H$ illustrates the horizontal propagation of the wave activity and is generally perpendicular to the ψ' field (not shown). In the western part of the LDA, $\overline{\boldsymbol{W}}^H$ points east or northeast, i.e. the standing meander at the SFZ is emitting mean wave activity northeast and out of the LDA. In the central and eastern LDA, $\overline{\boldsymbol{W}}^H$ vectors show some rotational aspects (Figure 3.2). The rotational $\overline{\boldsymbol{W}}^H$ in the eastern LDA appear collocated with a closed contour in the mean SSH field.

The four-year mean $\overline{EKE}$ and $\overline{EPE}$ are plotted in Figure 3.3. The $\overline{EKE}$ field has two peaks, both located adjacent to $\overline{\boldsymbol{W}}^z$ peaks. The $\overline{EPE}$ field shows elevated values in the northwest corner of the LDA, north of the main $\overline{\boldsymbol{W}}^z$ peak. The maximum value of $\overline{EPE}$ (0.047 m^2 s^{-2}) is slightly larger than that of $\overline{EKE}$ (0.036 m^2 s^{-2}). Yet the average ratio of $\overline{EPE}/\overline{EKE}$ is about unity over the LDA, with $\overline{EPE}$ dominating in the northwest corner and $\overline{EKE}$ dominating over the rest of the LDA, i.e. east of 64.5°W. The mean enstrophy field (not shown) broadly mirrors the $\overline{EPE}$ field, not a surprising result given that potential vorticity is dominated by the thickness term in this region.

The downstream evolution of $\overline{\boldsymbol{W}}$, $\overline{EPE}$, and $\overline{EKE}$ along the main storm track in the western part of the LDA is shown in Figure 3.4. The quantities are averaged in four sectors along the western storm track, i.e. four sectors starting

from the $\overline{\boldsymbol{W}}^z$ peak in the southwest corner and heading in the direction of the mean $\overline{\boldsymbol{W}}^H$ vectors. As expected, $\overline{\boldsymbol{W}}^z$ is strongest in the two upstream sectors, and then decreases in amplitude in the subsequent two sectors to about half its original magnitude by the northeastern-most sector. The magnitude of $\overline{\boldsymbol{W}}^H$ has its maximum value in the upstream region and reaches a minimum in the middle of the track (Figure 3.4, Sector 3). The $\overline{EPE}$ mirrors the $\overline{\boldsymbol{W}}^z$ with the highest values found in the upstream sector and decreasing farther downstream. In contrast, the weakest $\overline{EKE}$ is found in the upstream sector, and it increases to its largest values in the middle sections. The strongest $\overline{EKE}$ is collocated with a weakest $\overline{\boldsymbol{W}}^H$, i.e. with a convergence of $\overline{\boldsymbol{W}}^H$ in the along-track direction.

3.5.2 Composite-mean fields

As the LDA is located in a region between the SAF and PF, the left column of Figure 3.5 presents composites of the same information as in Figures 3.2 and 3.3 for time periods of elevated $\boldsymbol{W}^z$ (≥ 0.5 J m^{-3}) in the western LDA. Additionally, the divergence of the horizontal wave activity flux, $\nabla \cdot \boldsymbol{W}^H$ is plotted in Figure 3.5j. About 20% of the four years of data, 297 days, were used in creating the composites shown here. This removes some of the 'noise' in the full four-year mean fields, and more clearly illustrates the wave activity flux pattern in Drake Passage.

The pattern of $\boldsymbol{W}^z$ is similar to before, with a large peak in the western LDA, but the smaller local maximum more centrally located is eliminated (Figure 3.5a). The magnitude of the large western peak in $\boldsymbol{W}^z$ is about four times as large as that in the full four-year mean field. Similarly, the largest values of EKE and EPE are larger than their full four-year mean counterparts by a factor of 1.5 and 2, respectively (Figure 3.5d,g). $\boldsymbol{W}^H$ vectors are again pointing northeast, now with a slightly more northern component than the four-year mean vectors. The composite-mean EPE and $\boldsymbol{W}^z$ fields are well correlated in space (R^2=0.74), with

elevated values in the western part of the LDA. Again, the peaks in $\boldsymbol{W}^z$ and EKE are adjacent to each other, with the $\boldsymbol{W}^H$ vectors pointing from elevated $\boldsymbol{W}^z$ to elevated EKE. Broadly speaking, the peak in EKE is collocated with a convergence of $\boldsymbol{W}^H$ (Figure 3.5d,j), but this result is not statistically significant.

These composite-mean fields can be further decomposed into times when a (PF) trough and times when a (SAF) crest intruded in western LDA (Figure 3.5, middle and right column, respectively). While the overall patterns of $\boldsymbol{W}$ and EPE are quite similar for SAF and PF events - elevated values of $\boldsymbol{W}^z$ and EPE in the western LDA and $\boldsymbol{W}^H$ vectors pointing north-northeast - there are some slight differences. In particular, the maximum EPE and EKE for PF trough events ($\psi' > 0$) is stronger by 0.02 $\mathrm{m}^2\ \mathrm{s}^{-2}$ and 0.01 $\mathrm{m}^2\ \mathrm{s}^{-2}$, respectively, than that for SAF crest events ($\psi' < 0$). Additionally, the location of the EPE peak is farther north for PF events than it is for SAF events (Figure 3.5b,c,e,f).

The EKE and horizontal divergence ($\nabla \cdot \boldsymbol{W}^H$) fields show more spatial variability between the two subsets within the composites (Figure 3.5h,i,k,l). The peak in EKE is larger for PF trough events than SAF crest events and offset slightly south of the strongest $\boldsymbol{W}^H$ vectors. In the composite of SAF crest events, the $\boldsymbol{W}^H$ vectors point more directly from the peak in EPE, or $\boldsymbol{W}^z$, towards the peak of EKE (Figure 3.5i). The horizontal divergence of $\boldsymbol{W}^H$ is weaker and located farther north for PF trough events than SAF crest events.

3.5.3 Case study: 15-23 July 2010

Figure 3.6 illustrates the temporal evolution of a PF trough event included in the composite-mean fields presented in the previous section. The daily SSH of a nominal PF (-0.3 m) is contoured in each panel, and its trough is seen in the very southwestern edge of the LDA in the beginning of the event. During this event, shown here from 15 to 23 July 2010, a positive ψ anomaly is present in the western

part of the LDA, with an adjacent negative ψ anomaly more centrally located, and a smaller positive ψ anomaly in the east (Figure 3.6). This train of ψ anomalies is associated with a large meander that is also seen in the SSH field (recall that the SSH has not been low-pass filtered and an exact correspondence between SSH and ψ is not expected).

During this time period, *Watts et al.* (2016) (Figure 7) documented a strong poleward eddy heat flux in the western part of the LDA and a slightly weaker flux in the central LDA. In particular, those authors find joint upper-deep intensification associated with increasing eddy heat flux between 16 and 19 July, before the features translate out of the LDA and the flux decreases by 25 July. Here, Figure 3.6 (top row) shows a simultaneous intensification of $\boldsymbol{W}^z$ from 15 to 19 July and a subsequent decrease in $\boldsymbol{W}^z$ from 21 to 23 July, with its maximum value realized on 20 July. The vertical $\boldsymbol{W}^z$ is offset slightly east from the western EPE peak (Figure 3.6, second row). In this case, the vertical $\boldsymbol{W}^z$ peaks tends to fall between the western EPE peak and the EKE peak (Figure 3.6, third row).

Strong $\boldsymbol{W}^H$ vectors are collocated with the $\boldsymbol{W}^z$ peak and point north-northeast across the ψ' contours from the western anomaly to the central anomaly (Figure 3.6). Comparison of the ψ' fields on 15 and 23 July shows that the large positive ψ anomaly has translated in the same direction. On 17 and 19 July, there is a convergence of $\boldsymbol{W}^H$ that aligns well with the EKE peak. On 21 July, the vectors turn more eastward and converge into the center of the central ψ anomaly.

3.6 Discussion

3.6.1 4-year and composite-mean fields

Wave activity flux, $\boldsymbol{W}$, is a powerful diagnostic for examining the evolution of wave activity (a combination of total eddy energy and eddy enstrophy). In this framework, in the absence of adiabatic forcing or friction, a convergence of $\boldsymbol{W}$ is

directly linked to an increase in wave activity (Equation 3.1) and the growth of an eddy. Here, the stationary component of $\boldsymbol{W}$ is calculated with observations of the total geostrophic stream-function in the eddy-rich Polar Frontal Zone in Drake Passage. The array of CPIES was deployed immediately downstream of the Shackleton Fracture Zone, a major submarine ridge (Figure 3.1).

In order to conserve potential vorticity, the jets of the ACC shift equatorward as they flow over the Shackleton Fracture Zone and poleward as they flow down the leeward side, mechanically forcing a stationary meander in the lee of the ridge. Episodic events of SAF crests and PF troughs intruding into the western LDA are observed to be associated with strong eddy heat flux and baroclinic instability events (*Watts et al.*, 2016). The four-year mean $\boldsymbol{W}$ field, averaged between 200 and 700 m depth, shows elevated values of the vertical $\overline{\boldsymbol{W}^z}$ and $\overline{EPE}$ in the western part of the LDA (Figure 3.2 and 3.3a). This is indicative of the conversion from mean APE to EPE associated with baroclinic instability.

Horizontal $\overline{\boldsymbol{W}^H}$ vectors emanate from this region, indicating that wave activity is being transported from the region of strongest $\overline{\boldsymbol{W}^z}$ (and eddy heat flux) northeast and out of the LDA. This is considered the main storm track in this region, such that the track trends northeast, almost perpendicular to the mean SAF crest seen in Figure 3.1. In an along-track sense, i.e. averaging over the region of elevated $\overline{\boldsymbol{W}^z}$ in sequential bins in the direction of the $\overline{\boldsymbol{W}^H}$ vectors, the largest values of $\overline{EKE}$ are found downstream of the largest $\overline{\boldsymbol{W}^z}$ and $\overline{EPE}$ (Figure 3.4). This is also where there is an along-track convergence of $\overline{\boldsymbol{W}^H}$.

There is also a secondary region of elevated $\boldsymbol{W}^z$ located in the central LDA between the mean SAF crest and mean ring (closed mean SSH contour; Figure 3.2). Occasional intrusions of a PF trough and ring formation events have been observed in this region (*Chereskin et al.*, 2009). The horizontal $\boldsymbol{W}^H$ vectors show cyclonic

(clockwise) rotation that may be associated with this mean ring or with the deep recirculation in the Yaghan Basin, a deep basin in northern Drake Passage centered near 56°S and 61°W. There is also a secondary peak in $\overline{EKE}$, again connected to the secondary $\overline{\boldsymbol{W}^z}$ peak by $\overline{\boldsymbol{W}^H}$ vectors (Figure 3.2 and 3.3). Here, the focus is on the dynamics of the western storm track, but it can be noted that a larger array in the future could help illuminate the complicated dynamics in this region. In particular, it would help parse out whether the storm tracks continue farther downstream (outside of the array) or if they are disrupted by bathymetry and dissipate locally.

To highlight the dynamics of the western storm track, a composite-mean look at the $\boldsymbol{W}$ and eddy energy fields for a subset of eddy events is presented (Figure 3.5). An eddy event is defined as time when the regional-mean $\boldsymbol{W}^z$ (west of 64°W) is greater than 0.5 J m^{-3}. While the pattern in the western LDA doesn't change significantly, the secondary peak in $\boldsymbol{W}^z$ is greatly reduced in magnitude relative to the primary peak immediately downstream of the Shackleton Fracture Zone. Again, the horizontal $\boldsymbol{W}^H$ vectors point from the region of elevated EPE and $\boldsymbol{W}^z$ towards the region of highest EKE. This is especially apparent for events involving a SAF crest ($\psi' < 0$; Figure 3.5, right column). In a broad sense, where the strongest values of EKE are found, there is also a convergence of $\boldsymbol{W}^H$ (Figure 3.5, bottom row). The association between the location of EKE peaks and the horizontal component of the wave activity flux (and/or its convergence) illustrates the importance of barotropic processes in the transport of wave activity and the production of EKE downstream from regions of highest baroclinicity.

3.6.2 Case study: 15-23 July 2010

The temporal evolution of a 'typical' meander event is shown in Figure 3.6. During this time period, a PF trough ($\psi' > 0$) is intruding into the western side

of the LDA, strengthens, and begins to decay. Throughout the eight-day event, strong horizontal $\boldsymbol{W}^H$ vectors emanate from the $\boldsymbol{W}^z$ peak and generally point north-northeast from the western to the central ψ anomaly. *Watts et al.* (2016) show strong eddy heat flux in the western and central LDA during the first several days, with increasing flux from 16 to 19 July followed by decreasing flux from 22 to 25 July. Here, the largest $\boldsymbol{W}^z$ values are found on 20 July. The strong $\boldsymbol{W}^z$ and eddy heat flux, cited in *Watts et al.* (2016), are indicative of baroclinic growth and instability through a conversion from mean APE to EPE.

The offset between $\boldsymbol{W}^z$ and EKE and the alignment of $\boldsymbol{W}^z$ and EPE are not as pronounced in this event as they are in the four-year mean or composite-mean fields (Figure 3.4 and 3.5). In fact, the $\boldsymbol{W}^z$ peaks appear located between the EKE and EPE peaks, with the strongest EKE consistently found on the leading edge of the western ψ anomaly and EPE peaks found in the center of the western and central anomalies (Figure 3.6). It can be noted again here that the wave activity, M, is a combination of eddy energy and enstrophy and that the eddy enstrophy broadly mirrors the EPE field as potential vorticity is dominated by the thickness term (not shown).

In simple baroclinic instability, mean APE is converted to EPE through a horizontal eddy heat flux and EPE is converted to EKE through vertical eddy heat flux. Here, it is seen that the largest value of EPE is found on 23 July in the western ψ anomaly, while the largest value of EKE is found on 17 July. The enhanced EKE on 17 July, prior to the strongest $\boldsymbol{W}^z$ and horizontal eddy heat flux (from *Watts et al.* (2016), Figure 7), implies that the EKE is being produced by a process other than baroclinic instability, i.e. barotropic instability, or that there is eddy heat flux and baroclinic growth occurring outside the LDA and the energy is being transported into the LDA. In fact, Figure 3.6 (third row) shows

strong horizontal $\boldsymbol{W}^H$ vectors in the southwest corner of the LDA on 15 and 17 July that show a flux of wave activity into the LDA.

Later in the event, as $\boldsymbol{W}^z$ is at its strongest between 19 and 21 July, $\boldsymbol{W}^H$ vectors point from the $\boldsymbol{W}^z$ peak to the EKE peak. On 19 July, there is horizontal convergence of $\boldsymbol{W}^H$ at the EKE peak, but on 21 July the convergence is farther downstream (in the center of the negative ψ anomaly). There is also some divergence of $\boldsymbol{W}^H$ out of the western ψ anomaly on 23 July, which suggests the mean flow taking wave activity back from the eddies (or localized diabatic forcing). Overall, the energetics of the storm track are strongly tied to both the horizontal and vertical components of $\boldsymbol{W}$, highlighting the importance of barotropic and baroclinic processes, respectively, transferring wave activity through an oceanic storm track. Additionally, by diagnosing the dynamics of the storm track using $\boldsymbol{W}$, the evolution of the eddy-mean flow interactions can be studied in a snap-shot sense.

3.6.3 Implications of this work

Orlanski and Sheldon (1995) describe three stages of downstream baroclinic development. At first, energy from a pre-existing mature eddy is carried downstream (by geopotential fluxes by the ageostrophic flow) to feed an adjacent eddy. As the initial eddy decays and this downstream eddy matures, energy from it is carried farther downstream to feed a third eddy. As the second begins to decay, the third eddy matures, and so on until the energy eventually dissipates. In the situation described by *Orlanski and Sheldon* (1995), the wave is purely baroclinic, i.e. there is no barotropic mode, and dissipation occurs far downstream. In the ACC, both barotropic and baroclinic modes exist together. Additionally, unlike the atmosphere or many modeling studies with a single idealized ridge (e.g. *Chapman et al.*, 2015; *Bischoff and Thompson*, 2014; *Youngs et al.*, 2017), the ACC

is often punctuated by bathymetry. That is, soon after its interaction with the Shackleton Fracture Zone, the PF must navigate the Scotia Arc and the SAF is steered strongly northward by the South American continental slope. Upstream of the Shackleton Fracture Zone, the ACC also encounters the Phoenix Ridge near 66°W.

Here, it appears that barotropic processes, diagnosed as $\boldsymbol{W}^H$ and suggested by its convergence, are important in the maintaining the offset between EPE (produced through horizontal eddy buoyancy flux in the region of high baroclinicity and observed through $\boldsymbol{W}^z$) and EKE. Moreover, *Youngs et al.* (2017), using an idealized numerical simulation of flow over a ridge, show that mixed barotropic-baroclinic instability is important for the dynamics of Southern Ocean storm tracks. In the conventional eddy energy budgets, EKE is produced in two ways: through the baroclinic pathway by vertical eddy buoyancy flux that converts EPE to EKE or through the barotropic pathway by horizontal eddy momentum flux that converts mean kinetic energy to EKE. It remains unclear here which of these two processes is responsible for the EKE in Drake Passage or what the relative contribution of each process is to the total production of EKE. In order to properly parameterize global circulation and climate models to accurately simulate the transfers of energy and enstrophy, i.e. wave activity, through the ACC system, all the processes responsible for those transfers must first be understood.

3.7 Conclusion

In this study, stationary wave activity flux ($\boldsymbol{W}$) and eddy energy (EKE and EPE) are presented in the eddy-rich inter-frontal zone between the SAF and PF in Drake Passage. These quantities are calculated from direct observations by CPIES during the four years of the cDrake experiment, from November 2007 through November 2011. These quantities are presented in three ways: four-year time

mean, composite-mean of eddy events that make up 20% of the four-year time series, and a case study of one eddy event, a PF trough in the western LDA, that went into the composites. The patterns of $\boldsymbol{W}$ and EKE and EPE aide understanding of the observed spatial offset between the regions of strongest eddy heat flux ($\boldsymbol{W}^z$) and EKE: horizontal $\boldsymbol{W}^H$ transports wave activity from the region of growth and EPE production into the region of highest EKE.

The vertical wave activity flux, $\boldsymbol{W}^z$, is elevated in the western part of the LDA, immediately downstream of the Shackleton Fracture Zone, where a standing meander (SAF crest) can be seen in the satellite SSH data (Figure 3.2). This hot spot of $\boldsymbol{W}^z$ is heightened in a composite-mean of eddy events, both PF troughs and SAF crests (Figure 3.5, top row). In the composites, the elevated $\boldsymbol{W}^z$ is generally collocated with elevated values of mean EPE and is indicative of baroclinic instability and the conversion of mean APE to EPE. Horizontal $\boldsymbol{W}^H$ vectors point from the region of elevated $\boldsymbol{W}^z$ and EPE towards the region of elevated EKE (Figure 3.5). That is, the increased wave activity due to baroclinic growth immediately downstream of the Shackleton Fracture Zone is transported out of the region by $\boldsymbol{W}^H$ that feeds the adjacent elevated EKE values. Whether the EKE is produced from the EPE through the baroclinic pathway or the EKE is produced directly through the barotropic pathway is still unclear. However, the importance of $\boldsymbol{W}^H$ in controlling the elevated EKE adjacent to the region of baroclinic growth, and the suggestion of horizontal $\boldsymbol{W}^H$ convergence associated with increased EKE, highlights the importance of barotropic processes in maintaining the structure of oceanic storm tracks.

Acknowledgements The author is grateful for support from the National Science Foundation grants OCE1141802. The cDrake data are available at the National Centers for Environmental Information, online at http://www.nodc.noaa.gov. She thanks Kathy Donohue, Randy Watts, and Karen Tracey for the helpful discussions and guidance.

Bibliography

Bischoff, T., and A. F. Thompson (2014), Configuration of a Southern Ocean storm track, *Journal of Physical Oceanography*, *44*(12), 3072–3078, doi:10.1175/JPO-D-14-0062.1.

Bishop, S. P., D. R. Watts, and K. A. Donohue (2013), Divergent eddy heat fluxes in the Kuroshio Extension at 144 - 146E. Part I: Mean structure, *Journal of Physical Oceanography*, *43*(8), 1533–1550, doi:10.1175/JPO-D-12-0221.1.

Chapman, C. C., A. M. Hogg, A. E. Kiss, and S. R. Rintoul (2015), The dynamics of Southern Ocean storm tracks, *Journal of Physical Oceanography*, *45*(3), 884–903, doi:10.1175/JPO-D-14-0075.1.

Chereskin, T. K., K. A. Donohue, D. R. Watts, K. L. Tracey, Y. L. Firing, and A. L. Cutting (2009), Strong bottom current and cyclogenesis in Drake Passage, *Geophysical Research Letters*, *36*, doi:10.1029/2009GL040940.

Chereskin, T. K., K. A. Donohue, and D. R. Watts (2012), cDrake: Dynamics and transport of the Antarctic Circumpolar Current in Drake Pasage, *Oceanography*, *25*(3), 134–135, doi:http://dx.doi.org/10.5670/oceanog.2012.86.

Chidichimo, M. P., K. A. Donohue, D. R. Watts, and K. L. Tracey (2014), Baroclinic transport time series of the Antarctic Circumpolar Current measured in Drake Passage, *Journal of Physical Oceanography*, *44*, 1829–1853, doi:10.1175/JPO-D-13-071.1.

Cronin, M. (1996), Eddy-mean flow interaction in the Gulf Stream at 68W. Part II: Eddy forcing on the time-mean flow, *Journal of Physical Oceanography*, *26*, 2132–2151.

Danielson, R. E., J. R. Gyamkun, and D. N. Straub (2006), A case study of downstream baroclinic development over the North Pacific Ocean. Part II: Diagnoses of eddy energy and wave activity, *Monthly Weather Review*, *134*, 1549–1567.

Eliassen, A., and E. Palm (1961), On the transfer of energy in stationary mountain waves, *Geofysiske Publikasjoner*, *22*, 1–23.

Firing, Y. L., T. K. Chereskin, D. R. Watts, K. L. Tracey, and C. Provost (2014), Computation of geostrophic streamfunction, its derivatives, and error estimates from an array of CPIES in Drake Passage, *Journal of Atmospheric and Oceanic Technology*, *31*, 656–680, doi:10.1175/JTECH-D-13-00142.1.

Foppert, A., K. A. Donohue, D. R. Watts, and K. L. Tracey (in rev), Eddy heat flux across the Antarctic Circumpolar Current estimated from sea-surface height standard deviation, *Journal of Geophysical Research: Oceans*.

Jackett, D. R., and T. J. McDougall (1997), A neutral density variable for the world's oceans, *Journal of Physical Oceanography*, *27*, 237–263, doi:10.1175/1520-0485(1997)0272.0.CO;2.

Nikurashin, M., and G. Vallis (2012), A theory of the interhemispheric meridional overturning circulation and associated stratification, *Journal of Physical Oceanography*, *42*(10), 1652–1667, doi:10.1175/JPO-D-11-0189.1.

Orlanski, I., and J. J. Katzfey (1991), The life cycle of a cyclone wave in the Southern Hemisphere. part 1: Eddy energy budget, *Journal of the Atmospheric Sciences*, *48*(17), 1972–1998, doi:10.1175/1520-0469(1991)048⟨1972:TLCOAC⟩2.0.CO;2.

Orlanski, I., and J. P. Sheldon (1993), A case of downstream baroclinic develop-

ment over western North America, *Monthly Weather Review*, *121*(11), 2929–2950, doi:10.1175/1520-0493(1993)121⟨2929:ACODBD⟩2.0.CO;2.

Orlanski, I., and J. P. Sheldon (1995), Stages in the energetics of baroclinic systems, *Tellus*, *47A*, 605–628, doi:10.1034/j.1600-0870.1995.00108.x.

Pedlosky, J. (1987), *Geophysical Fluid Dynamics*, 2cd ed., Springer-Verlag.

Phillips, H. E., and S. R. Rintoul (2000), Eddy variability and energetics from direct current measurements in the Antarctic Circumpolar Current south of Australia, *Journal of Physical Oceanography*, *30*(12), 3050–3076, doi:10.1175/1520-0485(2000)030⟨3050:EVAEFD⟩2.0.CO;2.

Plumb, R. A. (1983), A new look at the energy cycle, *Journal of the Atmospheric Sciences*, *40*(7), 1669–1688, doi:https://doi.org/10.1175/1520-0469(1983)040⟨1669:ANLATE⟩2.0.CO;2.

Plumb, R. A. (1985), On the three-dimensional propagation of stationary waves, *Journal of the Atmospheric Sciences*, *42*(3), 217–229, doi:https://doi.org/10.1175/1520-0469(1985)042⟨0217:OTTDPO⟩2.0.CO;2.

Takaya, K., and H. Nakamura (2001), A formulation of a phase-independent wave-activity flux for stationary and migratory quasigeostrophic eddies on a zonally varying basic flow, *Journal of the Atmospheric Sciences*, *58*, 608–627.

Toggweiler, J. R., and B. Samuels (1995), Effect of Drake Passage of the global thermohaline circulation, *Deep Sea Research I*, *42*(4), 477–500, doi:10.1016/0967-0637(95)00012-U.

Tracey, K. L., K. A. Donohue, D. R. Watts, and T. K. Chereskin (2013), cDrake CPIES data report November 2007 to December 2011, *GSO Technical Report Paper 4*, University of Rhode Island Physical Oceanography.

Watts, D. R., K. L. Tracey, K. A. Donohue, and T. K. Chereskin (2016), Estimates of eddy heat flux crossing the Antarctic Circumpolar Current from observations in Drake Passage, *Journal of Physical Oceanography*, *46*(7), 2103–2122, doi: 10.1175/JPO-D-16-0029.1.

Williams, R. G., C. Wilson, and C. W. Hughes (2007), Ocean and atmosphere storm tracks: The role of eddy vorticity forcing, *Journal of Physical Oceanography*, *37*(9), 2267–2289, doi:10.1175/JPO3120.1.

Youngs, M. K., A. F. Thompson, A. Lazar, and K. J. Richards (2017), ACC meanders, energy transfer, and mixed barotropic-baroclinic instability, *Journal of Physical Oceanography*, *47*(6), 1291–1305, doi:https://doi.org/10.1175/JPO-D-16-0160.1.

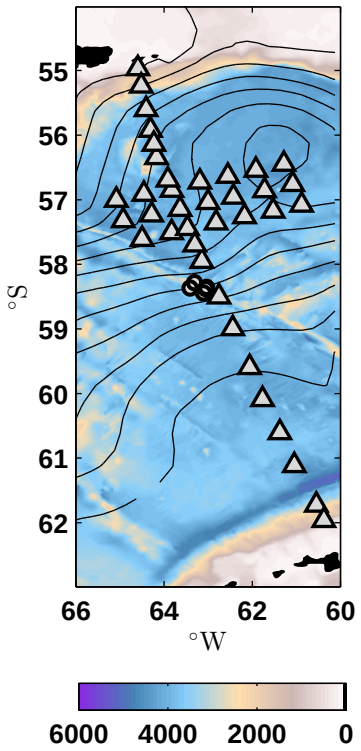

Figure 3.1. Map of Drake Passage. Bathymetry [m] is contoured with colored shading and mean SSH over the four years coincident with the cDrake experiment contoured in black (contour interval = 0.1 m). CPIES sites are shown as triangles and the 5 CPIES deployed for the last year of the experiment are shown as circles. The local dynamics array is the 3x7 array of CPIES located in the Polar Frontal Zone between the mean locations of the SAF and PF.

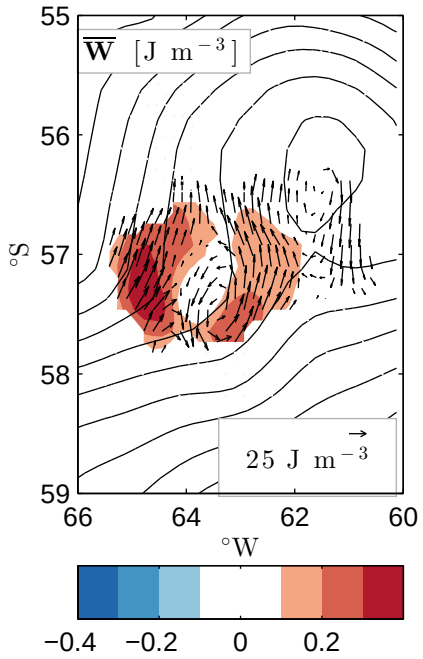

Figure 3.2. Four-year mean stationary wave activity flux vectors, $\boldsymbol{W}$ [J m^{-3}], calculated from 90-day low-passed "mean" fields in the cDrake array of CPIES using Equation 3.2 and averaged from 200 to 700 m depth. The vertical flux is color shaded and the horizontal flux is shown with arrows (plotted at every other grid point). Mean satellite SSH from the same time period is contoured in black with a contour interval of 0.1 m.

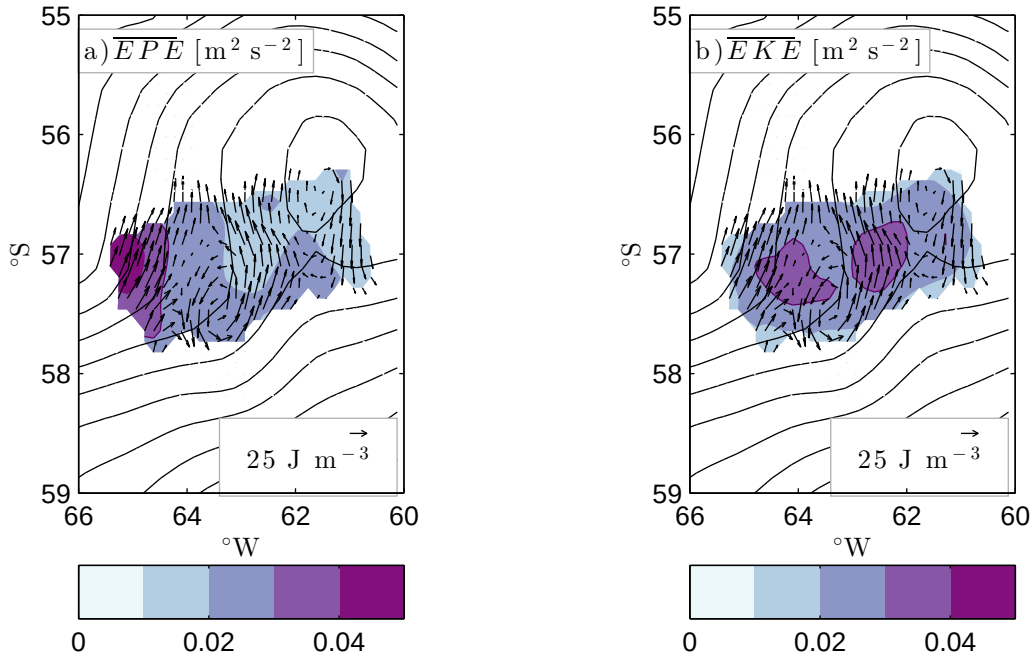

Figure 3.3. Four-year mean eddy energy [m^2 s^{-2}], (a) EPE and (b) EKE, calculated from 90-day low-passed "mean" fields in the cDrake array of CPIES and averaged from 200 to 700 m depth. The 0.03 m s^{-2} contour is drawn in purple in both panels. As in Figure 3.2, the four-year mean $\boldsymbol{W}^H$ is shown with arrows (plotted at every other grid point) and the mean satellite SSH from the same time period is contoured in black (contour interval of 0.1 m).

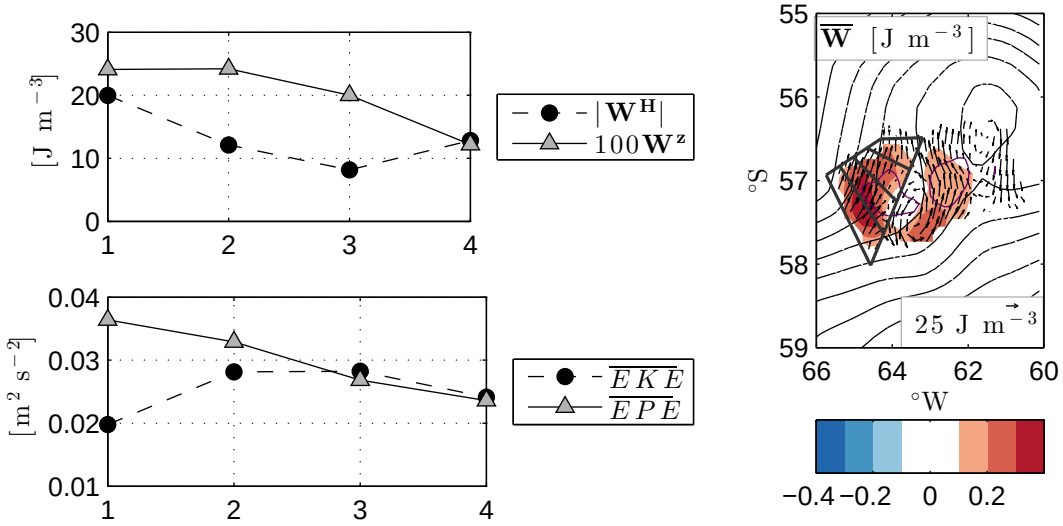

Figure 3.4. $\boldsymbol{W}$ [J m^{-3}] and eddy energy (EPE and EKE [m^2 s^{-2}]) in the western storm track. Values are averaged in the four sections depicted in the map on the right, with increasing section number (x-axis of left panels) increasing to the northeast, such that 1 is the farthest southwest section and 4 is the section farthest northeast in the LDA. The panel on the right is identical to Figure 3.2, except with added gray lines to distinguish the areas over which the values are averaged and the $\overline{EKE} = 0.03$ m^2 s^{-2} contour drawn in purple.

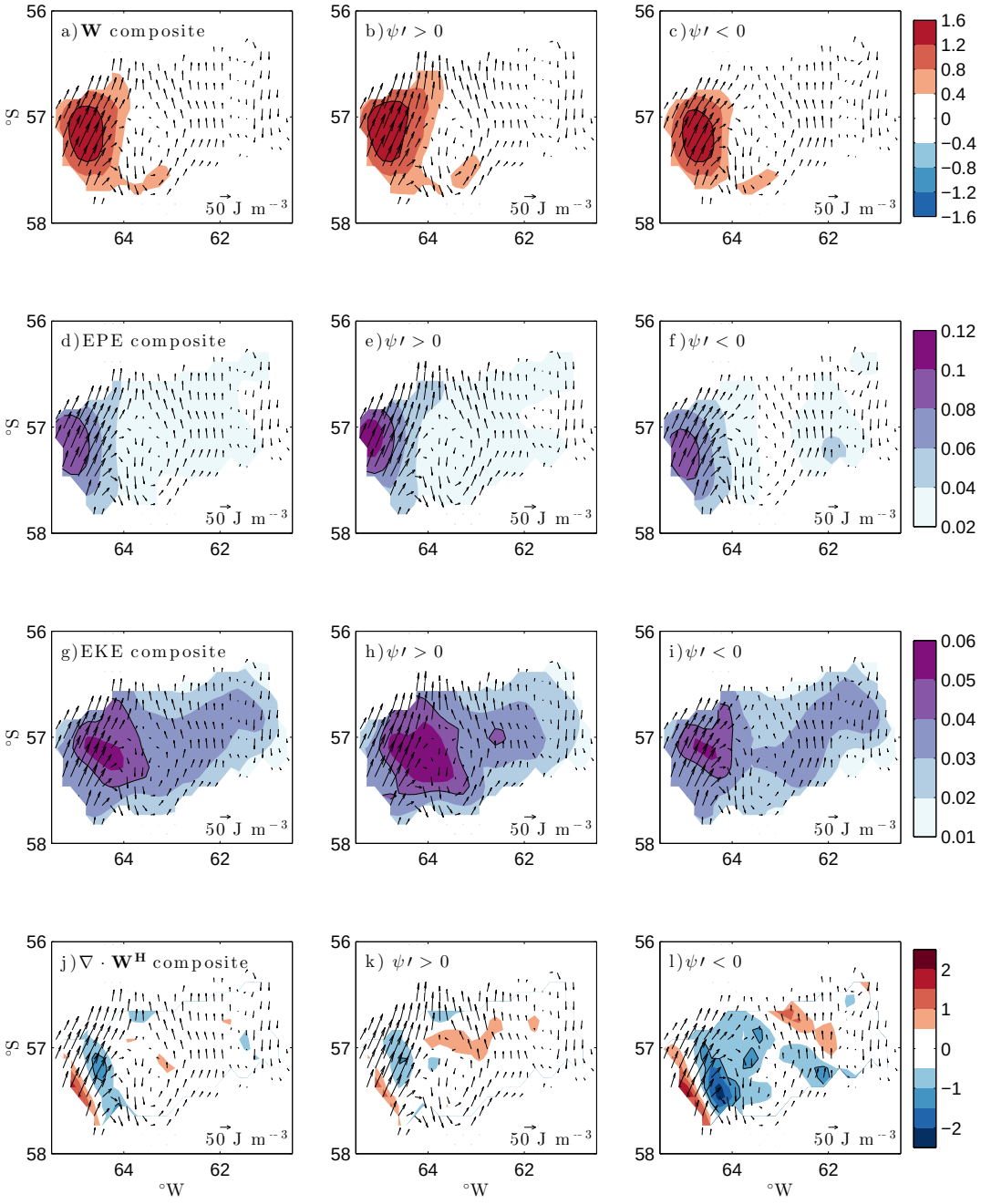

Figure 3.5. Composite-mean values of (a-c) $\boldsymbol{W}$ [J m^{-3}], (d-f) EPE [m^2 s^{-2}], (g-i) EKE [m^2 s^{-2}], and (j-l) $\nabla \cdot \boldsymbol{W}$ [J m^{-3} km^{-1}]. The composite-mean fields presented in the left column are composed from the subset of four-year time series when there was elevated vertical wave activity flux (regional-mean $\boldsymbol{W}^z > 0.5$ J m^{-3}) in the western LDA. The composite-mean fields in the center and right columns further decompose the composites on the left into times when there was a PF trough ($\psi\prime > 0$) and SAF crest ($\psi\prime < 0$) in the western LDA, respectively. The horizontal wave activity flux vectors are plotted in each panel for orientation. Black contours indicate the (a-c) $\boldsymbol{W}^z = 1.2$ J m^{-3}, (d-f) EPE$= 0.08$ m^2 s^{-2}, (g-i) EKE$= 0.04$ m^2 s^{-2}, and (j-l) $\nabla \cdot \boldsymbol{W}^H = 1$ J m^{-3} km^{-1} contours.

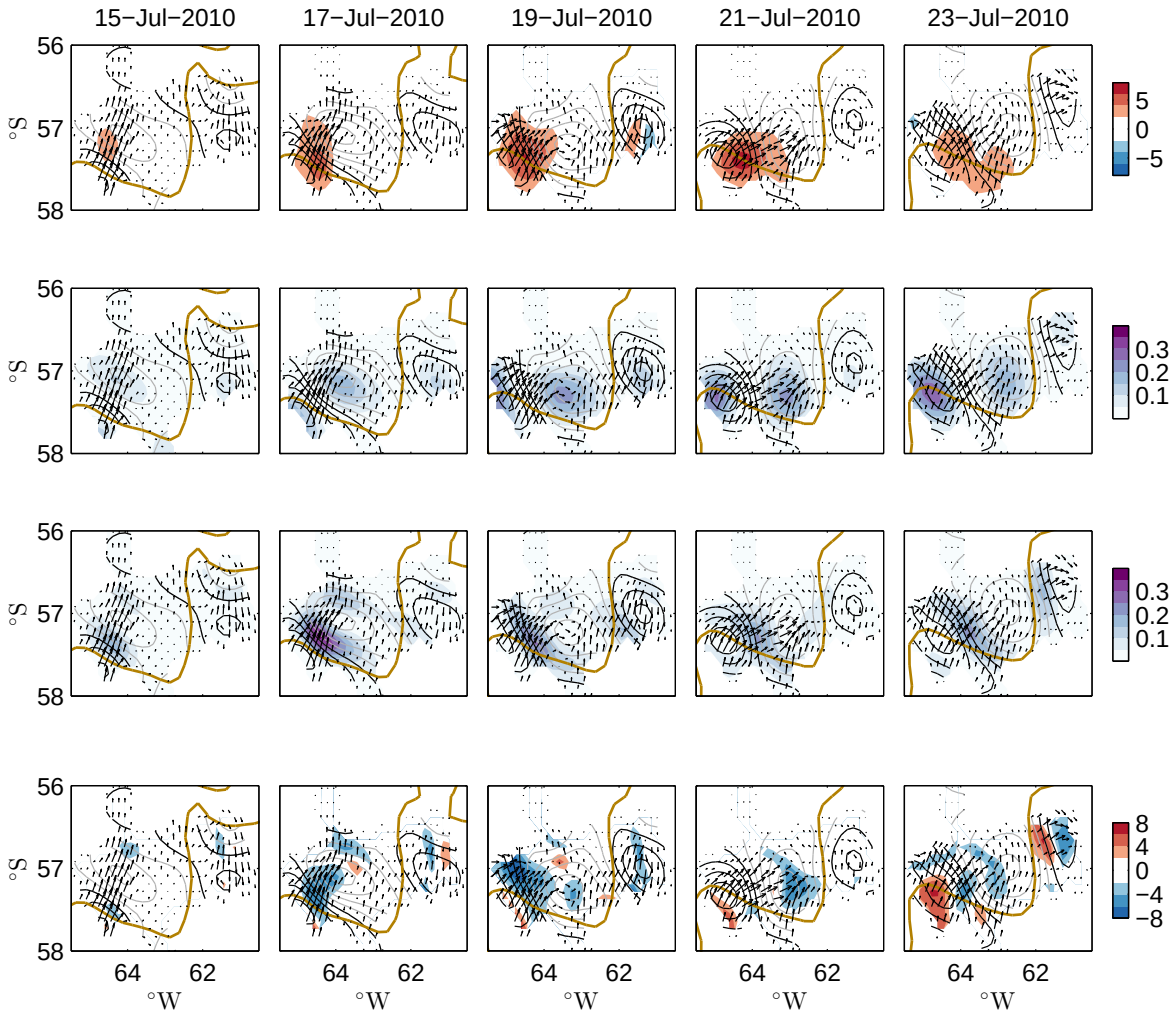

Figure 3.6. Case study of wave activity flux and its horizontal divergence (top and bottom row, respectively) and eddy energies, EPE (second row) and EKE (third row). The ψ anomaly field (deviation from 90-day low-passed mean field) is contoured, with $\psi' > 0$ in black and $\psi' < 0$ in gray. An SSH contour representative of the PF (SSH=-0.3 m) is shown in brown. The horizontal wave activity flux vectors are plotted at every other grid point in each panel for orientation.

Bibliography

Abernathey, R. P., and P. Cessi (2014), Topographic enhancement of eddy efficiency in baroclinic equilibration, *Journal of Physical Oceanography*, *44*(8), 2107–2126, doi:10.1175/JPO-D-14-0014.1.

Abernathey, R. P., J. Marshall, M. R. Mazloff, and E. Shuckburgh (2010), Enhancement of mesoscale eddy stirring at steering levels in the Southern Ocean, *Journal of Physical Oceanography*, *40*(1), 170–184, doi:10.1175/2009JPO4201.1.

Abernathey, R. P., I. Cerovecki, P. R. Holland, E. Newsom, M. R. Mazloff, and L. D. Talley (2016), Water-mass transformation by sea ice in the upper branch of the Southern Ocean overturning, *Nature Geoscience*, doi:10.1038/ngeo2749.

Adcroft, A., J. R. Scott, and J. Marotzke (2001), Impact of geothermal heating on the global ocean circulation, *Geophysical Research Letters*, *28*, 1735–1738, doi:10.1029/2000GL012182.

Ansorge, I. J., E. A. Pakhomov, S. Kaehler, J. R. E. Lutjeharms, and J. V. Durgadoo (2010), Physical and biological coupling in eddies in the lee of the South-West Indian Ridge, *Polar Biology*, *33*, 747–759, doi:10.1007/s00300-009-0752-9.

Baker, D. J., Jr., W. D. Nowlin, Jr., R. D. Pillsbury, and H. L. Bryden (1977), Antartic Circumpolar Current: Space and time fluctuations in the Drake Passage, *Nature*, *268*, 696–699, doi:10.1038/268696a0.

Baker-Yeboah, S., D. R. Watts, and D. A. Byrne (2009), Measurements of sea surface height variability in the eastern South Atlantic from pressure sensor-equipped inverted echo sounders: Baroclinic and barotropic components, *Journal of Atmospheric and Oceanic Technology*, *26*, 2593–2609, doi:10.1175/2009JTECHO659.1.

Bendat, J. S., and A. G. Piersol (2000), *Ramdom Data: Analysis and Measurement Procedures*, 3 ed., Wiley, New York.

Bischoff, T., and A. F. Thompson (2014), Configuration of a Southern Ocean storm track, *Journal of Physical Oceanography*, *44*(12), 3072–3078, doi:10.1175/JPO-D-14-0062.1.

Bishop, S. P., D. R. Watts, and K. A. Donohue (2013), Divergent eddy heat fluxes in the Kuroshio Extension at 144 - 146E. Part I: Mean structure, *Journal of Physical Oceanography*, *43*(8), 1533–1550, doi:10.1175/JPO-D-12-0221.1.

Bryden, H. L. (1979), Poleward heat flux and conversion of available potential energy in Drake Passage, *Journal of Marine Research*, *37*, 1–22.

Chang, E. K. M., and I. Orlanski (1993), On the dynamics of a storm track, *Journal of the Atmospheric Sciences*, *50*(7), 999–1015.

Chapman, C. C. (2014), Southern Ocean jets and how to find them: Improving and comparing common jet detection methods, *Journal of Geophysical Research*, *119*, 4318–4339, doi:10.1002/2014JC009810.

Chapman, C. C., A. M. Hogg, A. E. Kiss, and S. R. Rintoul (2015), The dynamics of Southern Ocean storm tracks, *Journal of Physical Oceanography*, *45*(3), 884–903, doi:10.1175/JPO-D-14-0075.1.

Chereskin, T. K., K. A. Donohue, D. R. Watts, K. L. Tracey, Y. L. Firing, and A. L. Cutting (2009), Strong bottom current and cyclogenesis in Drake Passage, *Geophysical Research Letters*, *36*(23), doi:10.1029/2009GL040940.

Chereskin, T. K., K. A. Donohue, and D. R. Watts (2012), cDrake: Dynamics and transport of the Antarctic Circumpolar Current in Drake Pasage, *Oceanography*, *25*(3), 134–135, doi:10.5670/oceanog.2012.86.

Chidichimo, M. P., K. A. Donohue, D. R. Watts, and K. L. Tracey (2014), Baroclinic transport time series of the Antarctic Circumpolar Current measured in Drake Passage, *Journal of Physical Oceanography*, *44*, 1829–1853, doi:10.1175/JPO-D-13-071.1.

Cronin, M. (1996), Eddy-mean flow interaction in the Gulf Stream at 68W. Part II: Eddy forcing on the time-mean flow, *Journal of Physical Oceanography*, *26*, 2132–2151.

Danielson, R. E., J. R. Gyamkun, and D. N. Straub (2006), A case study of downstream baroclinic development over the North Pacific Ocean. Part II: Diagnoses of eddy energy and wave activity, *Monthly Weather Review*, *134*, 1549–1567.

de Souza, J. M. A. C., A. d. M. Paiva, and K. Von Schuckmann (2013), New estimates for the heat flux across the Polar Front: spatial and temporal variability in recent years, *Antarctic Science*, *25*(3), 433–444, doi:10.1017/S0954102012001113.

de Szoeke, R. A., and M. D. Levine (1981), The advective flux of heat by mean geostrophic motions in the Southern Ocean, *Deep Sea Researh I*, *28*, 1057–1085.

Donohue, K. A., D. R. Watts, K. L. Tracey, A. D. Greene, and M. Kennelly (2010), Mapping circulation in the Kuroshio Extension with an array of current and pressure recording inverted echo sounders, *Journal of Atmospheric and Oceanic Technology*, *27*, 507–527, doi:10.1175/2009JTECHO686.1.

Donohue, K. A., M. A. Kennelly, and A. Cutting (2016), Sea surface height variability in Drake Passage, *Journal of Atmospheric and Oceanic Technology*, *33*(4), 669–683, doi:10.1175/JTECH-D-15-0249.1.

Eliassen, A., and E. Palm (1961), On the transfer of energy in stationary mountain waves, *Geofysiske Publikasjoner*, *22*, 1–23.

Ferrari, R., and M. Nikurashin (2010), Suppression of eddy diffusivity across jets in the Southern Ocean, *Journal of Physical Oceanography*, *40*(7), 1501–1519, doi:10.1175/2010JPO4278.1.

Ferrari, R., C. Provost, Y.-H. Park, N. Sennéchael, Z. Koenig, H. Sekma, G. Garric, and R. Bourdallé-Badie (2014), Heat fluxes across the Antarctic Cir-

cumpolar Current in Drake Passage: Mean flow and eddy contributions, *Journal of Geophysical Research: Oceans*, *119*, 6381–6402, doi:10.1002/2014JC010201.

Firing, Y. L., T. K. Chereskin, and M. R. Mazloff (2011), Vertical structure and transport of the Antarctic Circumpolar Current in Drake Passage from direct velocity observations, *Journal of Geophysical Research*, *116*, doi:10.1029/2011JC006999.

Firing, Y. L., T. K. Chereskin, D. R. Watts, K. L. Tracey, and C. Provost (2014), Computation of geostrophic streamfunction, its derivatives, and error estimates from an array of CPIES in Drake Passage, *Journal of Atmospheric and Oceanic Technology*, *31*, 656–680, doi:10.1175/JTECH-D-13-00142.1.

Fofonoff, N. P. (1962), Physical properties of sea water in the sea, volume 1, New York: Wiley-Interscience.

Foppert, A., K. A. Donohue, and D. R. Watts (2016), The Polar Front in Drake Passage: A composite-mean stream-coordinate view, *Journal of Geophysical Research: Oceans*, *121*, 1771–17,881, doi:10.1002/2015JC011333.

Foppert, A., K. A. Donohue, D. R. Watts, and K. L. Tracey (in rev), Eddy heat flux across the Antarctic Circumpolar Current estimated from sea-surface height standard deviation, *Journal of Geophysical Research: Oceans*.

Hogg, A. M., M. P. Meredith, D. P. Chambers, E. P. Abrahamsen, C. W. Hughes, and A. K. Morrison (2014), Recent trends in the Southern Ocean eddy field, *Journal of Geophysical Research: Oceans*, *120*, 257–267, doi:10.1002/2014/JC010470.

Holloway, G. (1986), Estimation of oceanic eddy transports from satellite altimetry, *Nature*, *323*, 243–244, doi:10.1038/323243a0.

Holton, J. R. (2004), *An Introduction to Dynamic Meteorology*, 4 ed., Academic Press.

Gille, S. T. (2003), Float observations of the Southern Ocean. Part II: Eddy fluxes, *Journal of Physical Oceanography*, *33*(6), 1182–1196, doi:10.1175/1520-0485(2003)033¡1182:FOOTSO¿2.0.CO;2.

Jackett, D. R., and T. J. McDougall (1997), A neutral density variable for the world's oceans, *Journal of Physical Oceanography*, *27*, 237–263, doi:10.1175/1520-0485(1997)0272.0.CO;2.

Jacobs, S. S. (2004), Bottom water production and its links with the thermohaline circulation, *Antarctic Science*, *16*(4), 427–437, doi:10.1017/S095410200400224X.

Karsten, R. H., and J. Marshall (2002), Constructing the residual circulation of the ACC from observations, *Journal of Physical Oceanography*, *32*(12), 3315–3327, doi:10.1175/1520-0485(2002)0322.0.CO;2.

Keffer, T., and G. Holloway (1988), Estimating Southern Ocean eddy flux of heat and salt from satellite altimetry, *Nature*, *332*, 624–626, doi:10.1038/332624a0.

Kushner, P. J., and I. M. Held (1998), A test, using atmospheric data, of a method for estimating oceanic eddy diffusivity, *Geophysical Research Letters*, *25*(22), 4213–4216, doi:10.1029/1998GL900142.

Large, W. G., and A. J. Nurser (2001), *Ocean Circulation and Climate: Observing and Modeling the Global Ocean*, Academic Press.

Lenn, Y.-D., T. K. Chereskin, and J. Sprintall (2008), Improving estimates of the Antarctic Circumpolar Current streamlines in Drake Passage, *Journal of Physical Oceanography*, *38*, doi:10.1175/2007JPO3834.1.

Levitus, S. (1987), Meridional Ekman heat fluxes for the world ocean and individual ocean basins, *Journal of Physical Oceanography*, *17*(9), 1484–1492, doi:10.1175/1520-0485(1987)017¡1484:MEHFFT¿2.0.CO;2.

Lindstrom, S. S., X. Qian, and D. R. Watts (1997), Vertical motion in the

Gulf Stream and its relation to meanders, *Journal of Geophysical Research*, *102*, 8485–8503, doi:10.1029/96JC0349.

Marshall, G. J. (2003), Trends in the Southern Annular Mode from observations and reanalyses, *Journal of Climate*, *16*, 4134–4143, doi:10.1175/1520-0442(2003)016¡4134:TITSAM¿2.0.CO;2.

Marshall, J., and G. Shutts (1981), A note on rotational and divergent eddy fluxes, *Journal of Physical Oceanography*, *11*, 1677–1680, doi:10.1175/1520-0485(1981)011¡1677:ANORAD¿2.0.CO;2.

Marshall, J., E. Shuckburgh, H. Jones, and C. Hill (2006), Estimates and implications of surface eddy diffusivity in the Southern Ocean derived from tracer transport, *Journal of Physical Oceanography*, *36*(9), 1806–1821, doi:10.1175/JPO2949.1.

Masich, J., T. K. Chereskin, and M. R. Mazloff (2015), Topographic form stress in the Southern Ocean State Estimate, *Journal of Geophysical Research: Oceans*, *120*, 7919–7933, doi:10.1002/2015JC011143.

Mazloff, M. R., P. Heimbach, and C. Wunsch (2010), An eddy-permitting Southern Ocean State Estimate, *Journal of Physical Oceanography*, *40*(5), 880–899, doi:10.1175/2009JPO4236.1.

Meijers, A. J., N. L. Bindoff, and J. L. Roberts (2007), On the total, mean, and eddy heat and freshwater transports in the Southern Hemisphere of a 1/8 x 1/8 global ocean model, *Journal of Physical Oceanography*, *37*(2), 277–295, doi:10.1175/JPO3012.1.

Meinen, C. S., and D. R. Watts (2000), Vertical structure and transport on a transect across the North Atlantic Current near 42N: Time series and mean, *Journal of Geophysical Research*, *105*(C9), 21,869–21,891, doi:10.1029/2000JC900097.

Meinen, C. S., D. S. Luther, D. R. Watts, A. D. Chave, and K. L. Tracey

(2003), Mean stream coordinates structure of the Subantarctic Front: Temperature, salinity, and absolute velocity, *Journal of Geophysical Research*, *108*(C8), doi:10.1029/2002JC001545.

Meredith, M. P. (2013), Replenishing the abyss, *Nature Geoscience*, *6*, 166–167, doi:10.1038/ngeo1743.

Meredith, M. P. (2016), Understanding the structure of changes in the Southern Ocean eddy field, *Geophysical Research Letters*, *43*, 5829–5832, doi:10.1002/2016GL069677.

Meredith, M. P., and A. M. Hogg (2006), Circumpolar response of Southern Ocean eddy activity to a change in the Southern Annular Mode, *Geophysical Research Letters*, *33*, L16,608, doi:10.1029/2006GL026499.

Meredith, M. P., P. L. Woodworth, T. K. Chereskin, D. P. Marshall, L. C. Allison, G. R. Bigg, K. A. Donohue, K. J. Heywood, C. W. Hughes, A. HIbbert, A. M. Hogg, H. L. Johnson, L. Jullion, B. A. King, H. Leach, Y.-D. Lenn, M. A. M. Maqueda, D. R. Munday, A. C. Naveira-Garabato, C. Provost, J.-B. Sallée, and J. Sprintall (2011), Sustained monitoring of the Southern Ocean at Drake Passage: Past achievements and future priorities, *Reviews of Geophysics*, *49*(4), doi:10.1029/2010RG000348.

Naveira-Garabato, A. C., R. Ferrari, and K. L. Polzin (2011), Eddy stirring in the Southern Ocean, *Journal of Geophysical Research*, *116*, doi:10.1029/2010JC006818.

Nikurashin, M., and G. Vallis (2012), A theory of the interhemispheric meridional overturning circulation and associated stratification, *Journal of Physical Oceanography*, *42*(10), 1652–1667, doi:10.1175/JPO-D-11-0189.1.

Orlanski, I., and J. J. Katzfey (1991), The life cycle of a cyclone wave in the Southern Hemisphere. part 1: Eddy energy budget,

Journal of the Atmospheric Sciences, *48*(17), 1972–1998, doi:10.1175/1520-0469(1991)048¡1972:TLCOAC¿2.0.CO;2.

Orlanski, I., and J. P. Sheldon (1993), A case of downstream baroclinic development over western North America, *Monthly Weather Review*, *121*(11), 2929–2950, doi:10.1175/1520-0493(1993)121¡2929:ACODBD¿2.0.CO;2.

Orlanski, I., and J. P. Sheldon (1995), Stages in the energetics of baroclinic systems, *Tellus*, *47A*, 605–628, doi:10.1034/j.1600-0870.1995.00108.x.

Orsi, A. H., T. W. III, and W. D. N. Jr. (1995), On the meridional extent and fronts of the Antarctic Circumpolar Current, *Deep-Sea Research I*, *42*, 641–673, doi:10.1016/0967-0637(95)00021-W.

Pedlosky, J. (1987), *Geophysical Fluid Dynamics*, 2cd ed., Springer-Verlag.

Peña-Molino, B., S. R. Rintoul, and M. R. Mazloff (2014), Barotropic and baroclinic contributions to along-stream and across-stream transport in the Antarctic Circumpolar Current, *Journal of Geophysical Research: Oceans*, *119*, 8011–8028, doi:10.1002/2014JC010020.

Phillips, H. E., and S. R. Rintoul (2000), Eddy variability and energetics from direct current measurements in the Antarctic Circumpolar Current south of Australia, *Journal of Physical Oceanography*, *30*(12), 3050–3076, doi:10.1175/1520-0485(2000)030¡3050:EVAEFD¿2.0.CO;2.

Plumb, R. A. (1983), A new look at the energy cycle, *Journal of the Atmospheric Sciences*, *40*(7), 1669–1688, doi:https://doi.org/10.1175/1520-0469(1983)040¡1669:ANLATE¿2.0.CO;2.

Plumb, R. A. (1985), On the three-dimensional propagation of stationary waves, *Journal of the Atmospheric Sciences*, *42*(3), 217–229, doi:https://doi.org/10.1175/1520-0469(1985)042¡0217:OTTDPO¿2.0.CO;2.

Rodrigues, R. R., M. Wimbush, D. R. Watts, L. M. Rothstein, and

M. Ollitrault (2010), South Atlantic mass transports obtained from subsurface float and hydrographic data, *Journal of Marine Research*, *68*(6), 819–850, doi:10.1357/002224010796673858.

Sekma, H., Y.-H. Park, and F. Vivier (2013), Time-mean flow as the prevailing contributiont to the poleward heat flux across the southern flank of the Antarctic Circumpolar Current: A case study in the Fawn Trough, Kerguelen Plateau, *Journal of Physical Oceanography*, *43*(3), 583–601, doi:10.1175/JPO-D-12-0125.1.

Smith, W. H., and D. T. Sandwell (1997), Global sea floor topography from satellite altimetry and ship depth soundings, *Science*, *277*(5334), 1956–1962, doi:10.1126/science.277.5334.1956.

Sokolov, S., and S. R. Rintoul (2007), Multiple jets of the Antarctic Circumpolar Current South of Australia, *Journal of Physical Oceanography*, *37*, doi:10.1175/JPO3111.1.

Sokolov, S., and S. R. Rintoul (2009a), Cirumpolar structure and distribution of the Antarctic Circumpolar Current fronts: 1. Mean circumpolar paths, *Journal of Geophysical Research*, *114*, doi:10.1029/2008JC005108.

Sokolov, S., and S. R. Rintoul (2009b), Cirumpolar structure and distribution of the Antarctic Circumpolar Current fronts: 2. Variability and relationship to sea surface height, *Journal of Geophysical Research*, *114*, doi:10.1029/2008JC005248.

Takaya, K., and H. Nakamura (2001), A formulation of a phase-independent wave-activity flux for stationary and migratory quasigeostrophic eddies on a zonally varying basic flow, *Journal of the Atmospheric Sciences*, *58*, 608–627.

Toggweiler, J. R., and B. Samuels (1995), Effect of Drake Passage of the global thermohaline circulation, *Deep Sea Research I*, *42*(4), 477–500, doi:10.1016/0967-0637(95)00012-U.

Thompson, A. F., and A. C. Naveira-Garabato (2014), Equilibration of

the Antarctic Circumpolar Current by standing meanders, *Journal of Physical Oceanography*, *44*, doi:10.1175/JPO-D-13-0163.1.

Thompson, A. F., and J.-B. Sallée (2012), Jets and topography: Jet transitions and the impact on transport in the Antarctic Circumpolar Current, *Journal of Physical Oceanography*, *42*, doi:10.1175/JPO-D-11-0135.1.

Tracey, K. L., K. A. Donohue, D. R. Watts, and T. K. Chereskin (2013), cDrake CPIES Data Report, *GSO Technical Report 2013-01*, University of Rhode Island, Graduate School of Oceanography, Narragansett, RI.

Treguier, A. M., J. Le Sommer, J. M. Molines, and B. de Cuevas (2010), Response of the Southern Ocean to the Southern Annular Mode: Interannual variability and multidecadal trend, *Journal of Physical Oceanography*, *40*(7), 1659–1668, doi:10.1175/2010JPO4364.1.

Volkov, D. L., L.-L. Fu, and T. Lee (2010), Mechanisms of the meridional heat transport in the Southern Ocean, *Ocean Dynamics*, *60*, 791–801, doi:10.1007/s10236-010-0288-0.

Watts, D. R., K. L. Tracey, K. A. Donohue, and T. K. Chereskin (2016), Estimates of eddy heat flux crossing the Antarctic Circumpolar Current from observations in Drake Passage, *Journal of Physical Oceanography*, *46*(7), 2103–2122, doi:10.1175/JPO-D-16-0029.1.

Williams, R. G., C. Wilson, and C. W. Hughes (2007), Ocean and atmosphere storm tracks: The role of eddy vorticity forcing, *Journal of Physical Oceanography*, *37*(9), 2267–2289, doi:10.1175/JPO3120.1.

Youngs, M. K., A. F. Thompson, A. Lazar, and K. J. Richards (2017), ACC meanders, energy transfer, and mixed barotropic-baroclinic instability, *Journal of Physical Oceanography*, *47*(6), 1291–1305, doi:https://doi.org/10.1175/JPO-D-16-0160.1.

Zhiwei, Z., Z. Yisen, T. Jiwei, Y. Qingxuan, and Z. Wei (2014), Estimation of eddy heat transport in the global ocean from Argo data, *Acta Oceanologica Sinica*, *33*(1), 42–47, doi:10.1007/s13131-014-0421-x.